Synthesis, Characterization and Testing of Bi_2MoO_6-Based Semiconductors Applied in Photocatalytic Water Treatment

Yuxuan Ren

A thesis submitted to the
Faculty of Graduate and Postdoctoral Studies
in partial fulfillment of the requirements
for the Master of Applied Science in Chemical Engineering

uOttawa

Department of Chemical and Biological Engineering
Faculty of Engineering
University of Ottawa

Abstract

Photocatalysis has received increasing attention in recent years as an effective technology in wastewater treatment applications. In this project, bismuth molybdate (Bi_2MoO_6), which is a popular visible-light-driven photocatalyst, was prepared by solvothermal and hydrothermal methods. The synthesis conditions, including thermal reaction temperature, synthesis duration, and precursor stirring time of the solvothermal method were optimized based on the photodegradation of Rhodamine B (RhB) under visible light irradiation. Furthermore, the CeO_2/Bi_2MoO_6 composites with different CeO_2 loading content were successfully prepared by the wet impregnation route and characterized by X-ray diffraction (XRD), X-ray photoelectron spectroscopy (XPS), scanning electron microscopy (SEM), high resolution transmission electron microscopy (HRTEM), energy dispersive spectroscopy (EDS) and diffuse-reflection spectroscopy (DRS). The photodecomposition of RhB aqueous solution under visible light irradiation indicated that composites showed enhancements in degradation activity and 20 wt% CeO_2/Bi_2MoO_6 exhibited the highest photocatalytic activity which was 24.13% and 83.33% higher than those of Bi_2MoO_6 and CeO_2, respectively. This enhancement could be attributed to the formation of heterojunctions that effectively suppressed the recombination of holes and electrons. Quenching experiments revealed that photo-induced holes and superoxide radicals ($O_2^{\bullet -}$) were the main active species during the degradation process. Reusability was assessed by a set of 5 cycling degradation experiments and the results indicated that the composite could be applied long-term. Moreover, the effect of some operating parameters including temperature, initial pH, catalyst dosage and initial substrate concentration were investigated.

Résumé

La photocatalyse fait l'objet d'une attention croissante ces dernières années en tant que technologie efficace dans les applications de traitement des eaux usées. Dans ce projet, molybdate de bismuth (Bi_2MoO_6), qui est un photocatalyseur populaire piloté par la lumière visible, a été préparé par des méthodes hydrothermales et solvothermales. Les conditions de synthèse, y compris la température de réaction thermique, la durée de synthèse et la durée d'agitation du précurseur du procédé solvothermal ont été optimisées sur la base de la photodégradation de la Rhodamine B (RhB) sous irradiation par lumière visible. De plus, les composites CeO_2 / Bi_2MoO_6 avec différents contenus de CeO_2 ont été préparées avec succès par voie d'imprégnation humide et caractérisées par diffraction des rayons X (XRD), spectroscopie photoélectronique par rayons X (XPS), microscopie électronique à balayage (SEM), transmission à haute révolution microscopie électronique (HRTEM), spectroscopie à dispersion d'énergie (EDS) et spectroscopie à réflexion diffuse (DRS). La photodécomposition de la solution aqueuse de RhB sous irradiation par la lumière visible indiquait que les composites présentaient une amélioration de l'activité de la dégradation et que 20% en poids de CeO_2/Bi_2MoO_6 présentait l'activité photocatalytique la plus élevée, soit 24.13% et 83.33% supérieurs à ceux de Bi_2MoO_6 et CeO_2. Cette amélioration pourrait être attribuée à la formation d'hétérojonctions qui supprimaient efficacement la recombinaison des trous et des électrons. Des expériences de trempe ont révélé que les trous photoinduits et les radicaux superoxydes ($O_2^{\bullet -}$) étaient la principale espèce active au cours du processus de dégradation. La réutilisabilité a été évaluée par une série de 5 expériences de dégradation par cycles et les résultats ont indiqué que le composite pouvait être appliqué à long terme. En outre, l'effet de certains

paramètres de fonctionnement, notamment la température, le pH initial, le dosage du catalyseur et la concentration initiale en substrat, a été étudié.

Acknowledgements

First, I would like to express my deep appreciation to my supervisor, Dr. Zisheng (Jason) Zhang who encouraged me to pursue my master's degree and provided me with knowledgeable and priceless guidance.

I would also feel grateful to Dr. Yun Liu at the Centre for Catalysis and Innovation (CCRI) in the University of Ottawa (uOttawa) for the kind help of sample characterization.

I would thank Dr. Xiangchao Meng for helpful advice and assistance in XRD analysis. I would also thank Yu and Zizhen in our group for their encouragement.

Finally, I would express my deep gratitude to my dear parents and my beloved boyfriend, who provided me with invaluable love and courage.

Nomenclature and Abbreviations

AOP	Advanced oxidation process
CB	Conduction band
CTAB	Cetyltrimethylammonium bromide
DDW	Double distilled water
DER	N, N'-Diethyl-Rhodamine
DRS	Diffuse-reflection spectroscopy
E_a	Apparent activation energy
EDS	Energy dispersive spectroscopy
EDTA	Ethylenediaminetetraacetic acid
E_g	Band bap energy
EG	Ethylene glycol
ER	N-Ethyl-Rhodamine (aka Rhodamine B)
E_t	True activation energy
FE-SEM	Field-emission scanning electron microscopy
HAc	Acetic acid
HRTEM	High-resolution transmission electron microscopy
IC	Indigo carmine
MB	Methylene blue
PAA	Porous anodic alumina
PEG	Polyethylene glycol
PVP	Polyvinylpyrrolidone

pzc	Point-of-zero charge
RhB	Rhodamine B
TER	N, N, N'-Triethyl-Rhodamine
VB	Valence band
XPS	X-ray photoelectron spectroscopy
XRD	X-ray powder diffraction

Table of Contents

List of Figures

List of Tables

Chapter 1 – Introduction

1.1 Background

With the continuous increase of global population and the spread of industrialization, resource shortage and environmental contamination are a growing problem in recent decades. Water shortage is one of the most serious and urgent problems facing humanity as access to fresh, clean water is limited in many regions around the world[1]. To effectively recycle water, the importance of wastewater treatment is therefore highlighted. Many technologies have been developed to decompose pollutants in the wastewater; however, these technologies cannot be applied in large-scale processes because they suffer from low efficiency and high costs, or they result in incomplete degradation of the pollutants[2-4]. Advanced oxidation processes (AOPs) like the Fenton process and ozone/ultraviolet light treatment processes have been regarded as promising technologies which are more effective and environmental-friendly[5, 6]. The most critical process in AOPs is the generation of hydroxyl radicals (•OH), which exhibit strong oxidative abilities and can thoroughly convert pollutants to non-toxic products[7]. The reaction generally shows high rate constants in the order of 10^6–10^9 M^{-1} s^{-1}[4].

The development of heterogeneous photocatalysis, an advanced oxidation process, shows great promise in wastewater treatment. Semiconductors are commonly used as photocatalysts. It is well-known that metals show continuous electronic states, while semiconductors include a vacant region, or band gap (E_g), between a fully filled valence band (VB) and an empty conduction band (CB)[8-10]. Their band gap is generally narrower than insulators, which is essential to allow them to be activated by light energy[11]. Thus, with sufficient energy from light irradiation, electrons will be activated and jump to the conduction band (CB). A corresponding quantity of holes with positive charges are left on the valence band (VB). These photoinduced charge carriers will further directly or indirectly participate in the oxidation processes to achieve decomposition of pollutants[11, 12].

Titanium dioxide (TiO_2) is one of the most widely researched semiconductor photocatalysts due to its low toxicity, low cost, excellent chemical stability and unique properties[12,13]. However, it is also well-known that the biggest drawback of TiO_2 applied as a photocatalyst is its relatively large band gap, generally in the range of 3.0-3.2 eV[10, 14, 15]. This indicates that only light in or near the UV region can provide enough energy for photo-activated reactions. However, UV light only accounts for 3% of total solar energy[16]. Research has been dedicated to the improvement of photocatalytic performance under visible light irradiation, including the modification of TiO_2 through doping[17-19] and heterojunctions[20-22], and investigation into new visible-light-driven semiconductor materials.

Bismuth molybdate, Bi_2MoO_6, a bismuth-based semiconductor, shows great potential in photocatalysis under visible light due to its narrower band gap and unique layered structure[23]. However, fast recombination of photoinduced charge carriers hinders its photodegradation activity. Cerium oxide, CeO_2, as one of the rare earth oxides, also exhibits some excellent photocatalytic properties[24-26]. In this work, the optimum synthesis conditions of Bi_2MoO_6 by the solvothermal method were investigated based on maximum photodegradation activity. The semiconductor composite CeO_2/Bi_2MoO_6 was successfully prepared with enhanced photocatalytic performance examined by degrading RhB in aqueous solution under visible light illumination.

1.2 Project Objectives

To enhance the photocatalytic performance of Bi_2MoO_6 under visible light irradiation, the objectives of this research are as follows:

1. To optimize the synthesis conditions, including thermal reaction temperature, synthesis time and precursor stirring time of Bi_2MoO_6 by the solvothermal method according to maximum photocatalytic performance under visible light;

2. To investigate the influence of different synthesis conditions on the crystal structure and morphology of the Bi_2MoO_6 photocatalyst;

3. To prepare Bi_2MoO_6 and CeO_2 by hydrothermal and precipitation methods respectively, and to synthesize CeO_2/Bi_2MoO_6 semiconductor heterojunction by the wet impregnation method;

4. To analyze the crystallinity, size, morphology, surface composition and optical properties, by XRD, SEM, TEM, EDS, XPS, and DRS;

5. To investigate the photocatalytic performance of the as-prepared composites and the stability under visible light irradiation by decomposing RhB aqueous solution;

6. To analyze the effect of CeO_2 loading content as well as the influence of other operating conditions like temperature, pH, catalyst dosage and initial RhB concentration;

7. To investigate the main active species and propose a possible photocatalytic mechanism of this semiconductor composite with enhanced degradation activity under visible light.

1.3 Thesis Outline

The thesis is composed of five chapters, including background information (introduction and literature review), experimental results (two chapters) and conclusion, the details of which are illustrated as follows:

- **Chapter 1 – Introduction**

This chapter generally introduces the necessity of wastewater treatment, basic information of photocatalysis and the main objectives of the thesis.

- **Chapter 2 – Literature Review**

In this chapter, a general introduction of the photocatalysis mechanism was given and various prepared routes of Bi_2MoO_6 and CeO_2 were summarized.

- **Chapter 3 – Optimization of Synthesis Conditions of Solvothermal-Prepared Bi_2MoO_6**

The influence of reaction temperature, synthesis duration and precursor stirring time during the solvothermal synthesis of Bi_2MoO_6 was investigated. The process was optimized with the goal of maximizing the photodegradation of RhB under visible light. Furthermore, the crystal structure and morphology of the photocatalyst was studied under various reaction conditions.

- **Chapter 4 – Enhanced Photocatalytic Activity of CeO_2/Bi_2MoO_6 Semiconductor Composites Applied in Water Treatment Under Visible Light Irradiation**

CeO_2/Bi_2MoO_6 semiconductor composites with different amount of CeO_2 loading were prepared. and the effect of some operating parameters was investigated. The pathway of RhB decomposition as well as the possible mechanism of enhanced photocatalytic performance were discussed.

- **Chapter 5 – Conclusions**

The main conclusions based on experimental results are summarized and future work is recommended.

1.4 References

1. Oturan, M.A. and J.-J. Aaron, Advanced oxidation processes in water/wastewater treatment: principles and applications. A review. Critical Reviews in Environmental Science and Technology, 2014. **44**(23): p. 2577-2641.
2. Han, F., et al., Tailored titanium dioxide photocatalysts for the degradation of organic dyes in wastewater treatment: a review. Applied Catalysis A: General, 2009. **359**(1-2): p. 25-40.

3. Oller, I., S. Malato, and J. Sánchez-Pérez, Combination of advanced oxidation processes and biological treatments for wastewater decontamination—a review. Science of the Total Environment, 2011. **409**(20): p. 4141-4166.
4. Andreozzi, R., et al., Advanced oxidation processes (AOP) for water purification and recovery. Catalysis Today, 1999. **53**(1): p. 51-59.
5. Stasinakis, A., Use of selected advanced oxidation processes (AOPs) for wastewater treatment–a mini review. Global NEST Journal, 2008. **10**(3): p. 376-385.
6. Gupta, V.K., et al., Chemical treatment technologies for waste-water recycling—an overview. Rsc Advances, 2012. **2**(16): p. 6380-6388.
7. Deng, Y. and R. Zhao, Advanced oxidation processes (AOPs) in wastewater treatment. Current Pollution Reports, 2015. **1**(3): p. 167-176.
8. Linsebigler, A.L., G. Lu, and J.T. Yates Jr, Photocatalysis on TiO_2 surfaces: principles, mechanisms, and selected results. Chemical Reviews, 1995. **95**(3): p. 735-758.
9. Kabra, K., R. Chaudhary, and R.L. Sawhney, Treatment of hazardous organic and inorganic compounds through aqueous-phase photocatalysis: a review. Industrial & Engineering Chemistry Research, 2004. **43**(24): p. 7683-7696.
10. Lee, S.-Y. and S.-J. Park, TiO_2 photocatalyst for water treatment applications. Journal of Industrial and Engineering Chemistry, 2013. **19**(6): p. 1761-1769.
11. Meng, X., Z. Zhang, and X. Li, Synergetic photoelectrocatalytic reactors for environmental remediation: a review. Journal of Photochemistry and Photobiology C: Photochemistry Reviews, 2015. **24**: p. 83-101.

12. Dong, S., et al., Recent developments in heterogeneous photocatalytic water treatment using visible light-responsive photocatalysts: a review. Rsc Advances, 2015. **5**(19): p. 14610-14630.

13. Wen, J., et al., Photocatalysis fundamentals and surface modification of TiO_2 nanomaterials. Chinese Journal of Catalysis, 2015. **36**(12): p. 2049-2070.

14. Houas, A., et al., Photocatalytic degradation pathway of methylene blue in water. Applied Catalysis B: Environmental, 2001. **31**(2): p. 145-157.

15. Tang, J., Z. Zou, and J. Ye, Efficient photocatalytic decomposition of organic contaminants over $CaBi_2O_4$ under visible-light irradiation. Angewandte Chemie, 2004. **116**(34): p. 4563-4566.

16. Schultz, D.M. and T.P. Yoon, Solar synthesis: prospects in visible light photocatalysis. Science, 2014. **343**(6174): p. 1239176.

17. Zhu, J., et al., Characterization of Fe–TiO_2 photocatalysts synthesized by hydrothermal method and their photocatalytic reactivity for photodegradation of XRG dye diluted in water. Journal of Molecular Catalysis A: Chemical, 2004. **216**(1): p. 35-43.

18. Cong, Y., et al., Synthesis and characterization of nitrogen-doped TiO_2 nanophotocatalyst with high visible light activity. The Journal of Physical Chemistry C, 2007. **111**(19): p. 6976-6982.

19. Ohno, T., et al., Preparation of S-doped TiO_2 photocatalysts and their photocatalytic activities under visible light. Applied Catalysis A: General, 2004. **265**(1): p. 115-121.

20. Zhang, X., et al., Low-temperature synthesis and high visible-light-induced photocatalytic activity of BiOI/TiO_2 heterostructures. The Journal of Physical Chemistry C, 2009. **113**(17): p. 7371-7378.

21. Shang, M., et al., 3D Bi_2WO_6/TiO_2 hierarchical heterostructure: controllable synthesis and enhanced visible photocatalytic degradation performances. The Journal of Physical Chemistry C, 2009. **113**(33): p. 14727-14731.

22. Sun, M., et al., Efficient degradation of azo dyes over Sb_2S_3/TiO_2 heterojunction under visible light irradiation. Industrial & Engineering Chemistry Research, 2012. **51**(7): p. 2897-2903.

23. Bi, J., et al., Simple solvothermal routes to synthesize nanocrystalline Bi_2MoO_6 photocatalysts with different morphologies. Acta Materialia, 2007. **55**(14): p. 4699-4705.

24. Liu, Y., et al., A novel $CeO_2/Bi_4Ti_3O_{12}$ composite heterojunction structure with an enhanced photocatalytic activity for bisphenol A. Journal of Alloys and Compounds, 2016. **688**: p. 487-496.

25. Miao, H., et al., Origin of enhanced photocatalytic activity of F-doped CeO_2 nanocubes. Applied Surface Science, 2016. **370**: p. 427-432.

26. Wen, X.-J., et al., AgI nanoparticles-decorated CeO_2 microsheets photocatalyst for the degradation of organic dye and tetracycline under visible-light irradiation. Journal of colloid and interface science, 2017. **497**: p. 368-377.

Chapter 2 – Literature Review

2.1 Introduction

Water is one of the most critical resources on Earth. The total amount of water available globally is huge; however, 97.2 wt% is salty ocean water that is not directly available to use, while the remainder is fresh water, either stored in glaciers, as groundwater, or as surface water[1]. This means the amount of freshwater that can be directly used by human beings is very limited. In recent years, there is an increased focus on wastewater treatment to alleviate global water shortages, promote sustainable resource use, and develop environmental protection protocols.

Initially, photocatalysis was developed as a means of water electrolysis and it is receiving tremendous interest due to its potential in wastewater treatment[2]. The mechanism of photocatalysis can be briefly defined as a series of redox reactions which are achieved by generation of some active species with high oxidative ability[3]. One of the most unique properties of photocatalysis that distinguishes it from other catalytic reactions is non-selective nature, allowing it to decompose a wide range of pollutants from various wastewater systems[4]. Photocatalysts are critical during the photodegradation process because all redox reactions happen on their surface and depend on their intrinsic electrical nature to a great extent[5]. Apart from TiO_2-based photocatalysts, which have been researched for many years, other semiconductors have also been focused as promising photocatalysts, like CeO_2 and Bi_2MoO_6.

2.2 Fundamentals of Photocatalysis in Water Treatment

During photocatalysis, a series of redox reactions is triggered by light irradiation when provided with sufficient energy. Decomposition of various chemical pollutants can be achieved by the production of oxidative species. Semiconductors whose conductivity is between those of metals and insulators have been widely studied as photocatalysts in recent years due to their special band structures[6]. Semiconductors can be classified into elemental semiconductor materials mainly located in group Ⅳ in the periodic table and compound semiconductor materials located in group Ⅲ and group Ⅴ [6].

Band gap is the vacant region between the valence band (VB) and conduction band (CB)[4]. The VB is the most energetic band fully populated by electrons and its energy represents the oxidative ability of the material; the CB is the lowest unoccupied band, and its energy represents the reductive ability of the material[5, 7, 8]. Since only energy that is equal to or greater than the band gap can trigger photoreactions, semiconductors are easier to activate than insulators because semiconductors have a lower band gap energy[9]. The band gap (E_g) can be estimated by Equation 2-1 [10]:

$$E_g(eV) = \frac{1240}{\lambda_{Abs-edge}} \qquad \text{(Eq. 2-1)}$$

where E_g and $\lambda_{Abs\text{-}edge}$ refer to the band gap (eV) and the wavelength of absorption edge (nm), respectively.

The band positions (valence band and conduction band) can be calculated by Mulliken electronegativity theory, given by Equations 2-2 and 2-3[10-12]:

$$E_{CB} = \chi_p - E^e - \frac{1}{2}E_g \quad \text{(Eq. 2-2)}$$

$$E_{VB} = E_{CB} + E_g \quad \text{(Eq. 2-3)}$$

where E_{CB}, E_{VB} and E_g are the positions of the conduction band edge, valence band edge and band gap, respectively; χ_p is the electronegativity of the semiconductor and E^e is the energy of free electrons on the hydrogen scale (≈ 4.5 eV).

First, adsorption will happen between semiconductors and substrates because all redox reactions occur on the surface of photocatalysts[5]. Electrons in the VB can be excited after absorbing sufficient energy from incident light and then jump to the CB, leaving positive holes in the VB. Since photons with different wavelength contains different amount of energy, the ideal choice of light source mostly depends on the band gap energy of the semiconductor material. The photo-generated electron-hole pairs with a life of few nanoseconds either move to the semiconductor surface and react with adsorbed substrates separately to finish decomposition or recombine with each other to produce heat[4, 13]. In an expected photoreaction, positive holes react with H_2O and OH^- on the catalyst surface to form hydroxyl radicals (•OH) that can attack pollutants via their high oxidative ability. Also, some proportion of holes also oxidize pollutants directly to generate intermediates that are converted into non-toxic products in subsequent reactions. As for electrons in the CB, they could reduce O_2 into superoxide radicals ($O_2^{\bullet -}$) which could also decompose pollutants after a series of reactions. The mechanism by which O_2 acts as an electron acceptor also effectively suppresses the charge recombination. The intact photocatalysis processes are illustrated in Equations 2-4 to 2-12 and Figure 2-1[3, 14-16]:

Step 1 – Excitation:

$$photocatalyst + hv \rightarrow h^+ + e^- \quad \text{(Eq. 2-4)}$$

$$h^{+} + OH^{-} \rightarrow OH\,\bullet \qquad \text{(Eq. 2-5)}$$

$$h^{+} + pollutant_{(ads)} \rightarrow {pollutant_{(ads)}}^{\bullet +} \qquad \text{(Eq. 2-6)}$$

Step 2 – Trapping:

$$h^{+} + H_2O \rightarrow\ OH\,\bullet + H^{+} \qquad \text{(Eq. 2-7)}$$

$$e^{-} + O_2 \rightarrow {O_2}^{\bullet -} \qquad \text{(Eq. 2-8)}$$

$${O_2}^{\bullet -} + OH\,\bullet \rightarrow HOO\,\bullet \qquad \text{(Eq. 2-9)}$$

Step 3 – Reactions of Other Radicals:

$$e^{-} + {O_2}^{\bullet -} + 2H^{+} \rightarrow H_2O_2 \qquad \text{(Eq. 2-10)}$$

$$H_2O_2 + H^{+} \rightarrow\ HOO\,\bullet + H_2O \qquad \text{(Eq. 2-11)}$$

Step 4 – Attacking:

$$OH\,\bullet / h^{+} / {O_2}^{\bullet -} /\ HOO\,\bullet + pollutants \rightarrow intermediates/final\ products \qquad \text{(Eq. 2-12)}$$

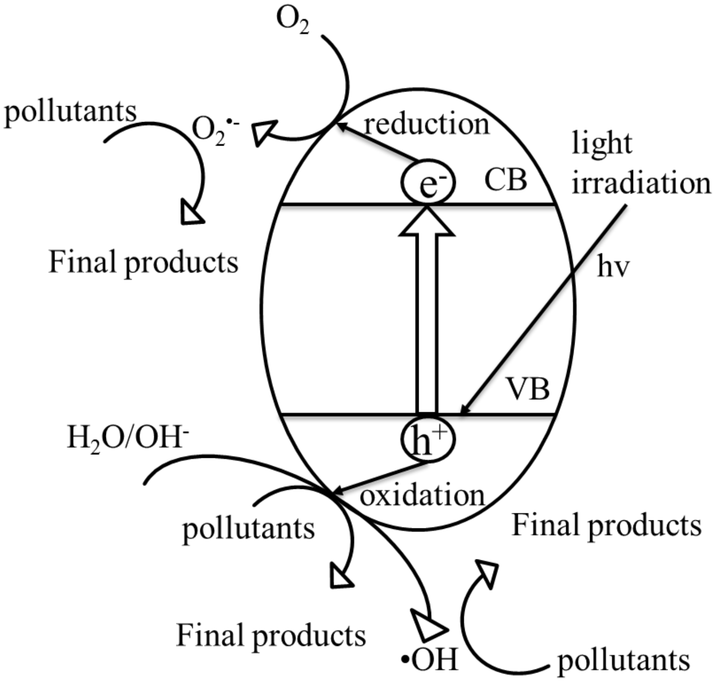

Figure 2-1. The general mechanism of photocatalysis

2.3 Effects of Operating Conditions on the Photodegradation Process

2.3.1 Temperature

Different systems show a different sensitivity to temperature. It is reported that the optimum temperatures mostly located in the region of 20-80 °C[17, 18]. Some researchers illustrate that higher temperature has a positive impact on photocatalytic reaction activity[19, 20]. However, some literatures indicate that higher temperature impedes separation of photoinduced electrons and holes and facilitates desorption process, leading to a decrease in photocatalytic activity[18, 21].

2.3.2 Initial pH

The initial pH value is a significant factor because real wastewater in industry always shows a wide range of varieties. Meanwhile, the initial pH is a complicated factor in photocatalytic treatment systems. It is impossible to state that all photocatalytic reactions in wastewater treatment are favourable in either acidic or neutral conditions because many factors like different substrates[22] and/or different catalysts[23, 24]would impact the optimum pH value. The point-of-zero charge (PZC), which is defined as the pH value when the total charge of the sorbent is zero, is an important concept to consider in this section[25]. If the PZC of a photocatalyst is lower than the solution pH, the surface of the photocatalyst would be dominated by anions and favored to absorb cations, and vice versa[24, 25]. Moreover, alkaline condition generally benefits the formation of hydroxyl radicals which may be the main active species in photocatalytic reactions[26].

2.3.3 Photocatalyst Dosage

The effect of catalyst dosage is an important consideration, as catalyst performance is directly proportional to the amount of catalyst used. However, it is also important due to the economic feasibility of the process. Catalysts costs are a significant contribution to the overall costs of the project. Many studies have revealed the influence of catalyst concentration and proposed possible reasons in photocatalysis[18, 26-32]. They indicated that with increasing catalyst dosage, photocatalytic activity increases and eventually reaches an optimum. This is due to the increased availability of electrons and holes for redox reactions, and the increased surface area of active sites on the photocatalyst material. However, after that the optimum is reached, the reaction activity begins to decrease. This evident decline can be attributed to lower light penetration into the catalyst suspension and clustering phenomena of excess catalyst. A reduction of suspension transparency would happen with continuous increase of catalyst dosage, thus more photons would be scattered and less would arrive at the catalyst surface to trigger electron excitation, thus leading to a reduced number of photoinduced charge carriers. Particle aggregation is especially noticeable for nanoparticles if the concentration surpasses a certain critical value.

2.3.4 Initial Substrate Concentration

Initial substrate concentration also has an impact on photodegradation activity. When starting at a relatively low pollutant concentration, further increasing the concentration leads to an increasing reaction rate [17, 33]. But, when starting at high initial substrate concentrations, further increasing the concentration leads to a decline in photoreaction activity because the active sites that are available for the production of oxidative species are already occupied by pollutants [18, 34, 35].

2.3.5 Additives

Apart from the above conditions, some additives may have an influence on photocatalytic performance. It has been proved that ethanol shows a quenching effect in the photodegradation process[26, 36]. In addition, some research indicates that the chloride ion, Cl^-, acts as a radical scavenger, slowing the photocatalytic reaction rate[37, 38]. On the other hand, the sulfate radical, $\bullet SO_4^{2-}$, a powerful oxidizing species generated when SO_4^{2-} ions are added as demonstrated in Equation 2-13[37], accelerates the photocatalytic reaction rate.

$$SO_4^{2-} + OH \bullet \rightarrow \bullet\, SO_4^{2-} + H_2O \qquad \text{(Eq. 2-13)}$$

2.4 Synthesis of Bi_2MoO_6

2.4.1 Solid-State Reaction[39]

Bi_2O_3 and MoO_3 with a molar ratio of 1:1 were mixed in acetone and the mixture was heated at 580 (±10) °C for 2 h. After cooling down, it was crushed in acetone and calcined for 3 more hours at the same temperature.

2.4.2 Reflux Method[40]

$Bi(NO_3)_3 \bullet 5H_2O$ and H_2MoO_4 were mixed with sufficient water and refluxed using a heater for 24 h. After washing and filtering, the sample was dried at 47 °C for 15 h and treated at 300-500 °C for 5 h. The photocatalytic activity under visible light was examined by the O_2 evolution from an $AgNO_3$ aqueous solution.

2.4.3 Co-Precipitation Method[41]

$Bi(NO_3)_3 \bullet 5H_2O$ and $(NH_4)_6Mo_7O_{24} \cdot 4H_2O$ were mixed with HNO_3 under continuous stirring. NH_4OH was introduced to adjust the pH to 3. The temperature was maintained at 70 °C and the solvent was allowed to evaporate completely. The yellow sample was collected and calcined at 450 °C, with a temperature increase 5 °C/min, for 20 h. The Bi_2MoO_6 was successfully prepared with negligible weight loss. Photocatalytic activity was tested by degrading RhB and IC (indigo carmine). Bi_2MoO_6 prepared by this method exhibited higher decomposing ratio than that prepared by solid-state method.

2.4.4 Hydrothermal Method

The hydrothermal method has become popular in recent years in material science because highly regular and uniform crystals can be achieved at a relatively lower temperature[42, 43]. $Bi(NO_3)_3{\bullet}5H_2O$ and Na_2MoO_4/ $(NH_4)_2MoO_4$ are the typical materials used in the preparation of Bi_2MoO_6 and plates/sheet-like structures are the general morphologies[41]. Notably, synthesis conditions like pH[44], temperature and time[45-47] have a significant impact on both morphologies and photocatalytic activity. L. Zhang et al.[44] prepared Bi_2MoO_6 by the hydrothermal method using HNO_3 at 180°C for 24 h and determined that with the increase of pH, the morphologies transformed from 2D sheet-like structures to 1D rod-like structures. Bi_2MoO_6 synthesized under acidic conditions showed a narrower band gap and higher photodegradation performance towards MB solution under visible light irradiation. X. Meng et al.[45] synthesized plate-like Bi_2MoO_6 by the hydrothermal method using acetic acid (HAc), demonstrating that Bi_2MoO_6 prepared at 120 °C for 24h exhibited the best photocatalytic performance under visible light irradiation when decomposing RhB.

Surfactants can be introduced in the preparation process to further control the morphology of the final structure. The related study[48] indicated that when using PVP as a surfactant during Bi_2MoO_6 synthesis, only plate-like structures were produced; without PVP, nanoparticles with irregular structures and different sizes were observed.

In addition, microwave-assisted hydrothermal method has also received increasing attention because of its high efficiency, fast heating and less time and energy consumption[43, 46, 49].

In conclusion, hydrothermal method is an efficient way to prepare Bi_2MoO_6 with uniform morphologies and high photocatalytic activities. However, careful attention must be paid to the synthesis conditions to produce these desirable products.

2.4.5 Solvothermal Method

The solvothermal method is another popular synthesis method due to easy control of sample properties like morphology and particle size, [50]. Compared with the hydrothermal method, some kinds of organic solvents instead of water precipitate the crystal growth. Ethylene glycol (EG) and ethanol are the common solvents used in Bi_2MoO_6 synthesis[51-55]. The former one plays a coordinating role to help crystal formation and the latter one can reduce the temperature needed for crystal growth due to its lower boiling point and higher vapor pressure[51, 53]. J. Bi et al.[56] investigated the influence of different solvents including water, EG and isopropanol in Bi_2MoO_6 preparation determined that Bi_2MoO_6 synthesized with EG showed smaller sizes and better photocatalytic performance on RhB decomposition. Moreover, the effect of different ratios of EG and ethanol was also studied, and the results indicated that with a EG/ethanol ratio of 1:1, the Bi_2MoO_6 showed the highest photocurrent and photoreaction rate towards RhB degradation under visible light irradiation[53]. As with the hydrothermal method, solvothermal method combined with microwave has also applied in Bi_2MoO_6 synthesis[57].

2.4.6 Ultrasonication-Assisted Method[58]

$Bi(NO_3)_3•5H_2O$ and $(NH_4)_6Mo_7O_{24}·4H_2O$ were used in this method and ultrasound was introduced to treat the aqueous mixture of these two materials for 60 minutes. After separating, washing and drying, the precipitates were calcined at 500°C for 2 h. It was found that ultrasound was in favour of generating samples with smaller sizes and higher surface areas by collision. And the photocatalytic degradation of RhB under visible light irradiation indicated that Bi_2MoO_6 prepared by ultrasound-assisted method showed a much better performance than that synthesized by solid-state route.

Overall, hydrothermal and solvothermal methods are still the most commonly-used synthesis routes for Bi_2MoO_6 preparation. Furthermore, the synthesis conditions play a critical role in the morphology, size and photocatalytic activity of the final product.

2.5 Synthesis of CeO_2

2.5.1 Precipitation Method

The precipitation method is a traditional way to prepare CeO_2 and $Ce(NO_3)_3•6H_2O$ is the typical precursor material in the synthesis. Precipitation occurs to generate $Ce(OH)_3$ firstly and the oxidation from $Ce(OH)_3$ to $Ce(OH)_4$ which can also be written as $CeO_2•2H_2O$ would continuously happen under alkaline condition[59]. Apart from adding OH^-, the precipitation and oxidation can also happen with the addition of H_2O_2. However, it has been indicated that H_2O_2 can not precipitate all Ce^{3+} from the solution. Therefore, the combination of OH^- and H_2O_2 is recommended as precipitant[59]. The CeO_2 can be obtained after calcination of the precursor to remove bound water and gain a better crystal structure[60]. To get more uniform morphologies and particle sizes, some surfactants acting as the matrix including cetyltrimethylammonium bromide (CTAB)[61], EG[10], polyvinylpyrrolidone (PVP)[62], polyethylene glycol (PEG)[63] and even egg white[64] can be applied during the synthesis.

2.5.2 Sol-Gel Method

X. Wen et al.[65] reported that CeO_2 can be prepared by this route with the addition of citric acid monohydrate ($C_6H_8O_7 \cdot H_2O$). After mixing with $Ce(NO_3)_3 \bullet 6H_2O$ in aqueous solution and evaporating under continuous stirring at 65°C, a gel is formed. Then the gel is heated at 200 °C and calcined at 450 °C to get the yellowish powder CeO_2, which shows micro-plate-like structure with a band gap of 2.81 eV. Apart from a direct reaction with acid, P. Periyat et al.[66] found that CeO_2 gel precursor could also be generated via precipitating by NH_4OH firstly and then adding urea solution and adjusting the pH to 2. After drying at 100 °C and calcining at 400-600 °C, the CeO_2 nanoparticles are obtained. The reaction mechanism can be explained by Equations 2-14 and 2-15[66]:

$$Ce(OH)_4 + (NH_2)_2CO \rightarrow (HO)_3 - Ce - O - CNHNH_2 + H_2O \qquad \text{(Eq. 2-14)}$$

$$(HO)_3 - Ce - O - CNHNH_2 \rightarrow CeO_2 + 2NH_3 + CO_2 \qquad \text{(Eq. 2-15)}$$

Moreover, templates like porous anodic alumina (PAA)[67] can be applied in this method to fabricate more ordered nano-scaled CeO_2 particles.

2.5.3 Ultrasonication-Assisted Method

Ultrasonication-assisted method has been popular due to its easy operation and high efficiency[63]. It has been reported that CeO_2 nanorods sized 5-10 nm in diameter were successfully prepared through precipitation with the addition of ultrasonication[63]. DV Pinjari et al.[68] investigated the difference of fabricated CeO_2 between ultrasonication-assisted method and general precipitation method and the results indicated that CeO_2 prepared with ultrasonication showed higher production yield and only took 20 min to produce, which was 12 times faster than those prepared by the conventional method. Furthermore, with the introduction of ultrasonication, the energy used was 92% less than that of the conventional method.

2.5.4 Hydrothermal/Solvothermal Method[69-71]

The reaction principle of hydrothermal/solvothermal method is similar to the precipitation method. In this method, $Ce(OH)_4$ acts as precursor needs to be prepared at first and then CeO_2 can be obtained after calcination.

In summary, the synthesis of CeO_2 can be achieved by many routes. The main reaction mechanism is similar, i.e., under alkaline condition, Ce^{4+} can be precipitated and then CeO_2 can be prepared successfully after removing H_2O.

2.6 Conclusions

In this review, the general mechanism of photocatalysis was introduced. The decomposition of pollutants is achieved by producing active species with high oxidative ability directly or indirectly with energy input from light irradiation. In addition, various synthesis methods of Bi_2MoO_6 and CeO_2 including both popular and rare methods were summarized. In the following sections, Bi_2MoO_6 will be prepared by hydrothermal and solvothermal methods and the CeO_2 will be synthesized by conventional precipitation method.

2.7 References

1. Oturan, M.A. and J.-J. Aaron, Advanced oxidation processes in water/wastewater treatment: principles and applications. A review. Critical Reviews in Environmental Science and Technology, 2014. **44**(23): p. 2577-2641.
2. Fujishima, A., Electrochemical photolysis of water at a semiconductor electrode. Nature, 1972. **238**: p. 37-38.
3. Dong, S., et al., Recent developments in heterogeneous photocatalytic water treatment using visible light-responsive photocatalysts: a review. Rsc Advances, 2015. **5**(19): p. 14610-14630.
4. Kabra, K., R. Chaudhary, and R.L. Sawhney, Treatment of hazardous organic and inorganic compounds through aqueous-phase photocatalysis: a review. Industrial & Engineering Chemistry Research, 2004. **43**(24): p. 7683-7696.
5. Linsebigler, A.L., G. Lu, and J.T. Yates Jr, Photocatalysis on TiO_2 surfaces: principles, mechanisms, and selected results. Chemical reviews, 1995. **95**(3): p. 735-758.
6. Neamen, D.A., Semiconductor physics and devices: basic principles. 2003: McGraw Hill.
7. König, B., Chemical Photocatalysis. 2013: Walter de Gruyter.
8. Lee, S.-Y. and S.-J. Park, TiO_2 photocatalyst for water treatment applications. Journal of Industrial and Engineering Chemistry, 2013. **19**(6): p. 1761-1769.
9. Meng, X., Z. Zhang, and X. Li, Synergetic photoelectrocatalytic reactors for environmental remediation: a review. Journal of Photochemistry and Photobiology C: Photochemistry Reviews, 2015. **24**: p. 83-101.

10. Wetchakun, N., et al., $BiVO_4/CeO_2$ nanocomposites with high visible-light-induced photocatalytic activity. ACS Applied Materials & Interfaces, 2012. **4**(7): p. 3718-3723.

11. Meng, X. and Z. Zhang, Bismuth-based photocatalytic semiconductors: introduction, challenges and possible approaches. Journal of Molecular Catalysis A: Chemical, 2016. **423**: p. 533-549.

12. Xu, Y. and M.A. Schoonen, The absolute energy positions of conduction and valence bands of selected semiconducting minerals. American Mineralogist, 2000. **85**(3-4): p. 543-556.

13. Bussi, J., et al., Photocatalytic removal of Hg from solid wastes of chlor-alkali plant. Journal of Environmental Engineering, 2002. **128**(8): p. 733-739.

14. Houas, A., et al., Photocatalytic degradation pathway of methylene blue in water. Applied Catalysis B: Environmental, 2001. **31**(2): p. 145-157.

15. Turchi, C.S. and D.F. Ollis, Photocatalytic degradation of organic water contaminants: mechanisms involving hydroxyl radical attack. Journal of Catalysis, 1990. **122**(1): p. 178-192.

16. Kwon, S., et al., Photocatalytic applications of micro-and nano-TiO_2 in environmental engineering. Critical Reviews in Environmental Science and Technology, 2008. **38**(3): p. 197-226.

17. Herrmann, J.-M., Heterogeneous photocatalysis: fundamentals and applications to the removal of various types of aqueous pollutants. Catalysis Today, 1999. **53**(1): p. 115-129.

18. Lee, K.M., et al., Recent developments of zinc oxide based photocatalyst in water treatment technology: a review. Water Research, 2016. **88**: p. 428-448.

19. Zhu, K., et al., Visible-light-induced photocatalysis and peroxymonosulfate activation over $ZnFe_2O_4$ fine nanoparticles for degradation of Orange II. Catalysis Science & Technology, 2016. **6**(7): p. 2296-2304.

20. Fu, X., et al., Effects of reaction temperature and water vapor content on the heterogeneous photocatalytic oxidation of ethylene. Journal of Photochemistry and Photobiology A: Chemistry, 1996. **97**(3): p. 181-186.

21. Gaya, U.I. and A.H. Abdullah, Heterogeneous photocatalytic degradation of organic contaminants over titanium dioxide: a review of fundamentals, progress and problems. Journal of Photochemistry and Photobiology C: Photochemistry Reviews, 2008. **9**(1): p. 1-12.

22. Piscopo, A., D. Robert, and J.V. Weber, Influence of pH and chloride anion on the photocatalytic degradation of organic compounds: Part I. Effect on the benzamide and para-hydroxybenzoic acid in TiO_2 aqueous solution. Applied Catalysis B: Environmental, 2001. **35**(2): p. 117-124.

23. Martinez-de La Cruz, A. and U.G. Perez, Photocatalytic properties of $BiVO_4$ prepared by the co-precipitation method: Degradation of rhodamine B and possible reaction mechanisms under visible irradiation. Materials Research Bulletin, 2010. **45**(2): p. 135-141.

24. Saleh, T.A. and V.K. Gupta, Functionalization of tungsten oxide into MWCNT and its application for sunlight-induced degradation of rhodamine B. Journal of Colloid and Interface Science, 2011. **362**(2): p. 337-344.

25. Fiol, N. and I. Villaescusa, Determination of sorbent point zero charge: usefulness in sorption studies. Environmental Chemistry Letters, 2009. **7**(1): p. 79-84.

26. Daneshvar, N., D. Salari, and A. Khataee, Photocatalytic degradation of azo dye acid red 14 in water on ZnO as an alternative catalyst to TiO_2. Journal of Photochemistry and Photobiology A: Chemistry, 2004. **162**(2-3): p. 317-322.

27. Chong, M.N., et al., Recent developments in photocatalytic water treatment technology: a review. Water Research, 2010. **44**(10): p. 2997-3027.

28. Bo, L., et al., Photocatalytic oxidation of trace carbamazepine in aqueous solution by visible-light-driven $Znln_2S_4$: performance and mechanism. Journal of Environmental Management, 2017. **190**: p. 259-265.

29. Huang, Z., et al., Immobilization of visible light-sensitive (N, Cu) co-doped TiO_2 onto rectorite for photocatalytic degradation of p-chlorophenol in aqueous solution. Applied Clay Science, 2017. **142**: p. 128-135.

30. Meng, X. and Z. Zhang, Synthesis, analysis, and testing of BiOBr-Bi_2WO_6 photocatalytic heterojunction semiconductors. International Journal of Photoenergy, 2015. **2015**.

31. Liang, Y., et al., Microwave-assisted synthesis of a superfine Ag/AgI photocatalyst with high activity and excellent durability. Journal of Materials Science, 2015. **50**(21): p. 6935-6946.

32. Behnajady, M., N. Modirshahla, and R. Hamzavi, Kinetic study on photocatalytic degradation of CI Acid Yellow 23 by ZnO photocatalyst. Journal of Hazardous Materials, 2006. **133**(1-3): p. 226-232.

33. Rabindranathan, S., S. Devipriya, and S. Yesodharan, Photocatalytic degradation of phosphamidon on semiconductor oxides. Journal of Hazardous Materials, 2003. **102**(2-3): p. 217-229.

34. Li, T., et al., Photocatalytic degradation of methylene blue in aqueous solution using ceramsite coated with micro-Cu_2O under visible-light irradiation. Korean Journal of Chemical Engineering, 2017. **34**(4): p. 1199-1207.

35. Akyol, A. and M. Bayramoğlu, Photocatalytic degradation of Remazol Red F3B using ZnO catalyst. Journal of Hazardous Materials, 2005. **124**(1-3): p. 241-246.

36. Galindo, C., P. Jacques, and A. Kalt, Photooxidation of the phenylazonaphthol AO20 on TiO_2: kinetic and mechanistic investigations. Chemosphere, 2001. **45**(6-7): p. 997-1005.

37. Chen, Z., et al., Enhanced photocatalytic performance over $Bi_4Ti_3O_{12}$ nanosheets with controllable size and exposed {001} facets for Rhodamine B degradation. Applied Catalysis B: Environmental, 2016. **180**: p. 698-706.

38. Arslan, I., I.A. Balcioglu, and D.W. Bahnemann, Heterogeneous photocatalytic treatment of simulated dyehouse effluents using novel TiO_2-photocatalysts. Applied Catalysis B: Environmental, 2000. **26**(3): p. 193-206.

39. Rastogi, R., A. Singh, and C. Shukla, Kinetics and mechanism of solid-state reaction between bismuth (III) oxide and molybdenum (VI) oxide. Journal of Solid State Chemistry, 1982. **42**(2): p. 136-148.

40. Shimodaira, Y., et al., Photophysical properties and photocatalytic activities of bismuth molybdates under visible light irradiation. The Journal of Physical Chemistry B, 2006. **110**(36): p. 17790-17797.

41. Martinez-de La Cruz, A. and S.O. Alfaro, Synthesis and characterization of γ-Bi_2MoO_6 prepared by co-precipitation: photoassisted degradation of organic dyes under vis-irradiation. Journal of Molecular Catalysis A: Chemical, 2010. **320**(1-2): p. 85-91.

42. Ohshima, E., et al., Growth of the 2-in-size bulk ZnO single crystals by the hydrothermal method. Journal of Crystal Growth, 2004. **260**(1-2): p. 166-170.

43. Komarneni, S., R. Roy, and Q. Li, Microwave-hydrothermal synthesis of ceramic powders. Materials Research Bulletin, 1992. **27**(12): p. 1393-1405.

44. Zhang, L., et al., Controllable synthesis of Bi_2MoO_6 and effect of morphology and variation in local structure on photocatalytic activities. Applied Catalysis B: Environmental, 2010. **98**(3-4): p. 138-146.

45. Meng, X. and Z. Zhang, Acetic Acid Assisted to Prepare Bi_2MoO_6 with Visible-Light-Induced Activity. General Chemistry, 2017. **3**(3).

46. Xie, H., et al., Microwave hydrothermal synthesis and visible-light photocatalytic activity of γ-Bi_2MoO_6 nanoplates. Materials Chemistry and Physics, 2008. **110**(2-3): p. 332-336.

47. Li, H., et al., Preparation, characterization and photocatalytic properties of nanoplate Bi_2MoO_6 catalysts. Journal of Materials Science, 2008. **43**(22): p. 7026-7034.

48. Xu, C., et al., γ-Bi_2MoO_6 nanoplates: Surfactant-assisted hydrothermal synthesis and optical properties. Ceramics International, 2009. **35**(5): p. 2099-2102.

49. Komarneni, S., R.K. Rajha, and H. Katsuki, Microwave-hydrothermal processing of titanium dioxide1. Materials Chemistry and Physics, 1999. **61**(1): p. 50-54.

50. Kang, M., et al., Characterization of a TiO_2 photocatalyst synthesized by the solvothermal method and its catalytic performance for $CHCl_3$ decomposition. Journal of Photochemistry and Photobiology A: Chemistry, 2001. **144**(2-3): p. 185-191.

51. Tian, G., et al., Facile solvothermal synthesis of hierarchical flower-like Bi_2MoO_6 hollow spheres as high performance visible-light driven photocatalysts. Journal of Materials Chemistry, 2011. **21**(3): p. 887-892.

52. Zhang, M., et al., Hierarchical heterostructures of Bi_2MoO_6 on carbon nanofibers: controllable solvothermal fabrication and enhanced visible photocatalytic properties. Journal of Materials Chemistry, 2012. **22**(2): p. 577-584.

53. Wang, X., et al., A facile mixed-solvothermal route to γ-Bi_2MoO_6 nanoflakes and their visible-light-responsive photocatalytic activity. Materials Research Bulletin, 2013. **48**(10): p. 3761-3765.

54. Tian, Y., et al., Solvothermal synthesis and enhanced visible light photocatalytic activity of novel graphitic carbon nitride–Bi_2MoO_6 heterojunctions. Powder Technology, 2014. **267**: p. 126-133.

55. Tian, G., et al., In situ growth of Bi_2MoO_6 on reduced graphene oxide nanosheets for improved visible-light photocatalytic activity. CrystEngComm, 2014. **16**(5): p. 842-849.

56. Bi, J., et al., Effects of the solvent on the structure, morphology and photocatalytic properties of Bi_2MoO_6 in the solvothermal process. Materials Research Bulletin, 2013. **48**(6): p. 2071-2075.

57. Bi, J., et al., Simple solvothermal routes to synthesize nanocrystalline Bi_2MoO_6 photocatalysts with different morphologies. Acta Materialia, 2007. **55**(14): p. 4699-4705.

58. Zhou, L., W. Wang, and L. Zhang, Ultrasonic-assisted synthesis of visible-light-induced Bi_2MO_6 (M= W, Mo) photocatalysts. Journal of Molecular Catalysis A: Chemical, 2007. **268**(1-2): p. 195-200.

59. Djuričić, B. and S. Pickering, Nanostructured cerium oxide: preparation and properties of weakly-agglomerated powders. Journal of the European Ceramic Society, 1999. **19**(11): p. 1925-1934.

60. Suresh, R., V. Ponnuswamy, and R. Mariappan, Effect of annealing temperature on the microstructural, optical and electrical properties of CeO_2 nanoparticles by chemical precipitation method. Applied Surface Science, 2013. **273**: p. 457-464.

61. Wang, G., et al., Synthesis, characterization and photoluminescence of CeO_2 nanoparticles by a facile method at room temperature. Journal of Alloys and Compounds, 2010. **493**(1-2): p. 202-207.

62. Phoka, S., et al., Synthesis, structural and optical properties of CeO_2 nanoparticles synthesized by a simple polyvinyl pyrrolidone (PVP) solution route. Materials Chemistry and Physics, 2009. **115**(1): p. 423-428.

63. Zhang, D., et al., Synthesis of CeO_2 nanorods via ultrasonication assisted by polyethylene glycol. Inorganic chemistry, 2007. **46**(7): p. 2446-2451.

64. Maensiri, S., et al., Egg white synthesis and photoluminescence of platelike clusters of CeO_2 nanoparticles. Crystal Growth & Design, 2007. **7**(5): p. 950-955.

65. Wen, X.-J., et al., Highly enhanced visible light photocatalytic activity of CeO_2 through fabricating a novel p–n junction $BiOBr/CeO_2$. Catalysis Communications, 2017. **90**: p. 51-55.

66. Periyat, P., et al., A facile aqueous sol–gel method for high surface area nanocrystalline CeO_2. RSC Advances, 2011. **1**(9): p. 1794-1798.

67. Wu, G., et al., An improved sol–gel template synthetic route to large-scale CeO_2 nanowires. Materials Research Bulletin, 2004. **39**(7-8): p. 1023-1028.

68. Pinjari, D.V. and A.B. Pandit, Room temperature synthesis of crystalline CeO_2 nanopowder: advantage of sonochemical method over conventional method. Ultrasonics Sonochemistry, 2011. **18**(5): p. 1118-1123.

69. Wang, L., et al., Characterization and optical properties of pole-like nano-CeO_2 synthesized by a facile hydrothermal method. Applied Surface Science, 2013. **286**: p. 269-274.

70. Chen, F., et al., Synergistic effect of CeO_2 modified TiO_2 photocatalyst on the enhancement of visible light photocatalytic performance. Journal of Alloys and Compounds, 2017. **714**: p. 560-566.

71. Sun, C., et al., Controlled synthesis of CeO_2 nanorods by a solvothermal method. Nanotechnology, 2005. **16**(9): p. 1454.

Chapter 3 – Optimization of Synthesis Conditions of Solvothermal-Prepared Bi_2MoO_6

Abstract

In recent years, photocatalysis has received considerable attention for its wide range of advantages, such as moderate operating conditions, low cost and thorough decomposition of pollutants without the generation of by-products. Among various semiconductor photocatalysts, Bi_2MoO_6 shows great potential in water treatment due to its narrow band gap, unique layered structure, and multiple synthesis techniques. Herein, Bi_2MoO_6 was prepared by the solvothermal method with the addition of ethylene glycol and ethanol. The optimization of synthesis conditions, including reaction temperature, time and precursor stirring time were studied. The crystal structures and morphologies under different synthesis conditions were examined by XRD and SEM, respectively. The results showed that Bi_2MoO_6 prepared under 180°C for 20 h and with a stirring time of 10 min exhibited the highest photocatalytic performance on degrading Rhodamine B (RhB) under visible light irradiation.

Key words: Photodegradation, Bi_2MoO_6, solvothermal method, RhB, visible light, water treatment

3.1 Introduction

Research into photocatalysis has progressed rapidly since the development of water splitting technology in the 1960s and 1970s by Japanese researchers[1]. In recent years, photocatalysis has been applied in many fields apart from water splitting, such as water treatment[2-5], air purification[6-8], CO_2 reduction[9-12] and disinfection[13,14]. Among these applications, decomposition of pollutants in wastewater has drawn great attention due to global water shortage and potential threats of toxic effluent discharge to the ecosystem. With light irradiation, the photoinduced electrons and holes can directly or indirectly attend the degradation process on the surface of photocatalysts by oxidizing pollutants to nontoxic products[15]. However, low visible-light absorption and fast charge carrier recombination restrict its wide application in industry[16]. As a result, more research has focused on modifying semiconductor photocatalysts to achieve better photocatalytic activity.

Bi_2MoO_6 is one of the most popular semiconductor photocatalysts in recent years due to its relatively narrow band gap (2.5-2.8 eV[17, 18]). More specifically, electrons on its valence band (VB) can be excited by visible light. As one of the Aurivillius members, it has unique perovskite-layered structures $(MoO_4)^{2-}$ between $(Bi_2O_2)^{2+}$ layers[17, 19, 20]. Moreover, its VB comprises both O *2p* orbitals and Bi *6s* orbitals, which can improve the transfer of photoinduced electrons and holes, thereby increasing the separation efficiency of charge carriers [16, 21]. Apart from its desirable band gap, Bi_2MoO_6 also shows other advantages including dielectric character, ion-conductive and luminescent properties[22]. The solvothermal method has been extensively used in photocatalyst synthesis due to its simple operation and high production yield[23].

In this project, the solvothermal method, with the addition of ethylene glycol and ethanol, was chosen to synthesize Bi_2MoO_6 and the preparation conditions were optimized. The photocatalytic performance was tested by degradation of Rhodamine B (RhB) under visible light irradiation. Using this as standard, the optimum reaction temperature, duration and precursor stirring time were obtained.

3.2 Experimental

3.2.1 Solvothermal Synthesis of Bi_2MoO_6

All chemical materials were supplied by Fisher Scientific and Sigma Aldrich. Bi_2MoO_6 was prepared by the solvothermal method using $Bi(NO_3)_3 \cdot 5H_2O$ and $Na_2MoO_4 \cdot 2H_2O$. 1.6866 g $Bi(NO_3)_3 \cdot 5H_2O$ and 0.4210 g $Na_2MoO_4 \cdot 2H_2O$ were each dissolved in 5 mL ethylene glycol and stirred for 50 min. After stirring, the $Bi(NO_3)_3 \cdot 5H_2O$ solution was slowly added to the $Na_2MoO_4 \cdot 2H_2O$ ethylene glycol solution. A white precipitate was immediately observed. Then 20 mL of ethanol was added dropwise to the mixture. After stirring for some time, the precursor mixture was transferred into a 45 mL Teflon-lined stainless-steel autoclave and reacted at a certain temperature for a designated time. After the autoclave cooled down to room temperature, the precipitates were filtered and washed several times, first by distilled deionized water (DDW), and then ethanol. The sample was then dried at 60°C and stored for characterization. The following synthesis conditions were tested to determine the optimum conditions:

Reaction temperature:	120, 140, 160, and 180°C
Synthesis time:	2, 5, 10, 15, 20, and 25 hours

Stirring time of precursor: 10, 30, and 60 minutes

3.2.2 Hydrothermal Synthesis of Bi_2MoO_6

Bi_2MoO_6 was prepared by the hydrothermal method using $Bi(NO_3)_3 \cdot 5H_2O$ and $Na_2MoO_4 \cdot 2H_2O$. 0.485 g $Bi(NO_3)_3 \cdot 5H_2O$ was dissolved in 5 mL of acetic acid and labelled as solution A; 0.121 g $Na_2MoO_4 \cdot 2H_2O$ was dissolved in 20 mL DDW and labelled as solution B. After stirring each solution for 20 mins, solution B was dropwise added to solution A. The mixture was observed to turn to a white suspension. It was magnetically stirred for an additional 20 mins at room temperature. Next, the mixture was transferred into a 45 mL Teflon-lined stainless-steel autoclave and heated to 120°C for 24 h. After the autoclave cooled down to room temperature, the yellowish precipitates were filtered and washed several times, first by DDW, and then by ethanol. The sample was then dried at 60°C and stored for characterization.

3.2.3 Characterization

The crystallinity of samples was analyzed by X-ray powder diffraction (Bruker-AXS, Karlsruhe, Germany) with Cu-Kα radiation (λ=0.15418 nm) from 5° to 80° (2θ). The structure and surface morphology of samples were obtained by scanning electron microscopy (FE-SEM, JEOL JSM-7500F).

3.2.4 Photocatalytic Performance Measurement

A slurry batch photoreactor was used to test the photocatalytic activity of as-prepared Bi_2MoO_6 under the various conditions discussed in Section 3.2.1. The photoreactor consisted of a 250 mL beaker with a thermostatic water bath, a 300 W halogen tungsten bulb (Ushio) and a UV cut-off filter. The temperature of the reactor was set at 20 °C. The 300 W halogen tungsten bulb and UV cut-off filter placed under it were designed as the light source. The filter was used to eliminate the light irradiation in the UV region (wavelength shorter than 410nm). All these apparatuses were set in a constructive shelter to minimize the influence of outside light. In each experiment, 100 mL RhB aqueous solution with a concentration of 8 ppm and 1 g/L of catalyst were added in the beaker under a constant magnetic stirring speed. Before light irradiation, a 30-min dark reaction was used to allow the catalyst to reach the absorption-desorption equilibrium. Then, the light was turned on and the photodegradation process started. Every 15 minutes, a 1 mL suspension was transferred to a 1.5 mL tube by a pipette and centrifugated under 10000 rpm for 5 minutes to separate the clear supernatant and catalysts. Then the absorbance of the supernatant was measured by a UV–vis spectrophotometer (Genesys 10 UV, Thermo Scientific). The characteristic absorption peak of RhB was set at 554 nm. The RhB remaining ratio could be calculated by Equation 3-1:

$$RhB\ remaining\ ratio\ (\%) = \left(\frac{C}{C_0}\right) \times 100\% = \left(\frac{A}{A_0}\right) \times 100\% \qquad \text{(Eq. 3-1)}$$

where c_0 and c are the initial and current concentrations of RhB solution, respectively, and A_0 and A are the initial and current absorbance of RhB solution, respectively.

3.3 Results and Discussion

3.3.1 XRD Analysis

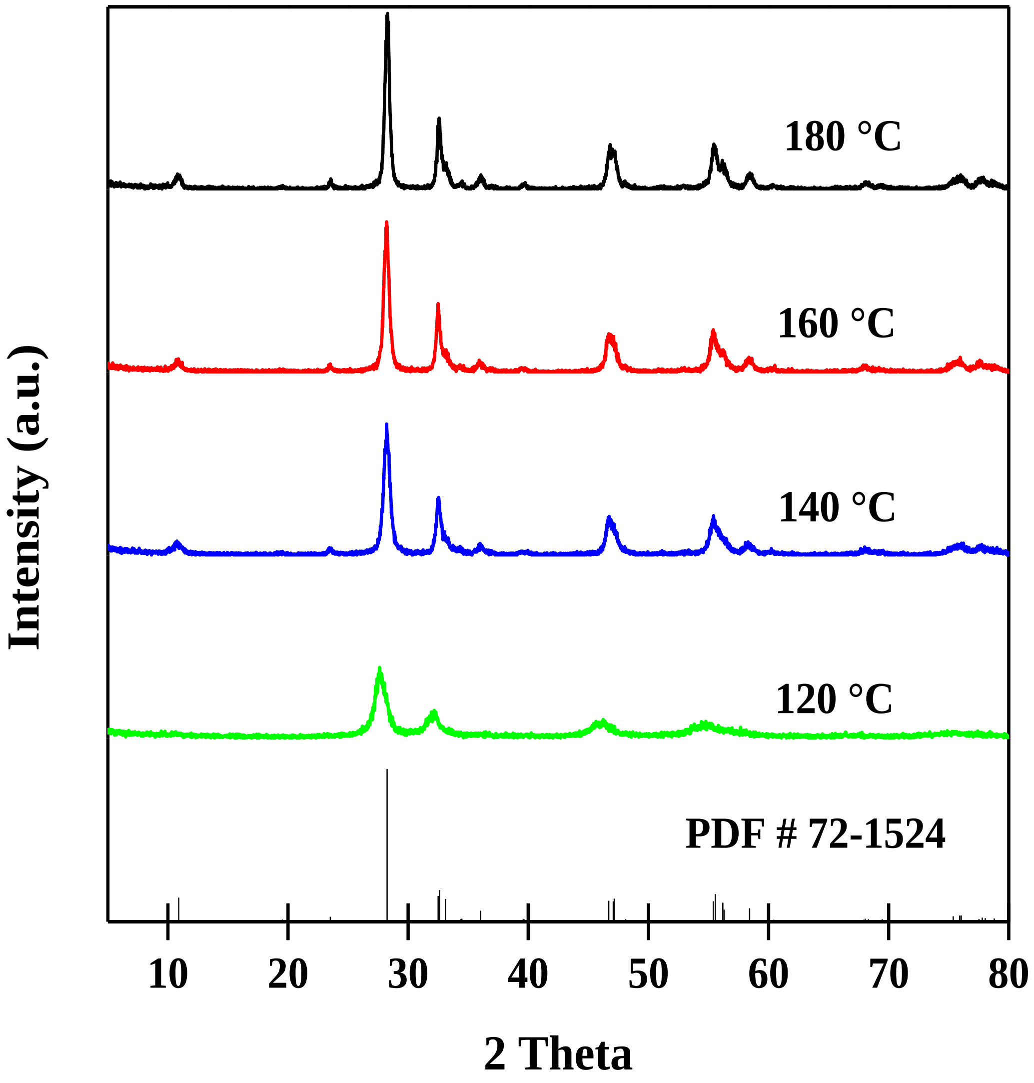

Figure 3-1. XRD pattern of Bi_2MoO_6 under different synthesis temperatures (reaction time: 20 h; precursor stirring time: 10 min)

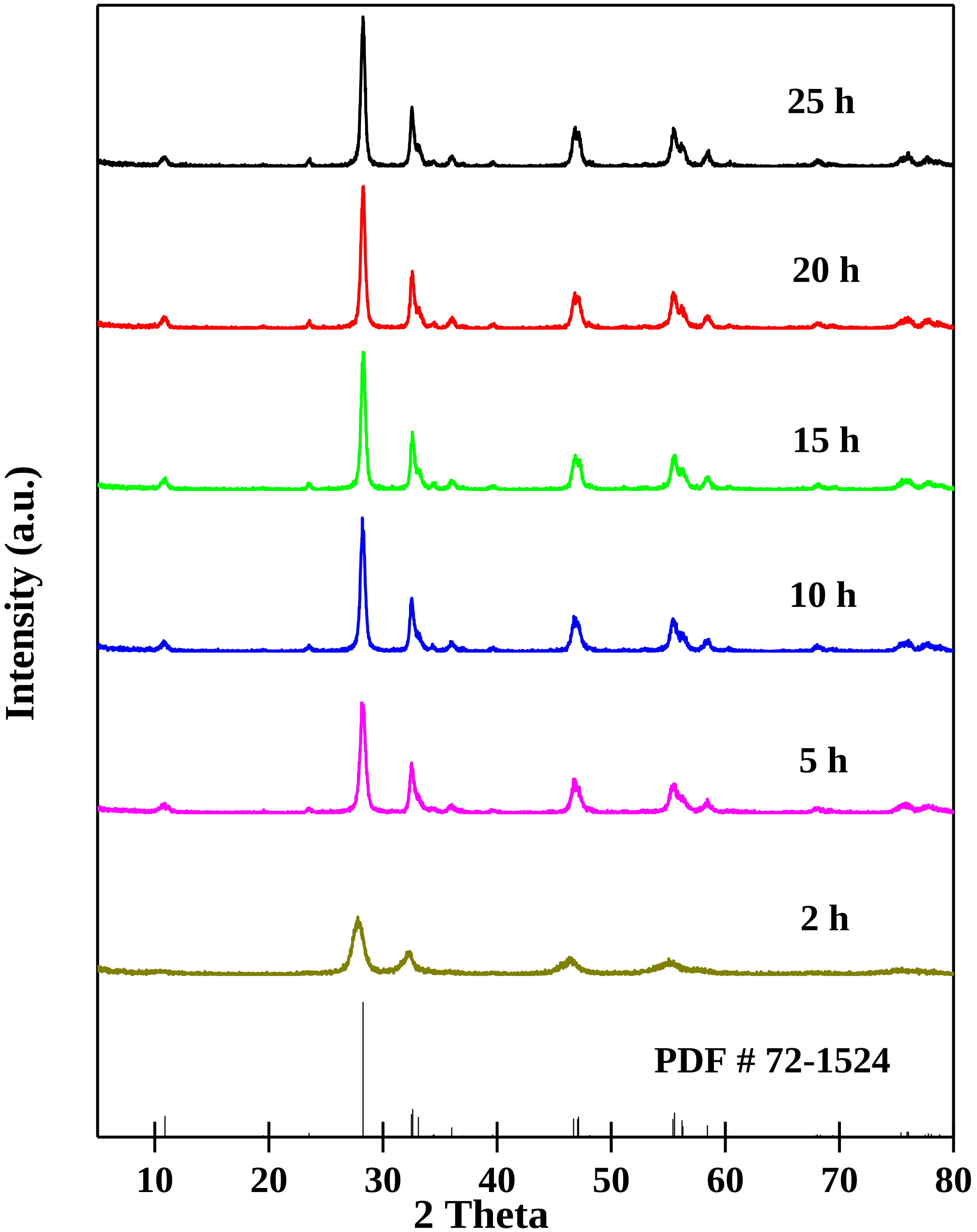

Figure 3-2. XRD pattern of Bi_2MoO_6 under different synthesis times (reaction temperature: 180°C; precursor stirring time: 10 min)

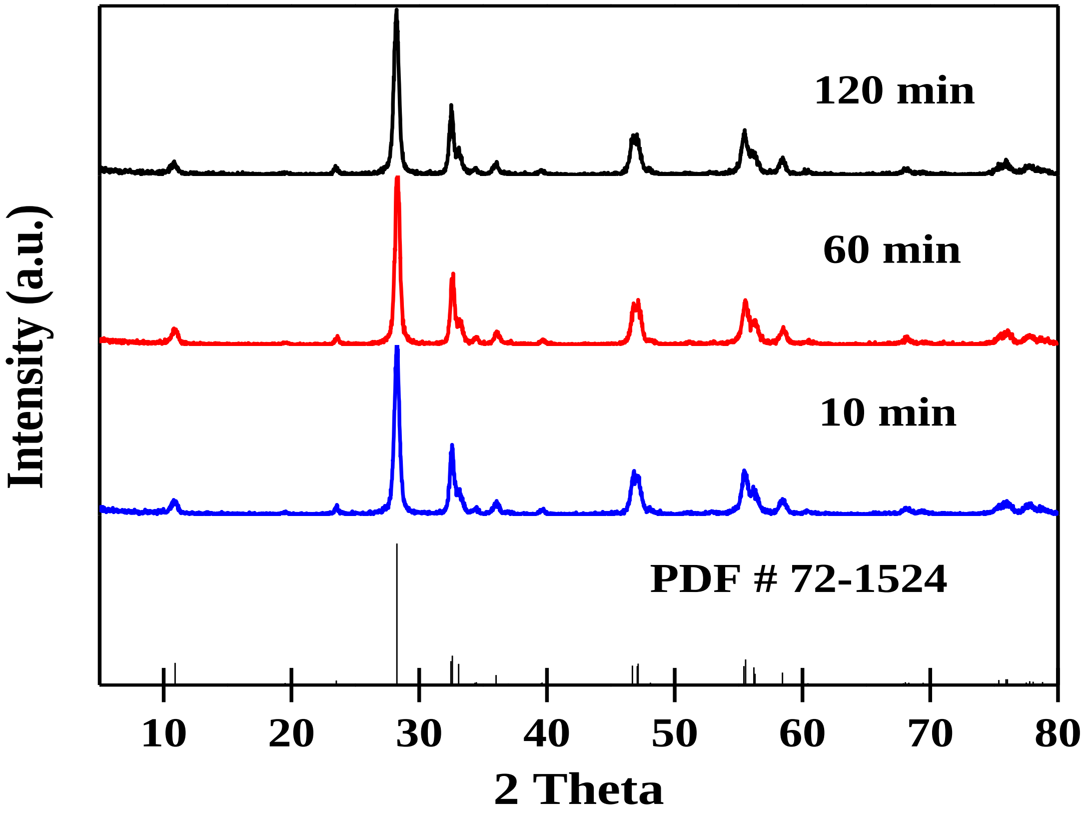

Figure 3-3. XRD pattern of Bi_2MoO_6 under different precursor stirring times (reaction temperature: 180°C; reaction time 20 h)

The XRD characterization was performed to investigate the crystal structures of Bi_2MoO_6 prepared under different conditions. When synthesized at different temperatures (Figure 3-1), it can be observed that Bi_2MoO_6 prepared at 140°C and above were well in accordance with the orthorhombic structure of the XRD standard for γ- Bi_2MoO_6 (JCPDS PDF# 72-1524). With an increase in temperature, the characteristic peaks became sharper and narrower, indicating better crystallinities of the prepared samples. At 120°C, the peak at $2\theta=10.896°$ did not appear and the other peaks were relatively low and wide. In terms of synthesis time (Figure 3-2), it can be observed that durations longer than 5 h were necessary because all characteristic peaks can be observed. When preparation times were longer than 10 h, better crystallinities were favoured. In terms of precursor stirring time (Figure 3-3), all samples showed good crystal structures and matched well with the XRD standard. There was no observable benefit to the crystal structure of the sample when the precursor stirring time was increased. No impurity peaks were observed in any of the XRD patterns in Figures 3-1 to 3-3, indicating that pure Bi_2MoO_6 with a single crystal structure was prepared successfully in all samples.

3.3.2 SEM

The morphologies of as-prepared Bi_2MoO_6 under different synthesis conditions were observed by SEM as shown in Figure 3-4. Firstly, the Bi_2MoO_6 prepared by the solvothermal method show a three-dimensional sphere-like structure sized at approximately 1 μm (Figure 3-4A to Figure 3-6A). At higher magnification, it can be seen that these spheres are composed of nanosized plates forming a flower-like structure (Figure 3-4B to Figure 3-6B). To assess the effects of reaction temperature on particle morphology, a constant precursor stirring time of 10 min and a constant reaction time of 20 h were used. For reaction temperatures ranging from 120°C to 180°C, an increase in reaction temperature causes a gradual increase in the thickness of the plate-like nanoparticles that comprised the spherical structures (Figure 3.4B1 to B4).When a reaction temperature of 120°C was used, the sphere had a sponge-like morphology and no obvious plate-like structures could be observed at 100 nm magnification (Figure 3.4B1). At 140°C, the plate-like structures were more evident (Figure 3-4B2). At 180°C, the plates were thicker than those at 160°C.

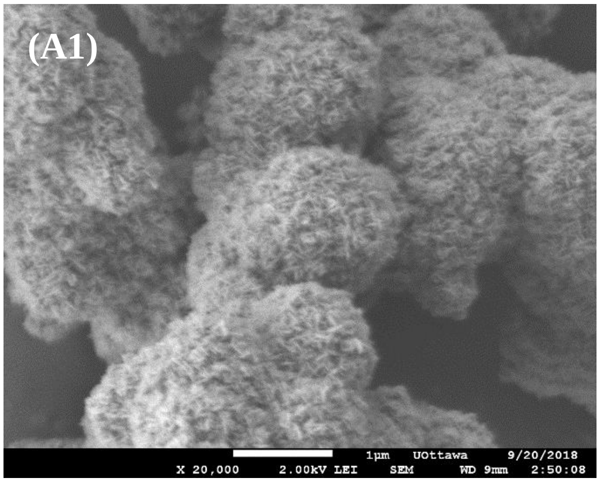
(A1)
1µm UOttawa 9/20/2018
X 20,000 2.00kV LEI SEM WD 9mm 2:50:08

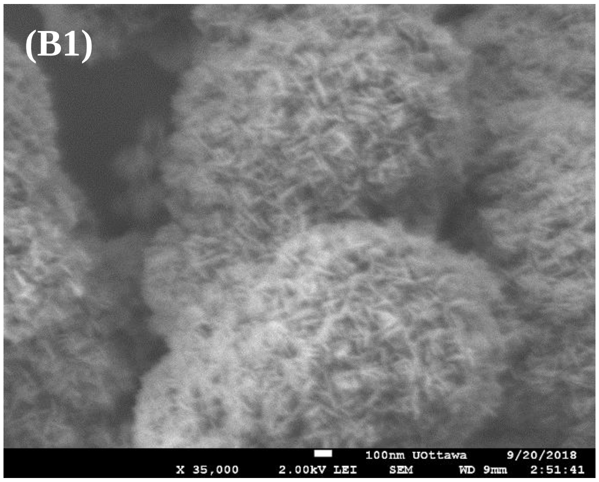
(B1)
100nm UOttawa 9/20/2018
X 35,000 2.00kV LEI SEM WD 9mm 2:51:41

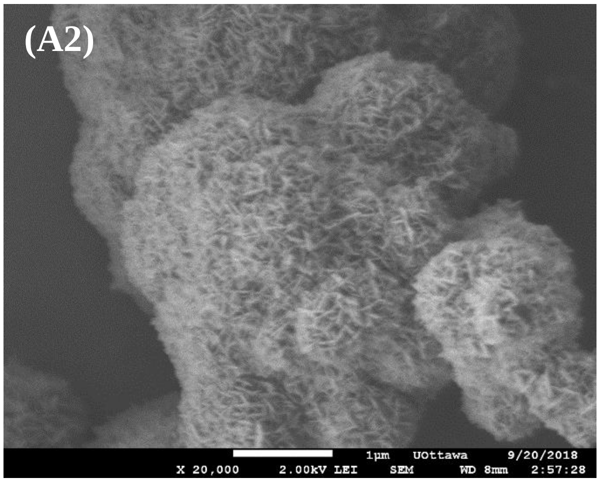
(A2)
1µm UOttawa 9/20/2018
X 20,000 2.00kV LEI SEM WD 8mm 2:57:28

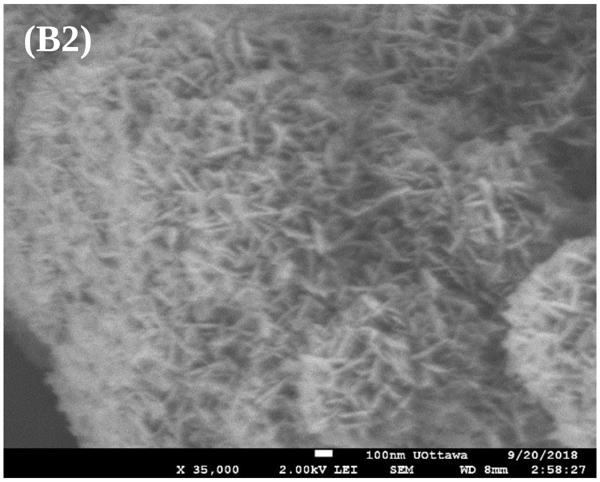
(B2)
100nm UOttawa 9/20/2018
X 35,000 2.00kV LEI SEM WD 8mm 2:58:27

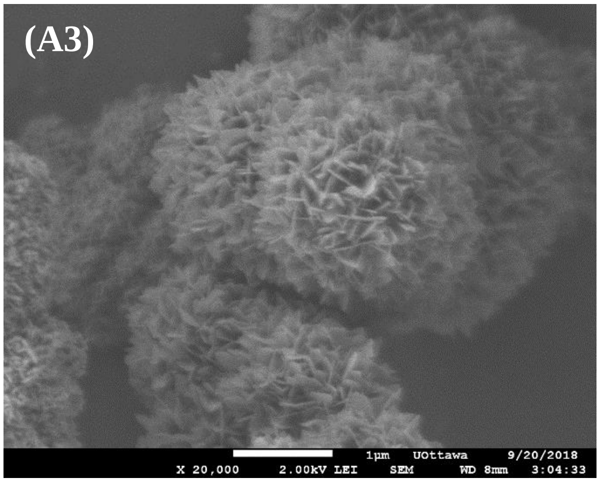
(A3)
1µm UOttawa 9/20/2018
X 20,000 2.00kV LEI SEM WD 8mm 3:04:33

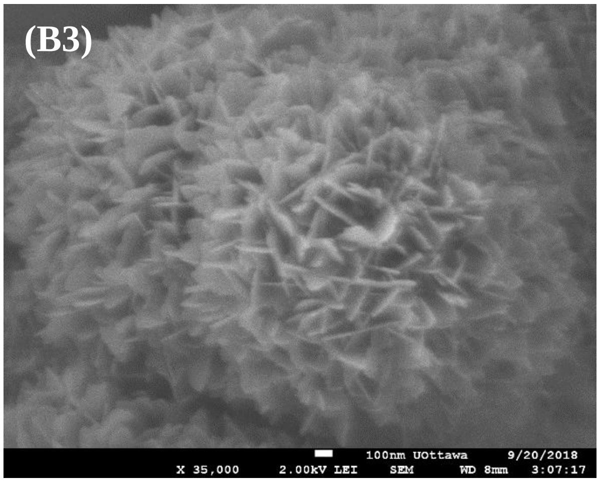
(B3)
100nm UOttawa 9/20/2018
X 35,000 2.00kV LEI SEM WD 8mm 3:07:17

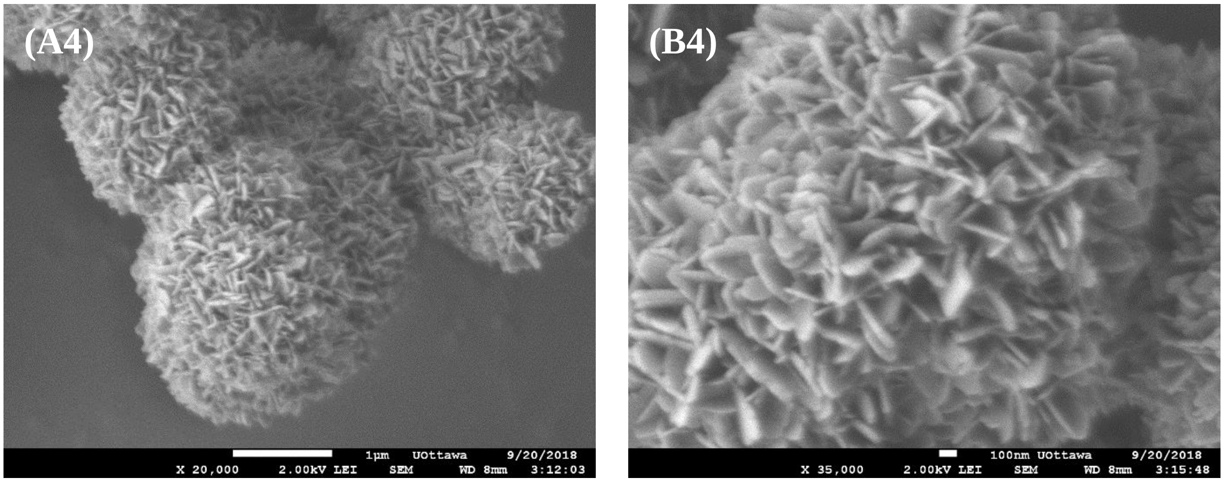

Figure 3-4. SEM images of Bi_2MoO_6 under different synthesis temperatures at (A) low magnification and (B) high magnification: (1) 120°C, (2) 140°C, (3) 160°C, (4) 180°C (reaction time: 20 h; precursor stirring time: 10 min)

To test the effects of reaction time in the autoclave on particle morphology, a constant precursor stirring time of 10 min and a constant reactor temperature of 180°C were used. When the reaction time was increased from 2 h to 25 h (Figure 3.4A4, B4 and 3.5), the plate-like structure came out gradually. After 10 h, plates could be observed clearly (Figure 3.5B3).

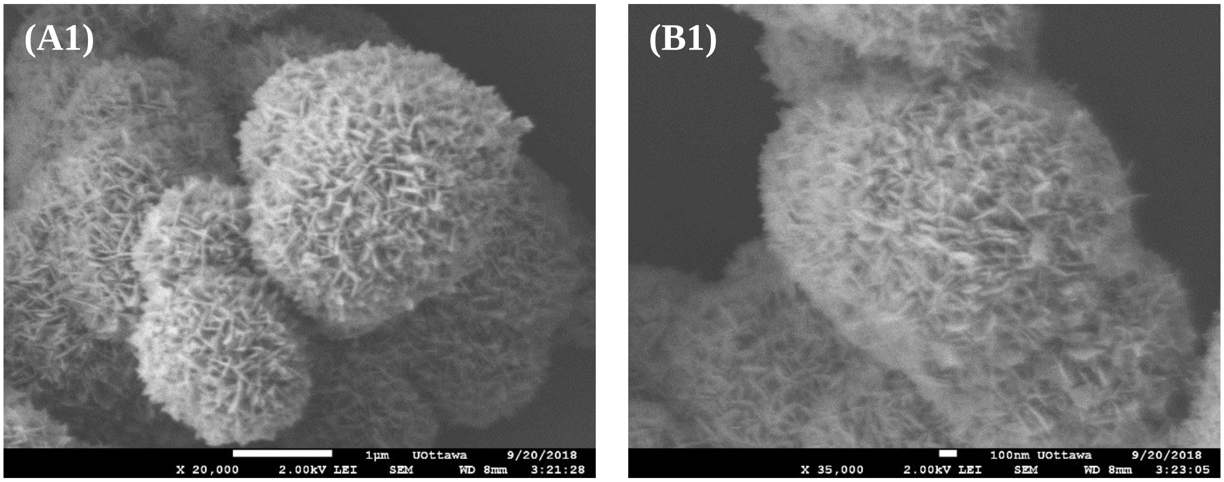

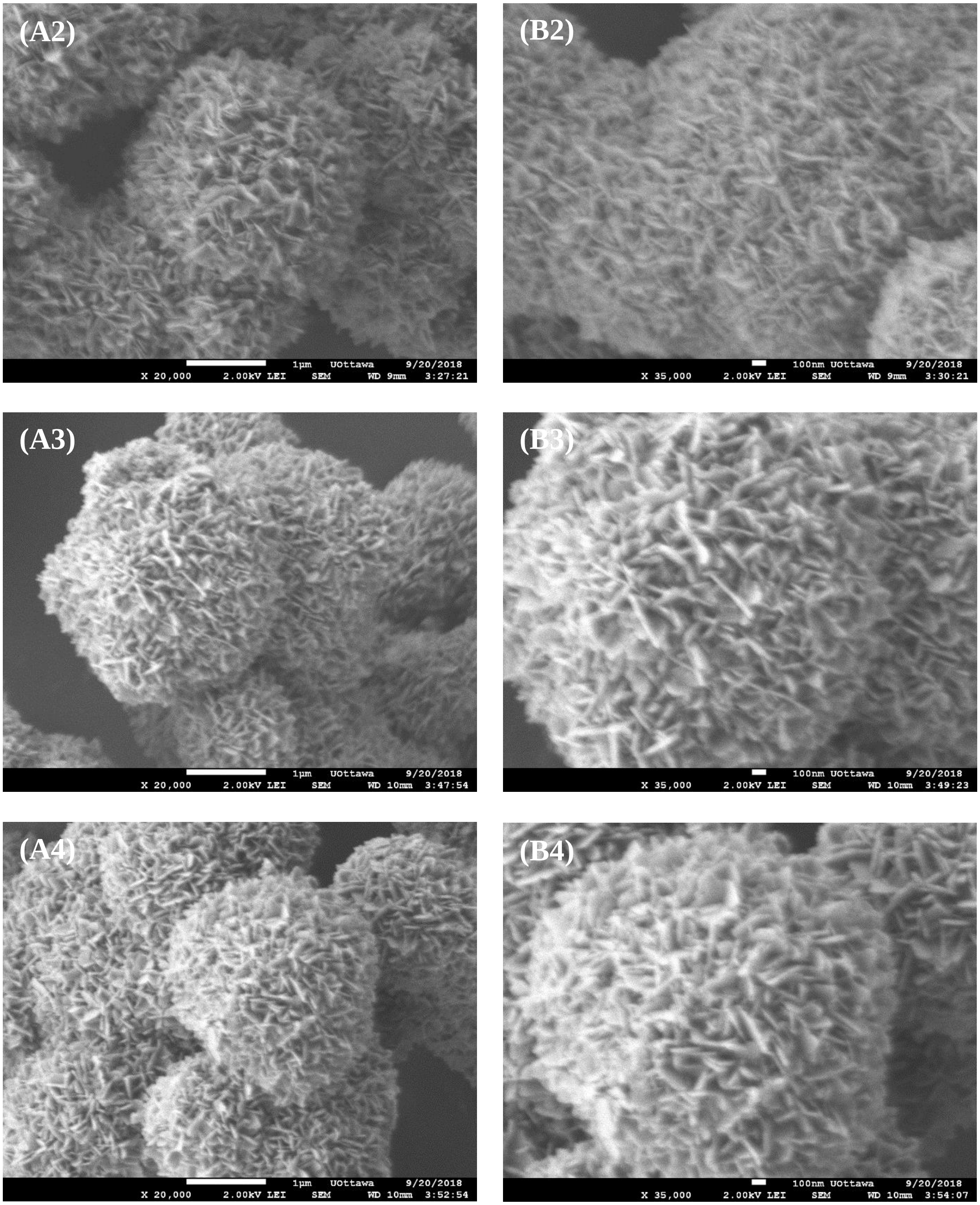
(A2)
1µm UOttawa 9/20/2018
X 20,000 2.00kV LEI SEM WD 9mm 3:27:21
(B2)
100nm UOttawa 9/20/2018
X 35,000 2.00kV LEI SEM WD 9mm 3:30:21
(A3)
1µm UOttawa 9/20/2018
X 20,000 2.00kV LEI SEM WD 10mm 3:47:54
(B3)
100nm UOttawa 9/20/2018
X 35,000 2.00kV LEI SEM WD 10mm 3:49:23
(A4)
1µm UOttawa 9/20/2018
X 20,000 2.00kV LEI SEM WD 10mm 3:52:54
(B4)
100nm UOttawa 9/20/2018
X 35,000 2.00kV LEI SEM WD 10mm 3:54:07

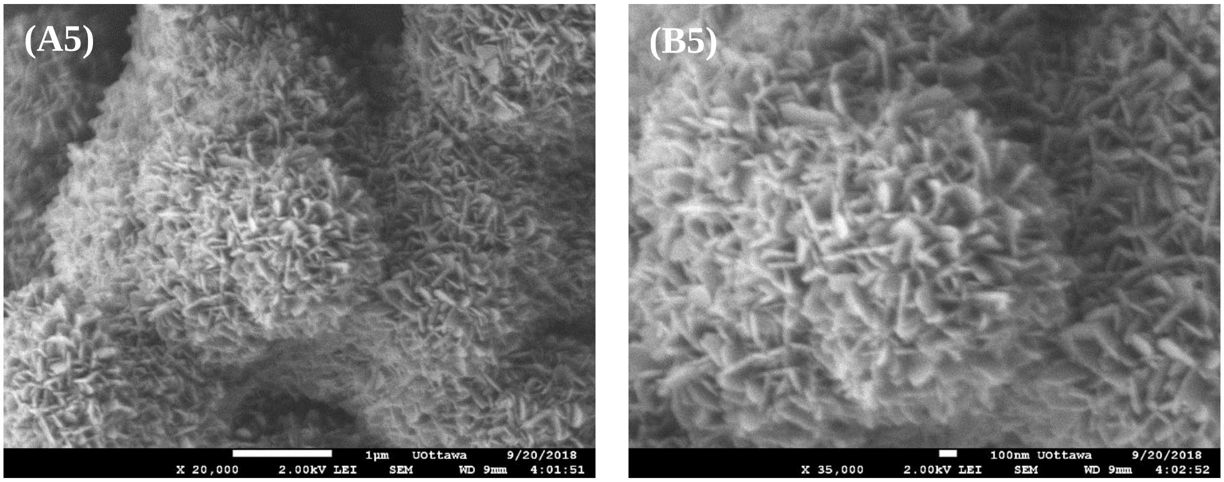

Figure 3-5. SEM images of Bi_2MoO_6 under different synthesis times at (A) low magnification and (B) high magnification: (1) 2 h, (2) 5 h, (3) 10 h, (4) 15 h, (5) 25 h (reaction temperature: 180°C; precursor stirring time: 10 min)

To test the effects of precursor stirring on particle morphology, a constant reactor temperature of 180°C and constant reactor time of 20 h were used. Compared to the effects of reaction temperature and reaction time, the precursor stirring time did not have as significant an impact on the morphology of the particles. It was observed that a longer stirring time led to a less stereoscopic structure. Furthermore, a stirring time of 10 min exhibited a better three-dimensional flower-like structure (Figure 3.4 A4, B4) while after 120-minute stirring, spheres were less independent and more likely to agglomerate together even along with some deformation (Figure 3.6A2, B2).

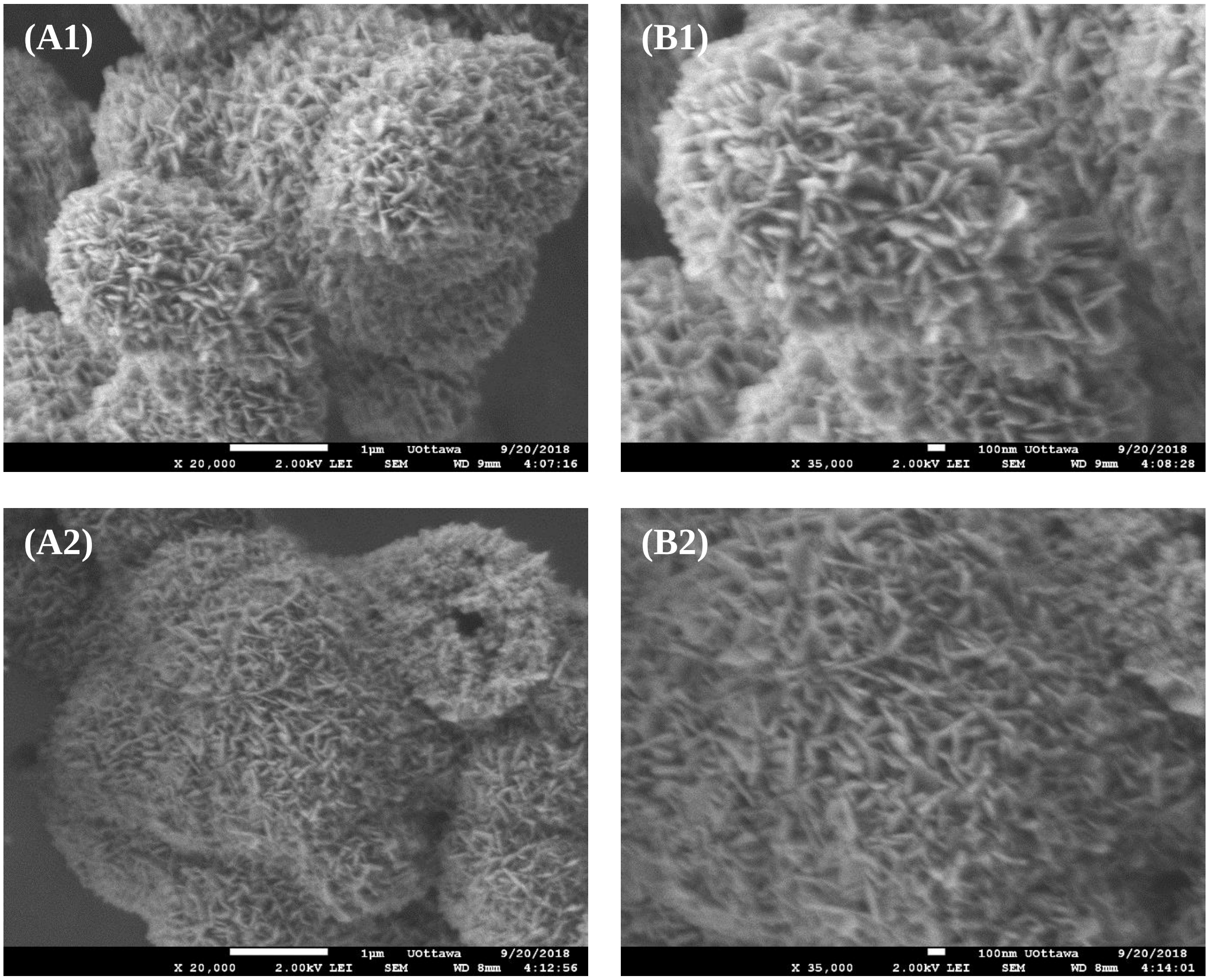

Figure 3-6. SEM images of Bi_2MoO_6 under different precursor stirring times at (A) low magnification and (B) high magnification: (1) 60 min, (2) 120 min (reaction temperature: 180°C; reaction time: 20 h)

3.3.3 Photodegradation of Rhodamine B (RhB)

3.3.3.1 Effect of Reaction Temperature

The photocatalytic performance of Bi_2MoO_6 was examined by RhB decomposition under visible light irradiation. Prior to the photocatalytic experiments, a 30-minute dark reaction was initiated to allow the photocatalysts to reach the adsorption-desorption equilibrium. The adsorption and degradation efficiencies under each reaction synthesis temperature are illustrated in following Figure 3-7 and Table 3-1. In addition, the photolysis of RhB was investigated under same conditions but in the absence of photocatalysts. The self-photodecomposition of RhB of approximately 6% after 120 minutes of irradiation was considered negligible. As the synthesis temperature was increased from 120°C to 180°C, the adsorption ability increased by a factor of 1.6, and the photodegradation activity increased by a factor of 7.0. These results may be attributed to the gradual formation of three-dimensional flower-like structures that provided more surface area for active reaction sites. Also, these stereoscopic plates could reinforce the multiple reflections of visible light, thereby generating more photoinduced electrons and holes due to higher energy harvesting efficiency[22]. In conclusion, the optimized prepared temperature of Bi_2MoO_6 by solvothermal method is 180°C in terms of degradation of RhB under visible light irradiation.

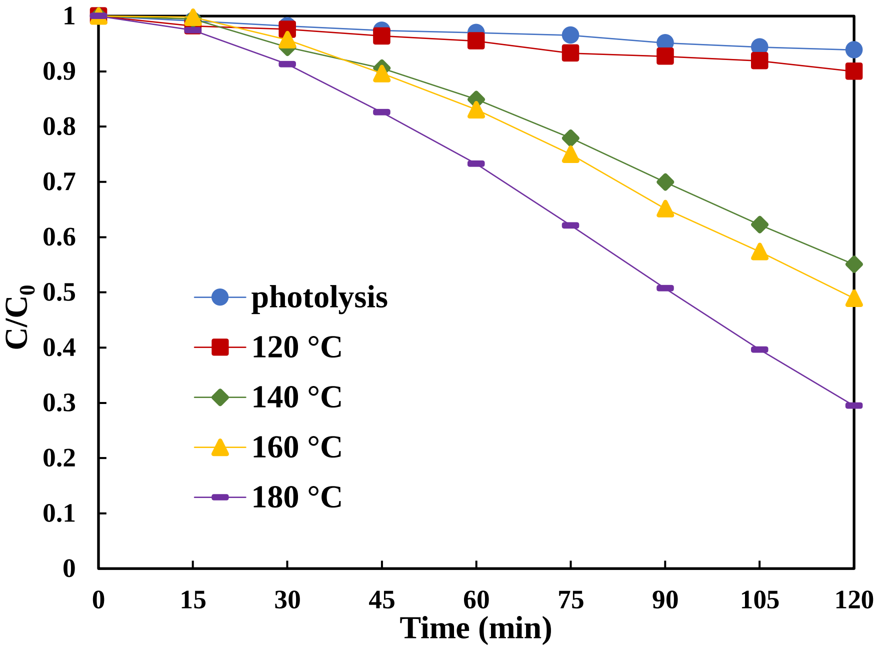

Figure 3-7. Photodegradation performance of Bi_2MoO_6 under different synthesis temperatures (precursor stirring time: 10 min; synthesis time: 20 h; catalysts dosage: 1 g/L; degradation temperature: 20 °C; pH 4.6 and initial RhB concentration: 8 ppm)

Table 3-1. Adsorption ability and degradation ratio of Bi_2MoO_6 under different synthesis temperatures

Temperature	Absorption ability	Degradation ratio at 120 min
120°C	8.15%	10.01%
140°C	10.41%	44.93%
160°C	11.81%	51.08%
180°C	13.09%	70.54%

3.3.3.2 Effect of Reaction Time

Photocatalytic activity of Bi_2MoO_6 under different thermal reaction times was tested, as shown in Figure 3-8 and Table 3-2. The synthesis temperature was controlled at the optimum value found in Section 3.3.3.2, which was 180°C. Similarly, photolysis was applied to prove that RhB was stable under visible light irradiation. The adsorption ability showed a slight increase until 15 h and then remained stable and fluctuated around 13%. As for photocatalytic activity, it continuously climbed up to 70.54% until 20 h, then there was an evident decrease to 56.24% when synthesis time prolonged to 25 h. Interestingly, the removal ratio of RhB increased sharply from 24.20% to 64.75% after a 120-minute irradiation when synthesis time prolonged from 2 h to 5 h while after that, the degradation activity only enhanced slightly for approximately 5% when preparation time increased to 20 h. All these results are in well accordance with the SEM analysis that the formation of the plate-like structure was almost finished after 10 h. Hence, Bi_2MoO_6 synthesized for 20 h at 180°C showed the best photocatalytic performance. In addition, when compared with the effect of synthesis temperature, it is clear that preparation temperature showed a more significant impact on photocatalytic activity.

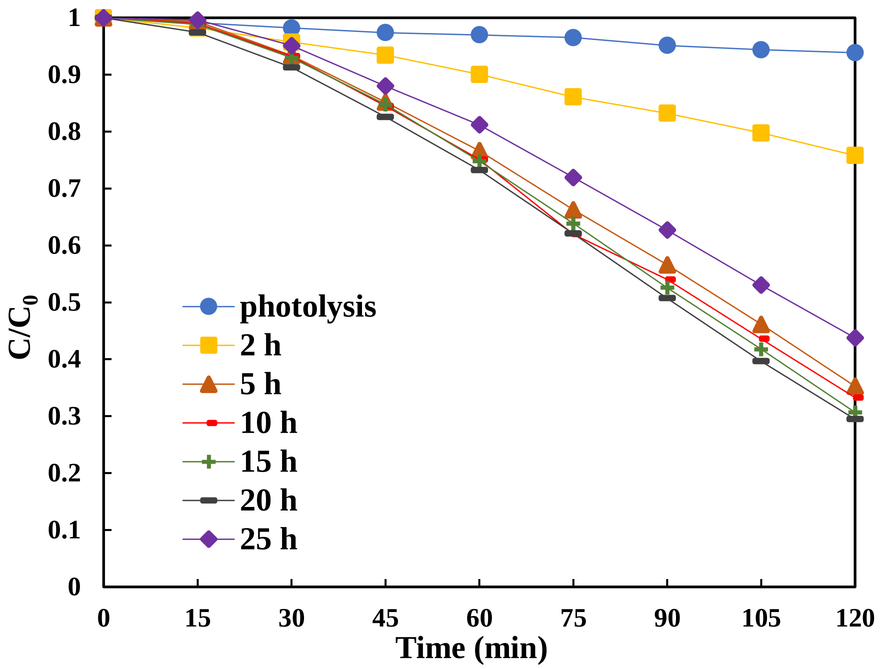

Figure 3-8. Photodegradation performance of Bi_2MoO_6 under different synthesis times (precursor stirring time: 10 min; synthesis temperature: 180°C; catalysts dosage: 1 g/L; degradation temperature: 20 °C; pH 4.6 and initial RhB concentration: 8 ppm)

Table 3-2. Adsorption ability and degradation ratio of Bi_2MoO_6 under different synthesis time

Preparation time (h)	**Absorption ability**	**Degradation ratio at 120 min**
2	9.95%	24.20%
5	11.50%	64.75%
10	11.80%	66.73%
15	13.97%	69.34%
20	13.08%	70.54%
25	13.22%	56.24%

3.3.3.3 Effect of Precursor Stirring Time

Before transferring the solution to the autoclave, the precursor would be stirred for a certain time. To investigate the influence of precursor stirring time, the photocatalytic performance of Bi_2MoO_6 prepared under different stirring times was measured by degrading RhB under visible light irradiation, as shown in the following Figure 3-9 and Table 3-3. Adsorption and degradation abilities decreased with an increase in precursor stirring time by factors of 1.1 and 1.4, respectively. Combined with the SEM images from Figure 3.6, Bi_2MoO_6 stirred for 10 minutes exhibited more intact and less aggregated spherical structures consisting of nanosized plates, thus corresponding to better photocatalytic performance.

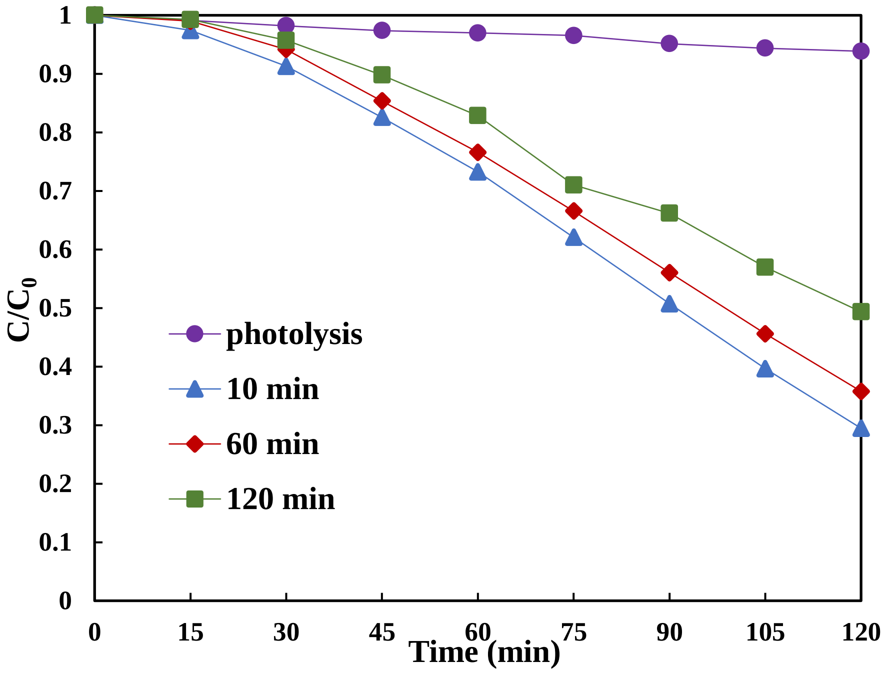

Figure 3-9. Photodegradation performance of Bi_2MoO_6 under different precursor stirring times (synthesis temperature: 20 h; synthesis time: 20 h; catalysts dosage: 1 g/L; degradation temperature: 20 °C; pH 4.6 and initial RhB concentration: 8 ppm)

Table 3-3. Adsorption ability and degradation ratio of Bi_2MoO_6 under different stirring time

Stirring time (min)	Absorption ability	Degradation ratio at 120 min
10	13.09%	70.54%
60	12.35%	64.23%
120	12.16%	50.65%

3.3.3.4 Comparison of Different Synthesis Methods

The solvothermal and hydrothermal synthesis methods for the preparation of Bi_2MoO_6 were compared by performing RhB degradation experiments, as shown in Figures 3-10 and 3-11, and Table 3-4. The solvothermal method was carried out at 180°C for 20 h, and the hydrothermal method (with the addition of acetic acid) was carried out at 120°C for 24 h. Bi_2MoO_6 prepared by the solvothermal method showed a 5.87% higher adsorption ability but 10.00% lower photocatalytic performance than that prepared by the hydrothermal method. A pseudo-first-order model was fitted to study the kinetics of the degradation processes. The solvothermal method showed a worse linear relationship (lower R^2) compared to the hydrothermal method between $-\ln(c/c_0)$ and time, which may be attributed to residual ethylene glycol on the surface of the Bi_2MoO_6 molecules.

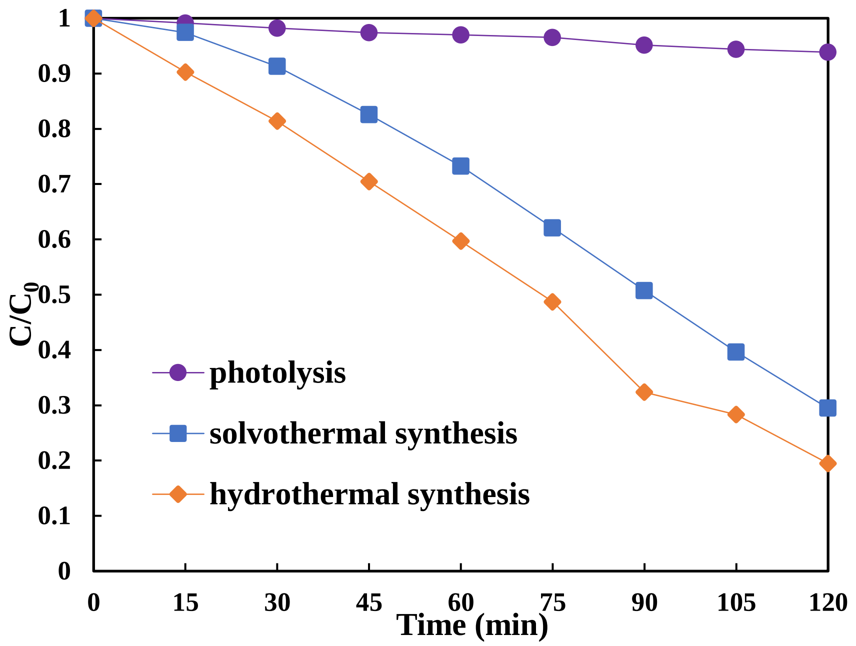

Figure 3-10. Photodegradation performance of Bi_2MoO_6 prepared by different method (catalysts dosage: 1 g/L; degradation temperature: 20 °C; pH 4.6 and initial RhB concentration: 8 ppm)

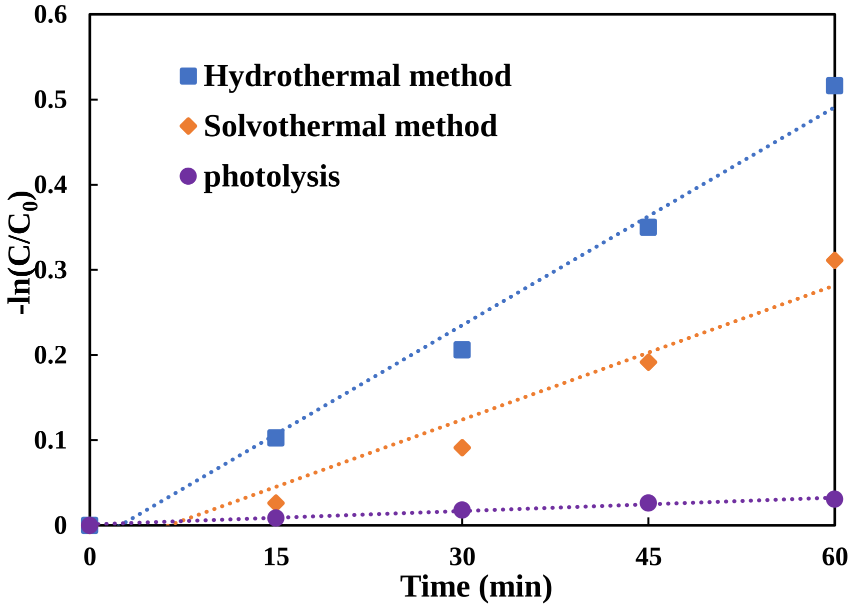

Figure 3-11. Kinetic study for Bi_2MoO_6 prepared by different method (catalysts dosage: 1 g/L; degradation temperature: 20 °C; pH 4.6 and initial RhB concentration: 8 ppm)

Table 3-4. Adsorption ability and degradation ratio, reaction rate constant k and R^2 of Bi_2MoO_6 under different synthesis method

Synthesis method	Absorption ability	Degradation ratio at 120 min	k (min^{-1})	R^2
Hydrothermal	7.22%	80.51%	0.0085	0.9874
Solvothermal	13.09%	70.51%	0.0053	0.9456

3.4 Conclusions

The synthesis conditions including reaction temperature, reaction time and precursor stirring time of Bi_2MoO_6 by the solvothermal method using ethylene glycol and ethanol were optimized. The crystal structures and morphologies under different preparation conditions were analyzed by XRD and SEM, respectively. It was found Bi_2MoO_6 showed the best photocatalytic performance when reaction temperature, reaction time and precursor stirring time were 180°C, 20 h, and 10 min, respectively. This is likely due to the better formation of three-dimensional plate-like structures under these conditions. These plate-like structures increase the surface area and light-harvesting efficiency. This work provides more evidence that Bi_2MoO_6 synthesized by the solvothermal method can be used as an effective photocatalyst in organic pollutants degradation.

3.5 References

1. Fujishima, A., Electrochemical photolysis of water at a semiconductor electrode. Nature, 1972. **238**: p. 37-38.
2. Prairie, M.R., et al., An investigation of titanium dioxide photocatalysis for the treatment of water contaminated with metals and organic chemicals. Environmental Science & Technology, 1993. **27**(9): p. 1776-1782.
3. Lee, S.-Y. and S.-J. Park, TiO_2 photocatalyst for water treatment applications. Journal of Industrial and Engineering Chemistry, 2013. **19**(6): p. 1761-1769.
4. Doll, T.E. and F.H. Frimmel, Removal of selected persistent organic pollutants by heterogeneous photocatalysis in water. Catalysis Today, 2005. **101**(3-4): p. 195-202.
5. Mills, A., R.H. Davies, and D. Worsley, Water purification by semiconductor photocatalysis. Chemical Society Reviews, 1993. **22**(6): p. 417-425.
6. Ao, C. and S. Lee, Indoor air purification by photocatalyst TiO_2 immobilized on an activated carbon filter installed in an air cleaner. Chemical Engineering Science, 2005. **60**(1): p. 103-109.
7. Li, D., et al., Visible-light-driven N− F− codoped TiO_2 photocatalysts. 2. Optical characterization, photocatalysis, and potential application to air purification. Chemistry of Materials, 2005. **17**(10): p. 2596-2602.
8. Pichat, P., et al., Purification/deodorization of indoor air and gaseous effluents by TiO_2 photocatalysis. Catalysis Today, 2000. **63**(2-4): p. 363-369.

9. Dai, W., et al., Hierarchical CeO_2/Bi_2MoO_6 heterostructured nanocomposites for photoreduction of CO_2 into hydrocarbons under visible light irradiation. Applied Surface Science, 2018. **434**: p. 481-491.

10. Yu, J., et al., Enhanced photocatalytic CO_2-reduction activity of anatase TiO_2 by coexposed {001} and {101} facets. Journal of the American Chemical Society, 2014. **136**(25): p. 8839-8842.

11. Liu, L., et al., Photocatalytic CO_2 reduction with H_2O on TiO_2 nanocrystals: Comparison of anatase, rutile, and brookite polymorphs and exploration of surface chemistry. Acs Catalysis, 2012. **2**(8): p. 1817-1828.

12. Wang, K., et al., Sulfur-doped g-C_3N_4 with enhanced photocatalytic CO_2-reduction performance. Applied Catalysis B: Environmental, 2015. **176**: p. 44-52.

13. Meng, X., et al., MoS_2 quantum dots-interspersed Bi_2WO_6 heterostructures for visible light-induced detoxification and disinfection. Applied Catalysis B: Environmental, 2017. **210**: p. 160-172.

14. Yu, J.C., et al., Efficient visible-light-induced photocatalytic disinfection on sulfur-doped nanocrystalline titania. Environmental Science & Technology, 2005. **39**(4): p. 1175-1179.

15. Dong, S., et al., Recent developments in heterogeneous photocatalytic water treatment using visible light-responsive photocatalysts: a review. Rsc Advances, 2015. **5**(19): p. 14610-14630.

16. Meng, X. and Z. Zhang, Pd-doped Bi_2MoO_6 plasmonic photocatalysts with enhanced visible light photocatalytic performance. Applied Surface Science, 2017. **392**: p. 169-180.

17. Bi, J., et al., Simple solvothermal routes to synthesize nanocrystalline Bi_2MoO_6 photocatalysts with different morphologies. Acta Materialia, 2007. **55**(14): p. 4699-4705.

18. Zhang, L., et al., Controllable synthesis of Bi_2MoO_6 and effect of morphology and variation in local structure on photocatalytic activities. Applied Catalysis B: Environmental, 2010. **98**(3-4): p. 138-146.

19. Frit, B. and J. Mercurio, The crystal chemistry and dielectric properties of the Aurivillius family of complex bismuth oxides with perovskite-like layered structures. Journal of Alloys and Compounds, 1992. **188**: p. 27-35.

20. Tian, Y., et al., Solvothermal synthesis and enhanced visible light photocatalytic activity of novel graphitic carbon nitride–Bi_2MoO_6 heterojunctions. Powder Technology, 2014. **267**: p. 126-133.

21. Meng, X. and Z. Zhang, Acetic Acid Assisted to Prepare Bi_2MoO_6 with Visible-Light-Induced Activity. General Chemistry, 2017. **3**(3).

22. Tian, G., et al., Facile solvothermal synthesis of hierarchical flower-like Bi_2MoO_6 hollow spheres as high performance visible-light driven photocatalysts. Journal of Materials Chemistry, 2011. **21**(3): p. 887-892.

23. Zhou, Y.-L., et al., Sphere-like kesterite Cu_2ZnSnS_4 nanoparticles synthesized by a facile solvothermal method. Materials Letters, 2011. **65**(11): p. 1535-1537.

Chapter 4 – Enhanced Photocatalytic Activity of CeO_2/Bi_2MoO_6 Semiconductor Composites Applied in Water Treatment under Visible Light Irradiation

Abstract

As one of the advanced oxidation processes (AOP), photocatalysis can mineralize organic pollutants on the surface of photocatalysts into CO_2 and innocuous inorganic ions by generating oxidizing species under light irradiation. It has great potential for use in pollutant degradation. In this project, the composite photocatalyst CeO_2/Bi_2MoO_6 with enhanced photodegradation activity of RhB under visible light irradiation was successfully synthesized. The as-prepared composites were analyzed by X-ray diffraction (XRD), X-ray photoelectron spectroscopy (XPS), scanning electron microscopy (SEM), high revolution transmission electron microscopy (HRTEM), energy dispersive spectroscopy (EDS) and diffuse-reflection spectroscopy (DRS). The composite with CeO_2 loading of 20wt% showed the highest activity, which was 24% and 83% higher than those of pure Bi_2MoO_6 and pure CeO_2 respectively. The increased performance could be attributed to the formation of the heterojunction between CeO_2 and Bi_2MoO_6, which reduced the recombination of holes and electrons. According to the results of quenching experiments, the most active species in the degradation process were photoinduced holes, while superoxide radicals ($O_2^{\bullet -}$) also played an active role, and hydroxyl radicals (•OH) had a negligible effect. The effects of some operating parameters on the degradation process including temperature, pH, RhB initial concentration and catalyst dosage were experimentally examined and the results were discussed.

Key words: Photodegradation, CeO_2/Bi_2MoO_6 heterojunction, RhB, visible light, water treatment

4.1 Introduction

Nowadays, an increasing attention has been paid to wastewater treatment. Wastewater effluent contains large amounts of organic pollutants and heavy metals that threaten not only human health but also the safety of the environment, especially marine ecosystems. As a result, various methods including adsorption[1], chemical oxidative processes[2] and biodegradation[2, 3] have been developed to remove containments from these waste streams. However, currently available physical technologies such as adsorption, precipitation or coagulation mainly focus on phase transfer, where the final products are still difficult to thoroughly degrade[4-6]. Other chemical or biological methods have other drawbacks, including high operation costs, generation of toxic secondary pollutants and small-scale application[7, 8]. As one of the advanced oxidation processes (AOP), photocatalysis has made a significant improvement in wastewater degradation. Photocatalyzed reactions are triggered by the absorption of light energy of suitable wavelength on the surface of a photocatalyst to generate reactive species that can then degrade pollutants into innocuous products.[9, 10]. Compared with other wastewater treatment technologies, photocatalysis has advantages such as low costs, mild operating conditions, no secondary pollution generation and complete mineralization that makes it applicable in environmental remediation[11-13]. However, there are still some obstacles that limit its wide application in industry, such as charge recombination of some semiconductor photocatalysts, leading to low photocatalytic activity and limited absorption ability in the region of visible light[9].

Cerium dioxide (CeO_2) has drawn increasing attention in photocatalysis for its wide range of advantages, such as distinct optical and electrical characteristics, good stability, nontoxicity and low cost[14-16]. Apart from a longer lifetime that photoinduced charge carriers of CeO_2 possess than TiO_2, the existence of unique Ce^{3+}/Ce^{4+} oxidation states makes it easy to store and release oxygen, and facilitates electron transfer as well[16-19]. Despite these merits, the large band gap of CeO_2, similar to that of TiO_2, hinders its photocatalytic performance, thus preventing its large-scale application[20]. Fortunately, coupling with other semiconductors such as $BiVO_4$[20], TiO_2[21], BiOI[22], Bi_2O_3[23], have been reported that can effectively enhance the visible light absorption and electron-hole pair separation efficiency, thus increasing the photocatalytic activity. Bismuth molybdate (Bi_2MoO_6), as one of the typical Aurivillius oxides whose common formula can be summarized as $Bi_2A_{n-1}B_nO_{3n+3}$ (A = Ca, Sr, Ba, Pb, Bi, Na, or K; B = Ti, Nb, Ta, Mo, W, or Fe), has been a promising visible-light-driven photocatalyst for recent years due to its unique layered structure and relatively narrow band gap (2.5-2.8 eV)[24, 25]. The VB of Bi_2MoO_6 is hybridized by the 6s orbital of Bi and 2p orbital of O, which facilitate the transfer of photogenerated electrons and holes[26]. However, the narrow band gap also leads to a low quantum yield, attributed to the fast recombination of photogenerated electrons and holes. To overcome this defect, heterojunctions formed between Bi_2MoO_6 and other materials including MoS_2[27], $Bi_2O_2CO_3$[28], graphene[29], CdS[30], can be used.

In the present study, CeO_2/Bi_2MoO_6 composites with different CeO_2 loading content were synthesized by the wet impregnation method. The increase in photocatalytic activity in RhB degradation under visible light irradiation was observed, indicating the successful formation of the Type II alignment heterojunction between the two semiconductors, which could assist the separation of photoinduced electrons and holes. The chemical and optical properties of the composites were analyzed. The cycling test was applied to check the composites' stability. A possible degradation pathway was discussed according to the UV-vis spectra. A more feasible mechanism of photodegradation in this system was proposed according to the results of quenching experiments and calculation of band structures. Finally, the effects of some operating parameters including temperature, pH, photocatalyst dosage and initial RhB concentration were analyzed as well.

4.2 Experimental

4.2.1 Synthesis of CeO_2 Nanoparticles

All chemical materials were supplied by Fisher Scientific and Sigma Aldrich. CeO_2 nanoparticles were synthesized by homogenous precipitation method using $Ce(NO_3)_3•6H_2O$ and NaOH. 1.95 mmol $Ce(NO_3)_3•6H_2O$ was added into 20 mL of DDW and stirred for 30 min in a 65°C water bath. 6 mmol NaOH was dissolved in 20 mL of DDW and then added dropwise to the $Ce(NO_3)_3•6H_2O$ solution. A yellow precipitate formed immediately, gradually turning to purple as the NaOH solution was added. The suspension was stirred at 65°C for 2 h, and then maintained at room temperature until it became yellow. The precipitate was centrifuged, washed separately by distilled water and ethanol twice, respectively, and dried at 60°C overnight. Then, the sample was calcined at 500°C for 2 h. Finally, the sample was stored for future use.

4.2.2 Synthesis of Plate-like Bi_2MoO_6

Bi_2MoO_6 was prepared by the hydrothermal method using $Bi(NO_3)_3$•$5H_2O$ and Na_2MoO_4•$2H_2O$. 0.485 g of $Bi(NO_3)_3$•$5H_2O$ was dissolved in 5 mL of acetic acid (HAc) and stirred for 20 min. 0.121 g of Na_2MoO_4•$2H_2O$ was dissolved in 20 mL DDW and added dropwise to the previous solution, causing a white precipitate to form. The mixture was stirred for an additional 20 min. The suspension was then transferred into a 45 mL Teflon-lined stainless-steel autoclave and heated to 120°C for 24 h. After the autoclave cooled down to room temperature, the yellowish precipitates were filtered and washed several times, first by DDW, and then by ethanol. The sample was then dried at 60°C for 12 h and collected.

4.2.3 Synthesis of CeO_2/Bi_2MoO_6 Composites

CeO_2/Bi_2MoO_6 composites were prepared by the wet impregnation method at room temperature. 0.2 g catalyst containing different amounts of CeO_2 (10 wt%, 20 wt%, and 40 wt%) was added into a 20 mL mixture of DDW and ethanol (1:1 by volume). The suspension was stirred in the fume hood uncovered at room temperature until the liquid phase completely evaporated. The sample was then dried at 60°C overnight and stored for characterization.

4.2.4 Characterization

The crystallinity of samples was analyzed by X-ray powder diffraction (Bruker-AXS, Karlsruhe, Germany) with Cu-Kα radiation (λ=0.15418 nm) from 20° to 80° (2θ). A Kratos Nova AXIS spectrometer equipped with an Al X-ray source (XPS) was applied to test the element composition and chemical states on the surface of the selected sample. The structure and surface morphology of samples were obtained by scanning electron microscopy (SEM). The SEM was also connected to an energy-dispersive X-ray spectroscopy (EDS). Transmission electron microscopy (TEM) was employed to measure the lattice fringes of the sample. The optical properties of samples were detected by ultraviolet-visible (UV-Vis) diffuse reflectance spectra (DRS) by a Thermo Evolution 300 Spectrophotometer.

4.2.5 Photocatalytic Performance Measurement

The photocatalytic performance of CeO_2/Bi_2MoO_6 composite, pure CeO_2 and pure Bi_2MoO_6 were tested in a slurry batch photoreactor. The photoreactor comprised a 250 mL beaker outfitted with a thermostatic water bath. The temperature of the reactor was stabilized at a constant value. Light irradiation was provided by a 300 W halogen tungsten bulb (Ushio) including a UV cut-off filter placed under the lamp to target the visible light source (wavelength over 410 nm). All these apparatuses were set in a constructive shelter to minimize the influence of outside light. In each experiment, 100 mL RhB aqueous solution with a certain concentration was used as the degradation substrate. Under constant magnetic stirring speed, the substrate and a certain amount of catalyst were added in the beaker. Before light irradiation, 30-min dark reaction was used to allow the catalyst to reach the absorption-desorption equilibrium. Then, the light was turned on and the photodegradation process started. Every 15 minutes, a 1 mL suspension was collected in a 1.5 mL tube by a pipette and centrifuged under 10000 rpm for 5 min to separate the clear supernatant. The supernatant was characterized by UV–vis spectrophotometry (Genesys 10 UV, Thermo Scientific) against the characteristic absorbance peak of RhB (554 nm). The photodegradation performance can be calculated by Equation 3-1.

To study the process of photodegradation, another UV–vis spectrophotometer (Biochrom Ultrospec 60) was employed to detect the absorption spectra of the supernatant in the range of 300 nm to 700 nm. To investigate the stability of the photocatalyst, a five-cycle degradation using a fixed amount of catalysts was employed. The catalysts were centrifuged and collected after each cycling and then mixed with fresh RhB solution to continue the degradation process until the last cycle. To investigate the main active species during the degradation process, quenching experiments were introduced by using different kinds of scavengers including N_2 bubbling ($O_2^{\bullet -}$), isopropanol (•OH) and EDTA (h^+). The influence of operating factors during photodegradation processes including temperature, initial pH value of RhB solution, initial RhB concentration and photocatalyst dosage were also examined.

4.3 Results and Discussion

4.3.1 XRD Analysis

The crystal structures of as-prepared pure CeO_2, pure Bi_2MoO_6 and composites with different CeO_2 loading ratios were characterized by XRD analysis as shown in Figure 4-1. From the figure, it can be observed that pure CeO_2 matched well with the cubic structure of the XRD standard (JCPDS card no. 89-8436) and pure Bi_2MoO_6 was in accordance with the orthorhombic structure of the XRD standard for γ-Bi_2MoO_6 (JCPDS PDF# 72-1524). Some small impurity peaks appeared in the pure Bi_2MoO_6, which may be attributed to the formation of intermediates and the similar result was found in the literature[31, 32]. When examining the composites, diffraction peaks for both CeO_2 and Bi_2MoO_6 were observed, indicating the co-existence of cubic CeO_2 and orthorhombic Bi_2MoO_6. Some characteristic peaks of CeO_2 and Bi_2MoO_6 overlapped with each other indicating a good combination of these two materials through the use of the wet impregnation method. With an increase in CeO_2 loading content, the intensity of the characteristic diffraction peaks for Bi_2MoO_6 decreased in magnitude. Furthermore, sharp and narrow characteristic peaks suggested that all samples showed good crystallinity. Finally, it can be concluded that cubic CeO_2 was successfully combined with orthorhombic Bi_2MoO_6 by the wet impregnation method.

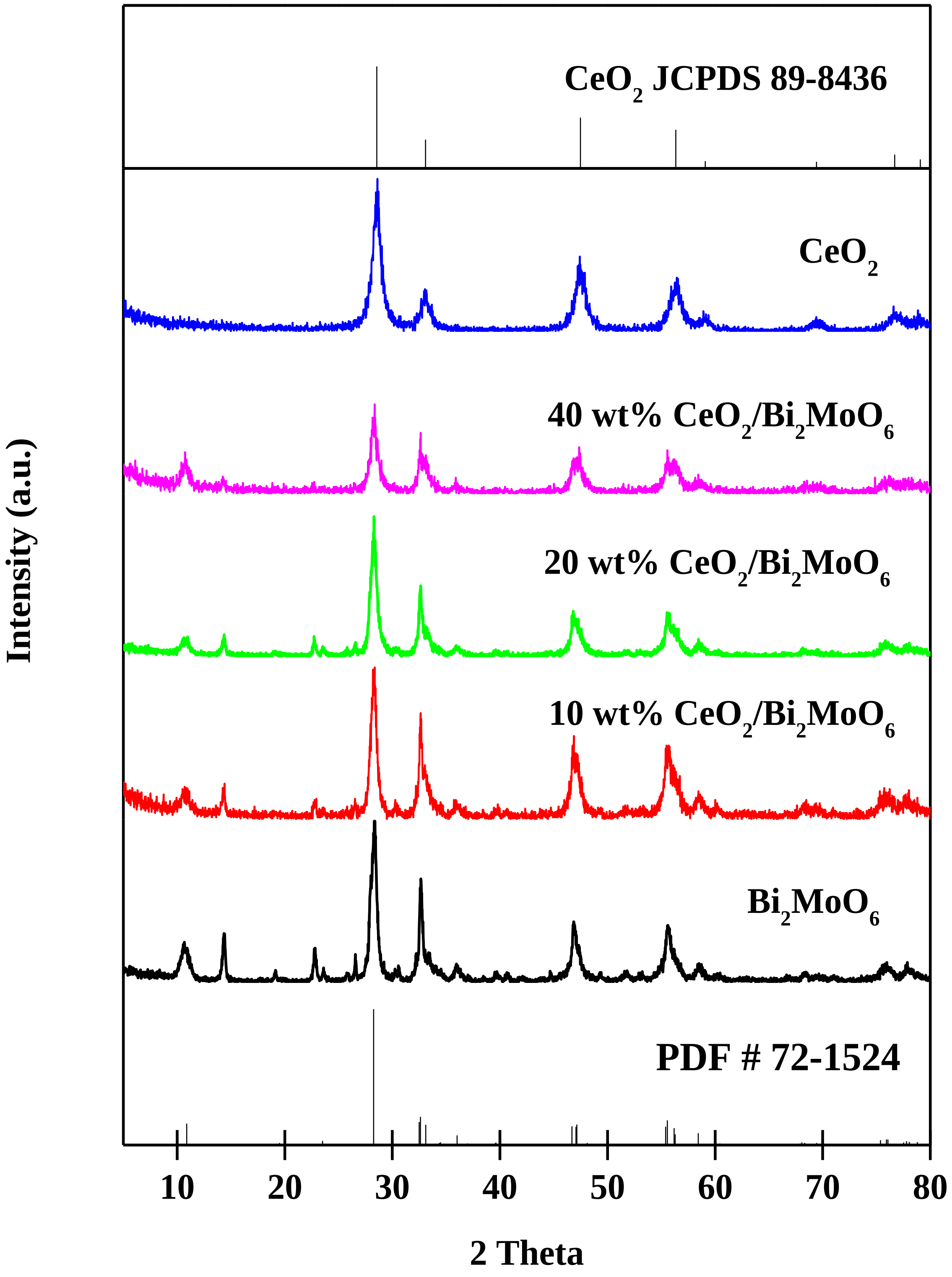

Figure 4-1. XRD pattern of pure CeO_2, pure Bi_2MoO_6, and CeO_2/Bi_2MoO_6 composites

4.3.2 XPS Analysis

The surface elemental composition and chemical states of 20 wt% CeO_2/Bi_2MoO_6 photocatalyst were characterized by XPS analysis. A survey scan and high resolution scan of Bi 4f, Mo 3d, Ce 3d and O 1s were conducted. The results are presented in Figure 4.2-4.6. Adventitious carbon (C 1s, 284.8 eV), a thin layer of carbonaceous material that is deposited on most samples exposed to air, was used to calibrate all the spectra. From Figure 4-2, the elements Bi, Mo, Ce, O were found, and no impurity peaks were observed, indicating that all major components of CeO_2 and Bi_2MoO_6 existed in the composite with no additional elemental contamination.

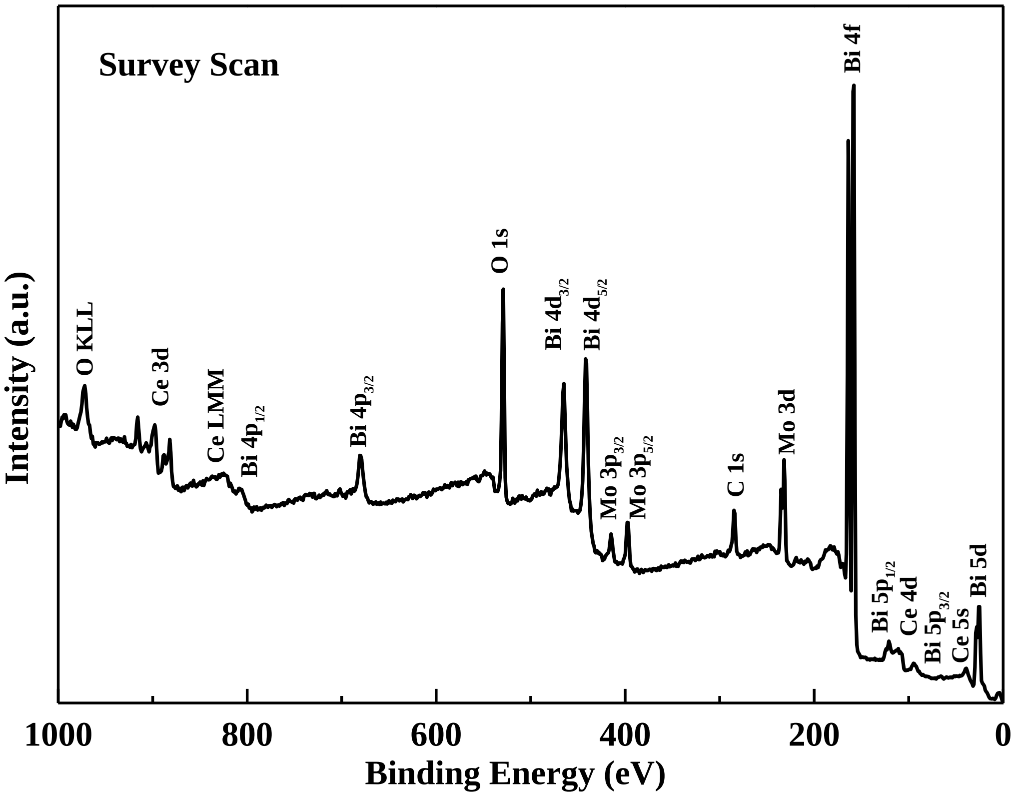

Figure 4-2. XPS scan survey spectra of 20 wt% CeO_2/Bi_2MoO_6 composite

According to Figure 4-3, the Bi 4f spectrum consisted of two peaks located at binding energies of 159.16 eV and 164.47 eV, which corresponded to Bi $4f_{7/2}$ and Bi $4f_{5/2}$, respectively. These peaks could be attributed to the Bi^{3+} ions of Bi_2MoO_6[22, 33].

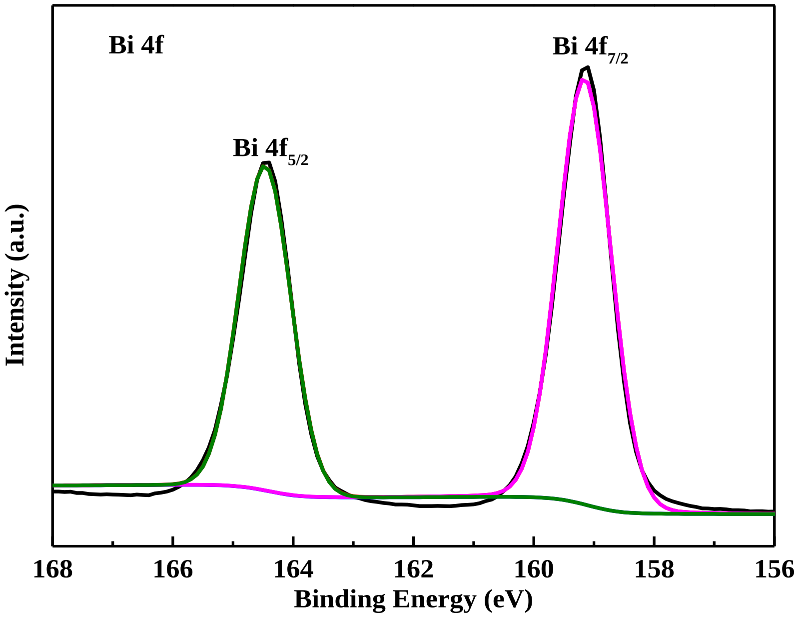

Figure 4-3. XPS high resolution scan spectrum of Bi 4f in the 20 wt% CeO_2/Bi_2MoO_6 composite

Similarly, in Figure 4-4 the Mo 3d spectrum could be fitted to 2 peaks located at binding energies of 232.43 eV and 235.59 eV, ascribed to Mo $3d_{5/2}$ and Mo $3d_{3/2}$, respectively. These two peaks demonstrated that the valence of Mo in the composite was +6[27, 33, 34].

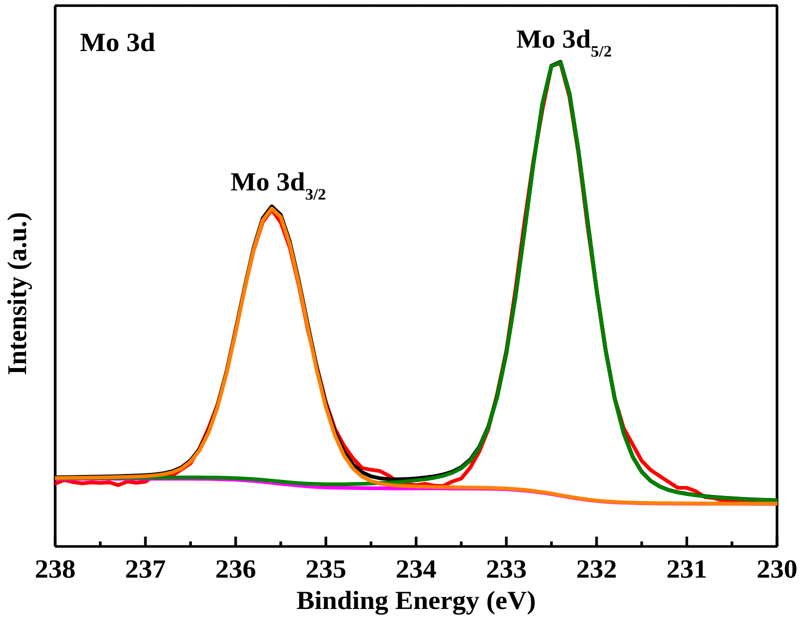

Figure 4-4. XPS high resolution scan spectrum of Mo 3d in the 20 wt% CeO_2/Bi_2MoO_6 composite

As for the spectrum of Ce 3d in Figure 4.5, there are 10 peaks, labelled as v and u, which corresponded to the Ce $3d_{5/2}$ and Ce $3d_{3/2}$ multiplets, respectively. All ten peaks could be divided into five sets of spin-orbit doublets. Three sets of doublet peaks located at binding energies of 916.69 eV (u_0) and 898.27 eV (v_0), 907.49 eV (u_1) and 888.93 eV (v_1), and 900.9 eV (u_2) and 882.34 eV (v_2), corresponding to $Ce3d^94f^0O2p^6$, $Ce3d^94f^1O2p^5$ and $Ce3d^94f^2O2p^4$ respectively, were assigned to the final states of Ce^{4+}. It could be observed when more electrons transferred from O 2p orbitals to Ce 4f orbitals, the binding energies decreased. This is because this kind of electrons transfer would enhance the electron density of Ce^{4+}, leading to a reduced attraction between Ce nuclei and surrounding electrons, thereby reinforcing the repulsion among electrons. The remaining two sets of peaks, denoted as u_3 (v_3) and u_4 (v_4), located at binding energies of 902.90 eV (898.75 eV) and 898.75 eV (880.13 eV) were related to the $3d^94f^2$ and $3d^94f^1$ of Ce^{3+}

cation, respectively[35-38]. These results revealed that Ce species did not exist as a single valence state in the sample, but instead as a mixture of both Ce^{3+} and Ce^{4+}. The concentration of Ce^{3+} species in the sample could be calculated by the integral area ratio of characteristic peaks, shown in Equation 4-1[35, 39]:

$$Ce^{3+}(\%) = \frac{area\ of\ Ce^{3+}}{area\ of\ Ce^{3+} + area\ of\ Ce^{4+}} \times 100\% \qquad \text{(Eq. 4-1)}$$

Using the above equation, it was determined that the surface percentage of Ce^{3+} was approximately 24.13%. This result was attributed to the formation of surface oxygen vacancies, which would aggregate as linear clusters, especially at higher temperature. Thus, some Ce^{4+} would be reduced to Ce^{3+} according to charge balances[40-43].

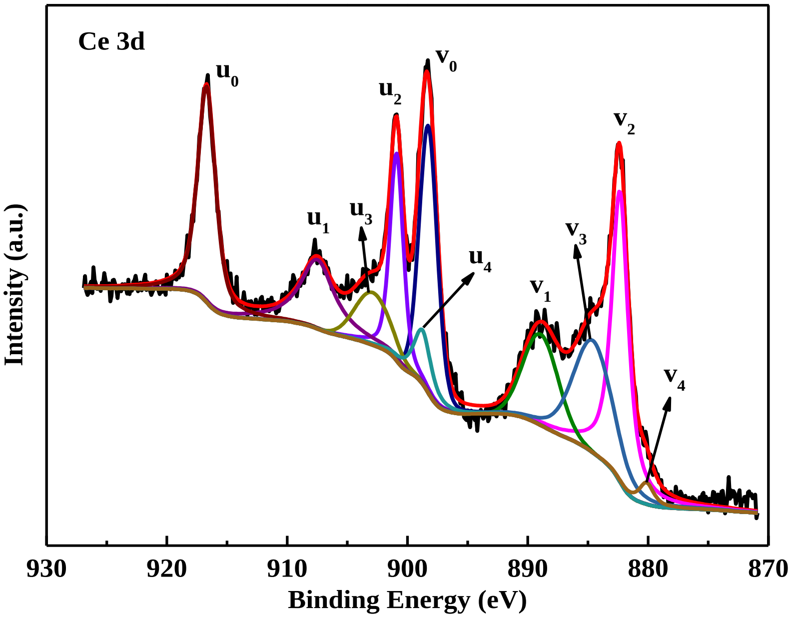

Figure 4-5. XPS high resolution scan spectrum of Ce 3d in the 20 wt% CeO_2/Bi_2MoO_6 composite

As for the spectrum of O 1s in Figure 4-6, it could be deconvoluted to five peaks, revealing that there were five different kinds of O structures in the composite. The peaks located at 530.90 eV and 529.99 eV corresponded to Mo-O and Bi-O bonds, respectively, while the peaks located at binding energies of 529.87 eV and 530.53 eV were related to the Ce-O bond in CeO_2 and Ce_2O_3, respectively. The lowest peak located at 531.13 eV may be associated with surface hydroxyl groups -OH (≈531.6 eV), but due to its wide range in binding energy (width of ≈4 eV), the possibility of a combination of O^{2-} (≈530.0 eV), surface hydroxyl groups -OH (≈531.6 eV) and oxygen atoms in absorbed H_2O (≈533.8 eV) could not be excluded[26, 33, 44]. The existence of these species could act as traps to capture photo-produced electrons (surface oxygen defects O^{2-}) and holes (surface hydroxyl groups -OH and absorbed H_2O), thus reducing the recombination of electrons and holes, which facilitated the enhancement of photoactivity. In addition, surface hydroxyl groups (-OH) and absorbed H_2O could also react with holes to produce hydroxyl groups (·OH), which is one of the main active species with strong oxidative ability during the photodegradation process[36, 45, 46].

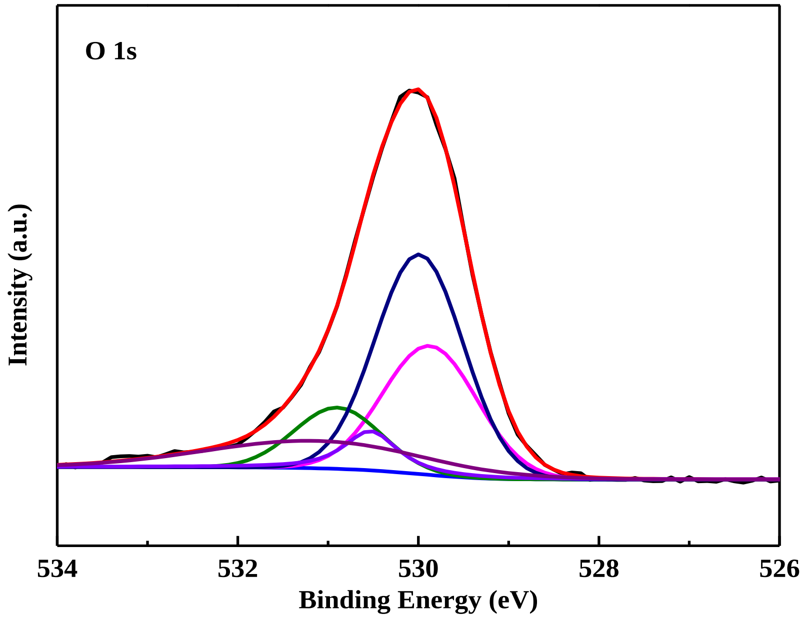

Figure 4-6. XPS high resolution scan spectrum of O 1s in the 20 wt% CeO_2/Bi_2MoO_6 composite

4.3.3 SEM & TEM & EDS Analyses

The morphologies of pure CeO_2, pure Bi_2MoO_6 and as-prepared 20wt% CeO_2/Bi_2MoO_6 composite were obtained by scanning electron microscopy (SEM). The results are shown in Figure 4-7. Pure Bi_2MoO_6 prepared by hydrothermal method showed a flake-like structure sized around 1 μm (Figure 4-7a). Pure CeO_2 had a sponge-like structure comprised of nanoparticles (Figure 4-7b). In the composite material, it could be observed that CeO_2 nanoparticles were successfully combined with Bi_2MoO_6 flakes (Figure 4-7c, d).

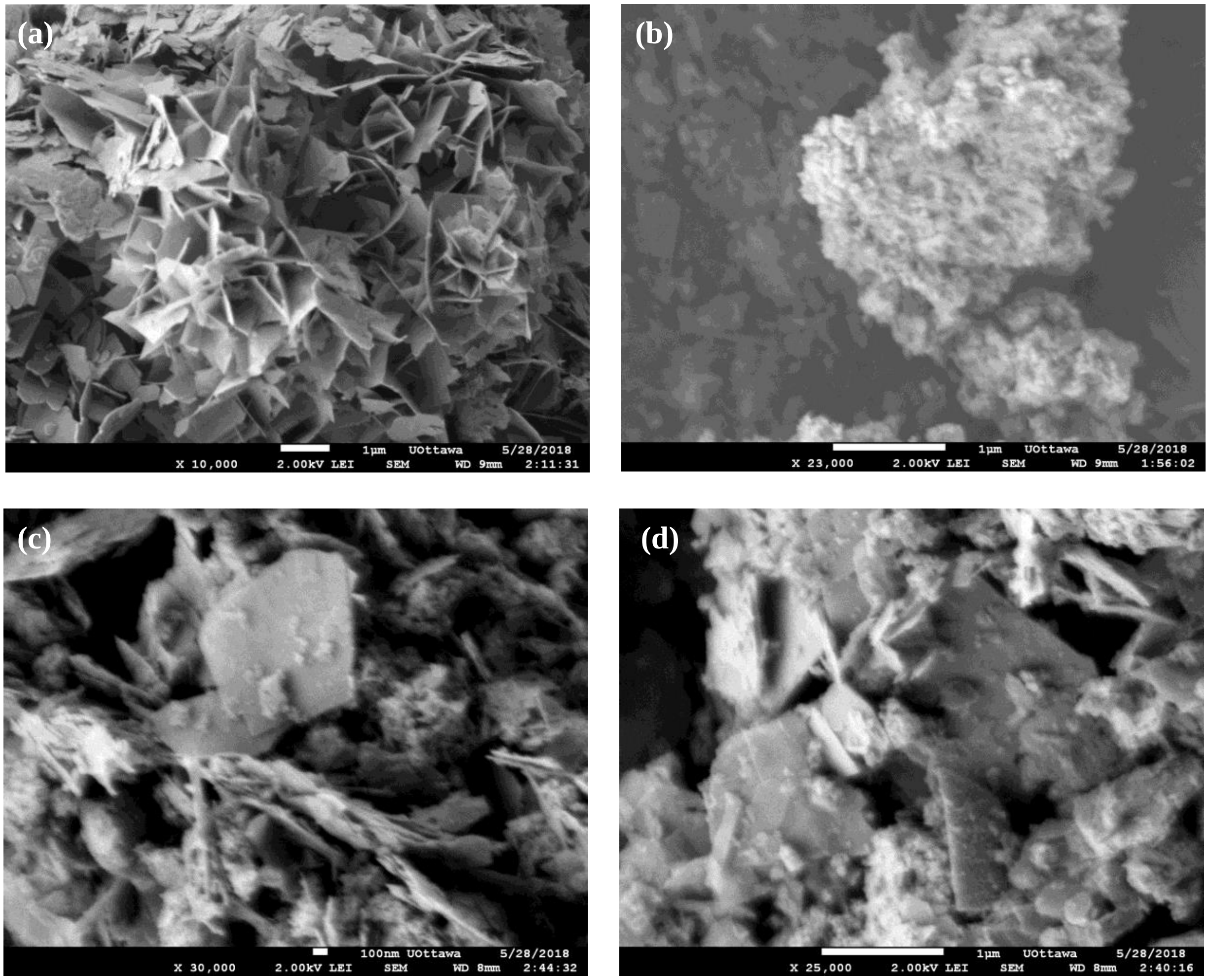

Figure 4-7. SEM images of (a) pure Bi_2MoO_6, (b) pure CeO_2, (c), (d) 20 wt% CeO_2/Bi_2MoO_6 composite

To investigate the lattice structure of the composite, an HRTEM analysis was performed. The results are shown in Figure 4-8. The dark sections were attributed to the overlap of lattice fringes of CeO_2 and Bi_2MoO_6, indicating that CeO_2 with a particle size of approximately 10 nm was successfully loaded on the surface of Bi_2MoO_6. It was also observed that there were two kinds of lattice fringes with different interplanar spacings. The distances of 0.3125 nm and 0.2632 nm between lattice fringes were in well accordance with (111) plane of cubic CeO_2 and (220) plane of orthorhombic Bi_2MoO_6 respectively, further proving the successful combination of CeO_2 nanoparticles and Bi_2MoO_6 flakes.

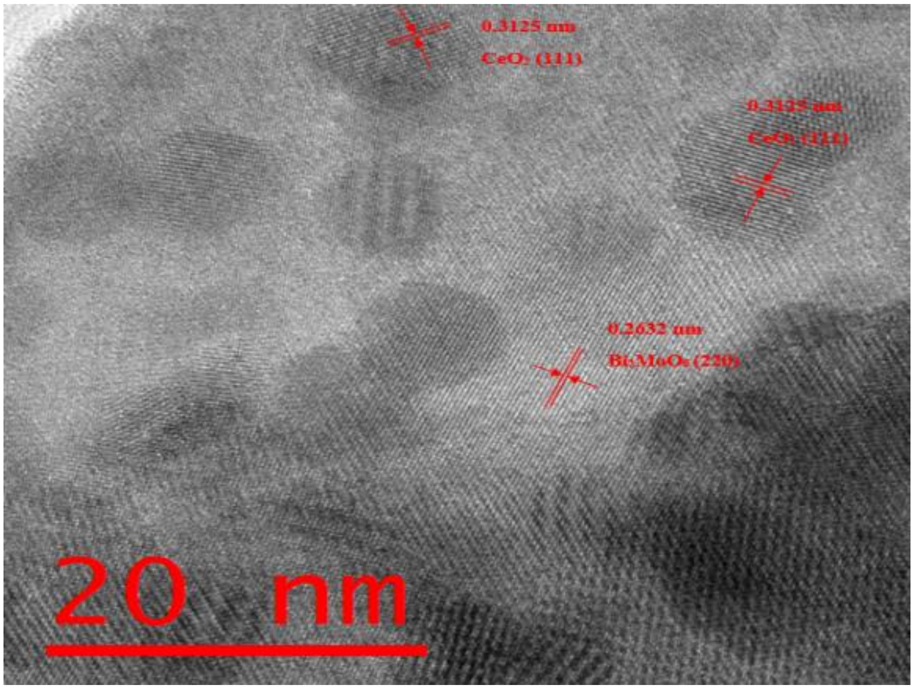

Figure 4-8. HRTEM image of 20wt% CeO_2/Bi_2MoO_6 composite

The EDS spectrum of 20 wt% CeO_2/Bi_2MoO_6 composite was obtained to investigate the fundamental elementary composition. As shown in Figure 4-9, only characteristic peaks for elements Bi, Mo, Ce and O exist, with no impurity peaks in the spectrum, indicating only the existence of CeO_2 and Bi_2MoO_6.

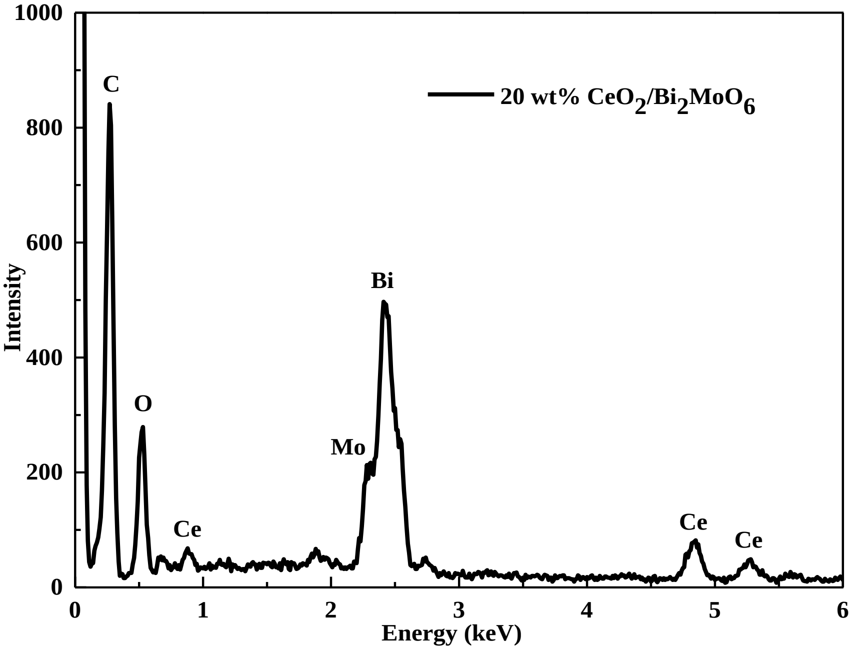

Figure 4-9. EDS of 20 wt% CeO_2/Bi_2MoO_6 composite

4.3.4 UV-Vis Diffused Reflectance Spectra Analysis

Photodegradation activity is associated with the optical properties of semiconductor photocatalysts. As such, the optical absorption properties of the prepared samples were detected by UV-Vis DRS and the spectra are shown in Figure 4-10. All samples show high absorbance in the UV light range; the absorbance started to decrease at ~350 nm. The rapid decline could be ascribed to the band gap transition[31, 47]. It can be seen from Figure 4-10 that pure CeO_2 had a weaker absorption in the visible-light region compared with pure Bi_2MoO_6. For composites, an evident red shift occurred in the absorbance, indicating that composites had a stronger absorption in the visible-light region than that of pure CeO_2, which facilitated the enhancement of photoactivity under visible light irradiation. The red shift was related to the synergistic effects between the two semiconductors, in addition to the presence of defect states due to the existence of Ce^{3+} in CeO_2[36, 46]. The absorption edges were estimated from the spectra in Figure 4-10. The band gap was estimated using Equation 2-1[20]. These results are summarized in Table 4-1.

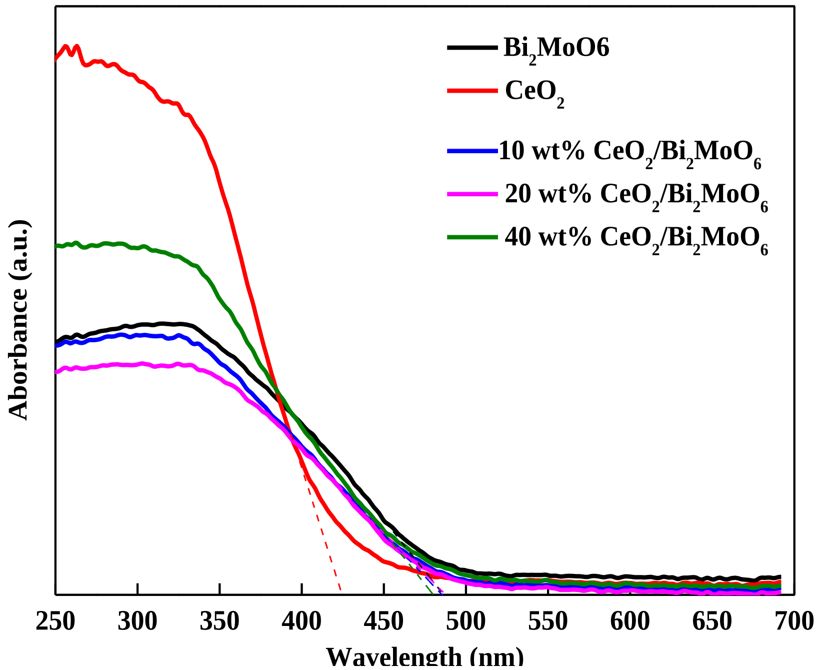

Figure 4-10. UV-Vis DRS of pure CeO_2, pure Bi_2MoO_6 and CeO_2/Bi_2MoO_6 composites with different CeO_2 loading content

Table 4-1. Absorption edges and band gaps of as-prepared samples

Sample Name	**λ_{edge} (nm)**	**E_g (eV)**
CeO_2	424.39	2.92
Bi_2MoO_6	486.24	2.55
10 wt% CeO_2/Bi_2MoO_6	485.34	2.56
20 wt% CeO_2/Bi_2MoO_6	487.76	2.54
40 wt% CeO_2/Bi_2MoO_6	480.10	2.58

It can be seen from Table 4-1 that all composites had lower band gap energy than pure CeO_2, and 20wt% CeO_2/Bi_2MoO_6 composite showed the narrowest band gap. The possible reason was that Bi_2MoO_6 with a relatively narrow band gap of 2.55 eV could act as a sensitizer semiconductor, so the sensitization between these two semiconductors may happen[20, 48]. All these results demonstrated that CeO_2/Bi_2MoO_6 composites had proper band gaps and could act successfully as a promising visible-light-driven photocatalyst in water treatment.

4.3.5 Photodegradation of Rhodamine B (RhB)

4.3.5.1 Effect of the CeO_2 Loading Content in the Composites

The photocatalytic activity of as-prepared samples with different CeO_2 loading content was detected by degrading RhB under visible light irradiation as shown in Figure 4-11. Prior to the photocatalytic experiments, a 30-minute dark reaction was initiated to allow the photocatalysts to reach the adsorption-desorption equilibrium. The absorption data of samples is listed in Table 4-2. Both CeO_2 and Bi_2MoO_6 showed a weak absorption capability of approximately 5-7%, while the composites showed an enhanced absorption ability of up to 2.8 times higher than the pure photocatalysts. This may be due to the long stirring process used during the preparation of the composites.

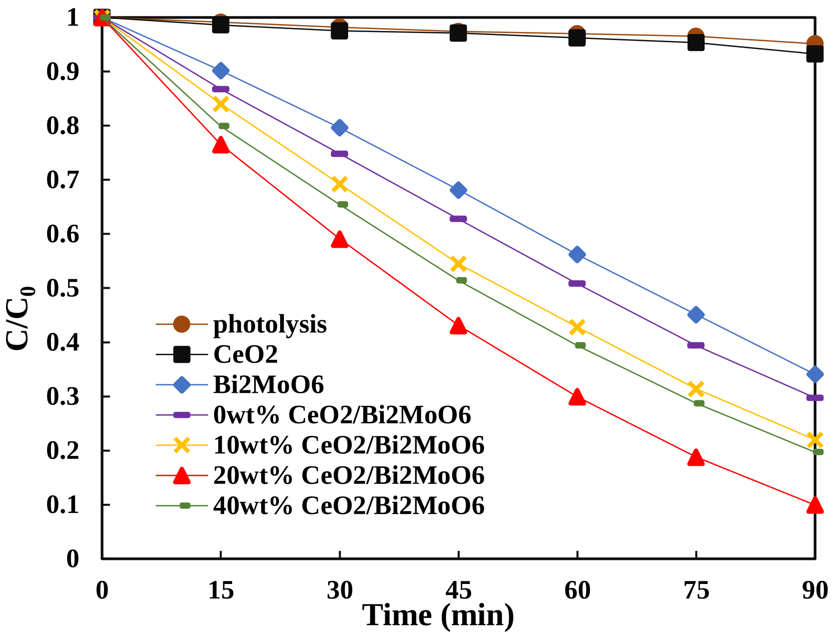

Figure 4-11. Photodegradation performance verse irradiation time of composites with different CeO_2 loading content. (catalysts dosage: 1 g/L; temperature: 20 °C; pH 4.6 and RhB initial concentration: 8 ppm)

Table 4-2. Adsorption ability, photodegradation ratio, reaction rate constant k and R^2 for different catalyst systems

Sample	Absorption ability	Degradation ratio at 90 min	k (min^{-1})	R^2
CeO_2	5.40%	6.73%	0.0006	0.9687
Bi_2MoO_6	6.83%	66.94%	0.0096	0.9847
10wt%	11.54%	78.02%	0.0142	0.9947
20wt%	15.00%	90.07%	0.0199	0.9946
40wt%	14.89%	80.31%	0.0154	0.9973

The photolysis of RhB was also tested, following the same procedure but without adding catalysts. Under 90-minute irradiation, the photolysis ratio was only ~5%, indicating that the substrate remained stable during the process. Using pure CeO_2, the removal ratio of which was close to that of photolysis (~7%) indicating that no significant degradation occurred. Pure Bi_2MoO_6 showed a much higher activity, which reached 66.94% in the 90-minute experiment. The photocatalytic activities of 10 wt% CeO_2/Bi_2MoO_6, 20 wt% CeO_2/Bi_2MoO_6, and 40 wt% CeO_2/Bi_2MoO_6 were 78.02%, 90.07% and 80.31%, respectively with 90-minute visible light irradiation. 20 wt% CeO_2/Bi_2MoO_6 showed the best photocatalytic activity, which was 24.13% and 83.33% higher than those of pure Bi_2MoO_6 and pure CeO_2, respectively. It is clear that CeO_2 loading content had an impact on degradation activity. Increasing the loading content of CeO_2 had a positive effect on photodegradation rate, which could be attributed to the formation of heterojunctions. The heterojunctions suppressed the recombination of photoinduced electrons and holes, increased their separation efficiency and enhanced the photoreaction rate. Thus, to some extent, increasing CeO_2 loading content would produce more heterojunctions and benefit photocatalytic performance. However, after the addition of an optimal amount of CeO_2, the evident decline of photocatalytic activity may be due to less light penetration and decreased number of active sites caused by excessive CeO_2[22, 48, 49]. Notably, the removal ratio of 0 wt% CeO_2/Bi_2MoO_6 was also tested, the reaction activity was a little bit higher than that of pure Bi_2MoO_6 but still much lower than those of the composites. This result indicated that the preparation method had an impact on the photocatalytic degradation perhaps due to the long stirring process used during synthesis and the introduction of ethanol. However, the primary reason was still the formation of heterojunctions between CeO_2 and Bi_2MoO_6.

The kinetics of the degradation process were also studied as shown in Figure 4-12. It can be seen that the degradation data can be fitted with pseudo-first-order kinetics in the first 60 minutes. The integrated rate law for pseudo first-order kinetics is given in Equation 4-2:

$$\ln\left(\frac{C}{C_0}\right) = kt \qquad \text{(Eq. 4-2)}$$

where C_0 and C represent the initial and current concentration of RhB, respectively, k is the reaction rate constant, and t is the illumination time. The calculated values of k and R^2 were listed in Table 4-2. All R^2 values were higher than 0.96, indicating that the data fits the pseudo first-order model well. The 20 wt% CeO_2/Bi_2MoO_6 composite showed the largest reaction rate constant, supporting the result that the composite had the better photocatalytic activity.

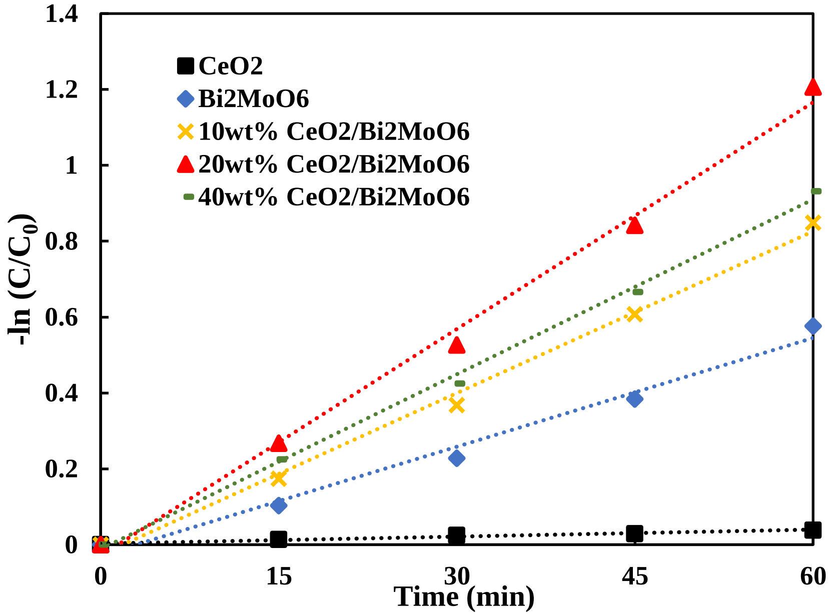

Figure 4-12. Kinetics study of composites with different CeO_2 loading content (catalysts dosage: 1 g/L; temperature: 20 °C; pH 4.6 and initial RhB concentration: 8 ppm)

4.3.5.2 Effect of Photodegradation Temperature

Photodegradation is driven by photonic activation, not thermal activation, and therefore can be performed at room temperature[50]. The influence of different degradation temperatures in the range of 10-40°C using the 20 wt%CeO_2/Bi_2MoO_6 composite at a dosage of 1 g/L, an initial pH of 4.6, and an initial RhB concentration of 8 ppm was tested. The results are summarized in Figure 4-13 and Table 4-3. Overall, increasing the temperature led to an increase in photocatalytic activity of up to 33.67%. The effect is most notable at lower temperatures. When the operating temperature was doubled from 10°C to 20°C, the activity increased by 26.27%. However, when the operating temperature doubled again from 20°C to 40°C, the activity only increased by an additional 7.40%. In the temperature region of 20°C to 80°C, the true activation energy is zero, while the apparent activation energy is a small value. When temperature is lower than 20°C, the desorption of final products limits the photodegradation rate and the apparent activation energy tends to the heat of products adsorbed. As a result, the apparent activation energy increases and the photocatalytic performance decreases[50].

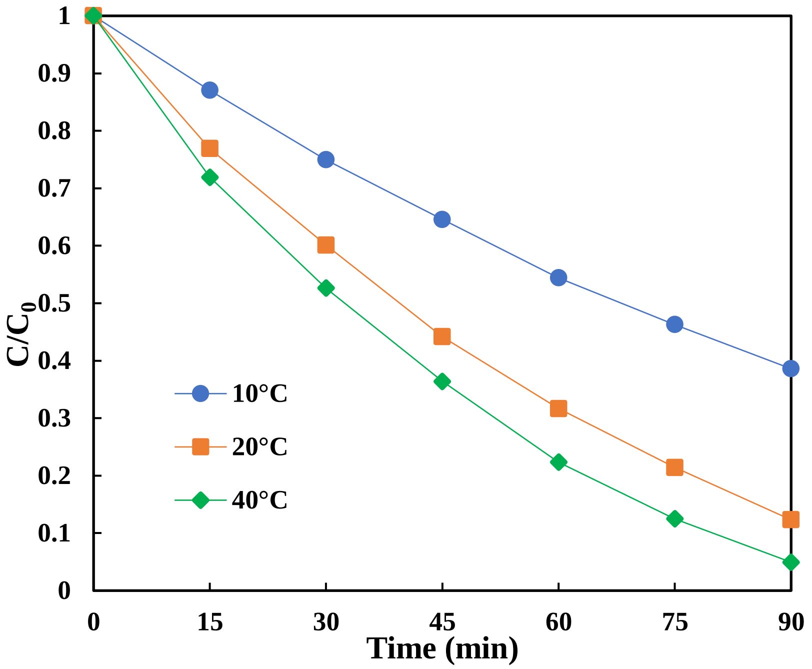

Figure 4-13. Photodegradation performance of 20 wt% CeO_2/Bi_2MoO_6 under different temperatures (catalysts dosage:1 g/L; pH 4.6 and initial RhB concentration: 8 ppm)

Table 4-3. Adsorption ability and photodegradation ratio of 20wt% CeO_2/Bi_2MoO_6 composite at different temperatures

Temperature	Absorption ability	Degradation ratio at 90 min
10°C	11.38%	61.39%
20°C	14.77%	87.66%
40°C	11.40%	95.06%

4.3.5.3 Effect of Initial pH Value of RhB

Initial pH of substrates is an important factor in photodegradation because in industry, wastewater may exhibit a wide range of pH. So photodegradation performance of 20 wt% CeO_2/Bi_2MoO_6

composite under different pH ranging from 4.6 to 12 was carried out. The initial pH of the RhB solution was controlled by adding NaOH solution. The adsorption and photocatalytic performance results are shown in Figure 4-14 and Table 4-4. The degradation activity was relatively high from pH 4.6 to pH 9. There was only a slight change of photodegradation ratio, revealing the composite could remain stable under weak acidic and basic conditions. Sharp decline happened in photodegradation activity was noted at pH 12. This was attributed to the lower absorption capacity of the catalyst at this high pH level, which made RhB molecules more difficult to absorb on the catalyst surface[51]. Highest photocatalytic activity was achieved at pH 9 because alkaline condition benefits the formation of hydroxyl radicals which are one of active species with high oxidative ability[52-54]. At pH 4.6, the lower photocatalytic activity can be attributed to the existence of hydronium ions, which leads to a reduction in the number of active sites[52, 53].

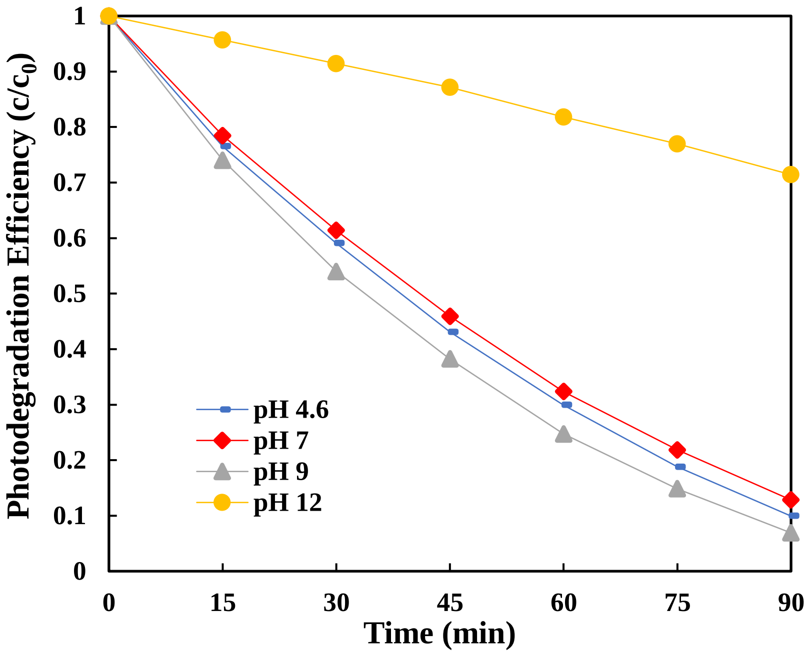

Figure 4-14. Photodegradation performance of 20wt% CeO_2/Bi_2MoO_6 under different pH (catalysts dosage: 1 g/L; temperature: 20 °C and initial RhB concentration: 8 ppm)

Table 4-4. Adsorption ability and photodegradation ratio of 20wt% CeO_2/Bi_2MoO_6 composite at different pH values

pH	Absorption ability	Degradation ratio at 90 min
4.6	15.00%	90.07%
7	38.22%	87.16%
9	21.78%	93.02%
12	7.24%	28.58%

The degradation results of different pH values could also be explained from adsorption aspect. More RhB molecules adsorbed on the catalysts surface favors the increase of photoreaction activity, while excessive adsorption may cover the active sites, thus leading to a decrease in degradation ratio. According to Table 4-4, with the initial increase in adsorption ability, photocatalytic activity also increased. The best performance was achieved at pH 9 with an adsorption ability of 21.78%. However, with a continuous increase in adsorption ability to 38.22% at pH 7, the degradation activity declined.

4.3.5.4 Effect of Catalyst Dosage

Catalyst costs are a significant operating expenditure in any chemical engineering application. So, it is imperative to optimize the catalyst dosage, as this helps reduce costs and maximize output. The photodegradation performance of 20 wt% CeO_2/Bi_2MoO_6 composite with different catalyst dosages ranging from 0 g/L to 3 g/L was carried out. The temperature, initial RhB pH and initial RhB concentration were maintained at 20°C, 4.6 and 8 ppm, respectively. The results are summarized in Figure 4-15 and Table 4-5. Photolysis (i.e. a catalysis dosage of 0 g/L) led to a negligible absorption and degradation of RhB. The adsorption ability at different catalyst dosages varied from 15.00% to 19.97%. The photocatalytic performance increased as a function of catalysis dosage. This increase was most notable at the beginning of the degradation reaction, as shown in Figure 4-16. This may be attributed to the availability of additional active sites for the adsorption of RhB molecules, along with the generation of additional electrons and holes [10, 54]. However, due to excessive catalyst, the turbidity of the suspension would increase, which could increase the light scattering and reduce the light penetration[51, 55, 56]. As a result, photoinduced degradation slowed down. The final degradation ratio was the result of the combined contribution of these two factors. Thus, as catalyst dosage continuously increased, the sharp enhancement in degradation ratio did not occur.

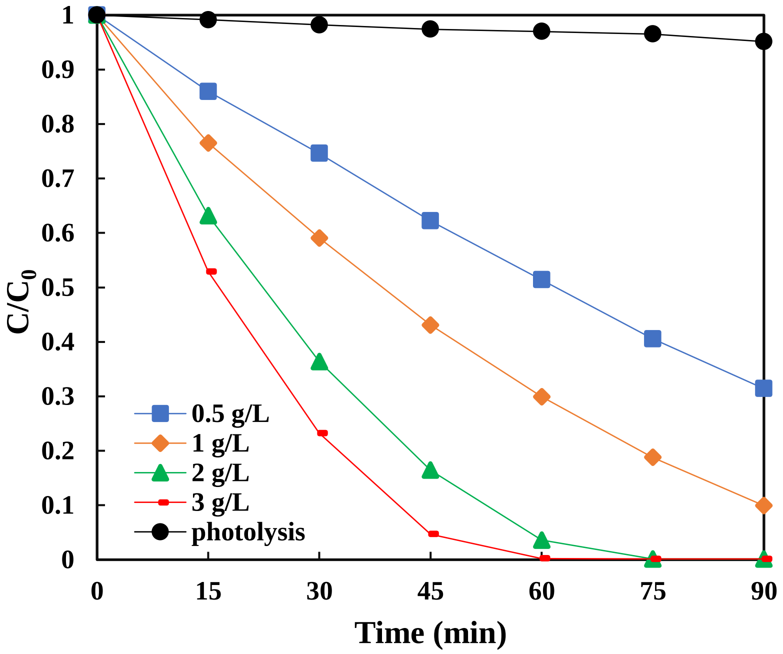

Figure 4-15. Photodegradation performance of 20wt% CeO_2/Bi_2MoO_6 under different catalyst dosages (temperature: 20 °C; pH 4.6 and initial RhB concentration: 8 ppm)

Table 4-5. Adsorption ability and photodegradation ratio of 20wt% CeO_2/Bi_2MoO_6 composite at different catalyst dosages

Catalyst Dosage (g/L)	Absorption ability	Degradation ratio at 45 min	Degradation ratio at 90 min
0 (photolysis)	0.40%	2.61%	4.86%
0.5	16.98%	37.79%	68.59%
1	15.00%	56.91%	90.07%
2	17.16%	83.56%	99.86%
3	19.97%	95.33%	99.86%

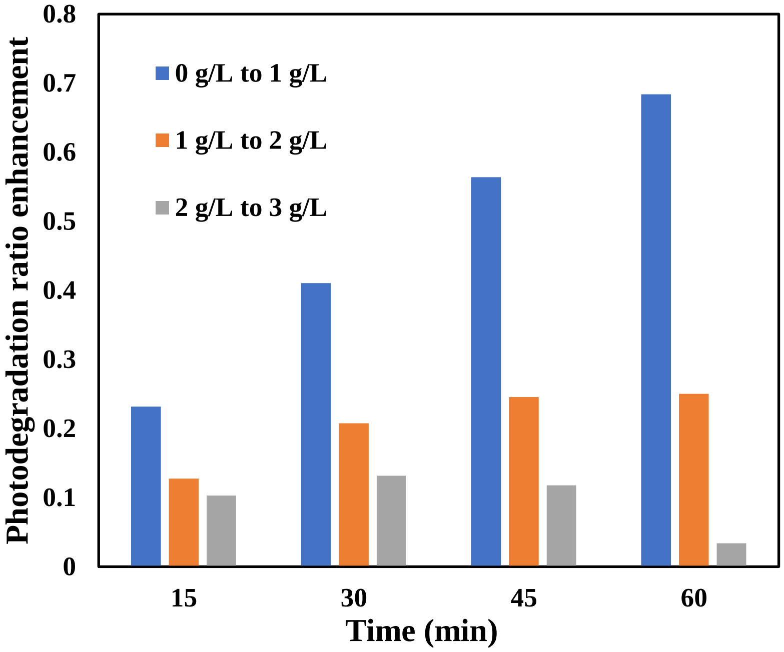

Figure 4-16. Photodegradation ratio enhancement of 20 wt% CeO_2/Bi_2MoO_6 with continuous increase of photocatalyst dosage (temperature: 20 °C; pH 4.6 and initial RhB concentration: 8 ppm)

4.3.5.5 Effect of Initial RhB Concentration

The initial substrate concentration is another important factor in wastewater treatment. Therefore, the removal ratio of RhB with different initial substrate concentrations ranging from 4 ppm to 32 ppm was examined using 20 wt% CeO_2/Bi_2MoO_6 composite as the catalyst. The temperature, pH and catalyst dosage were maintained at 20°C, 4.6 and 1 g/L, respectively. The results are shown in Figure 4-17 and Table 4-6. RhB photolysis was tested at an initial substrate concentration of 8 ppm, as shown in Figure 4-17. It was determined that the effect of photolysis was negligible. At 1 g/L of catalyst, the absorption ability ranged from 15.00 to 21.67%, with the most significant increase occurring when the initial substrate concentration was doubled from 8 ppm to 16 ppm. The degradation activity decreased as a function of increasing initial substrate concentration. The most significant decrease occurred when the initial substrate concentration was doubled from 8 ppm to 16 ppm. Overall, these results indicate that photoreaction is preferential at a lower substrate concentration. The evident decline in degradation with the increase of initial dye concentration could be attributed to three reasons: (1) the competition between adsorption and degradation due to the limited number of active sites caused by constant catalyst dosage [51, 57]; (2) more intermediates would be produced with the increase of RhB concentration, leading to a stronger competition[16, 58]; and (3) the weakness of light irradiation – as the solution is becoming darker with the increase of RhB concentration, more light would be adsorbed and lost before arriving on the catalyst surface. Moreover, excessive RhB molecules would cover the active sites, directly hindering the light irradiation on the surface[16, 51, 59].

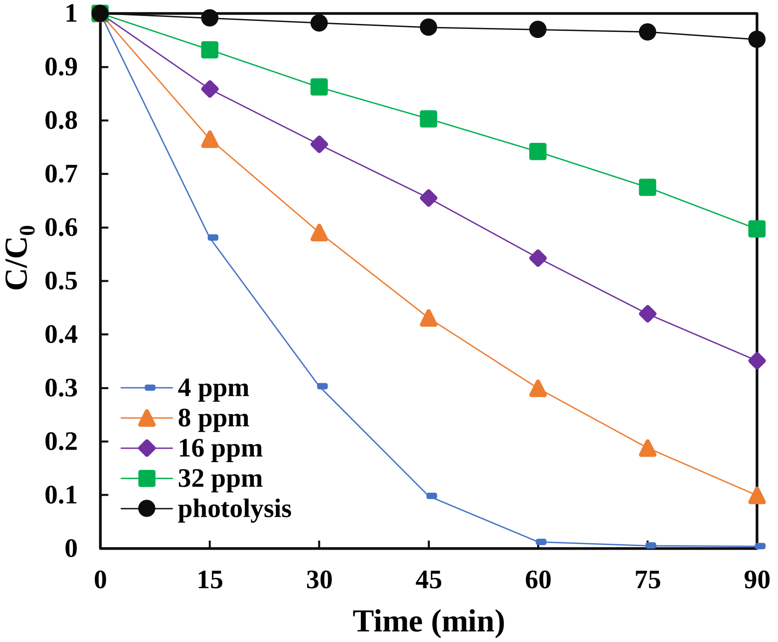

Figure 4-17. Photodegradation performance of 20 wt% CeO_2/Bi_2MoO_6 composite under different initial RhB concentrations (temperature: 20 °C; pH 4.6 and catalyst dosage:1 g/L)

Table 4-6. Adsorption ability and photodegradation ratio of 20 wt% CeO_2/Bi_2MoO_6 composite at different initial RhB concentrations

Initial RhB concentration (ppm)	**Absorption ability**	**Degradation ratio**
4	16.19%	99.59%
8	15.00%	90.07%
16	20.45%	64.91%
32	21.67%	40.29%

4.3.5.6 UV-vis Spectra of RhB (Degradation Pathway)

The pathway of the degradation process was analyzed by UV-vis spectroscopy at as shown in Figure 4-18. Figure 4-19 depicts the variation trends of major absorbance peak wavelengths and relative absorbances over time.

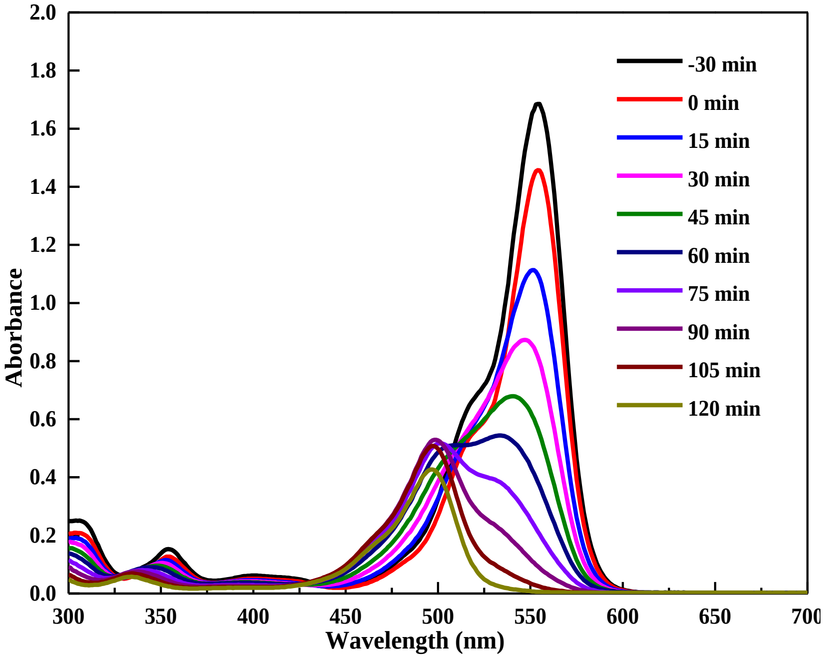

Figure 4-18. UV-vis spectra of RhB under different irradiation times (catalyst: 20wt% CeO_2/Bi_2MoO_6 composite; catalysts dosage: 1 g/L; temperature: 20 °C; pH 4.6 and RhB initial concentration: 8 ppm)

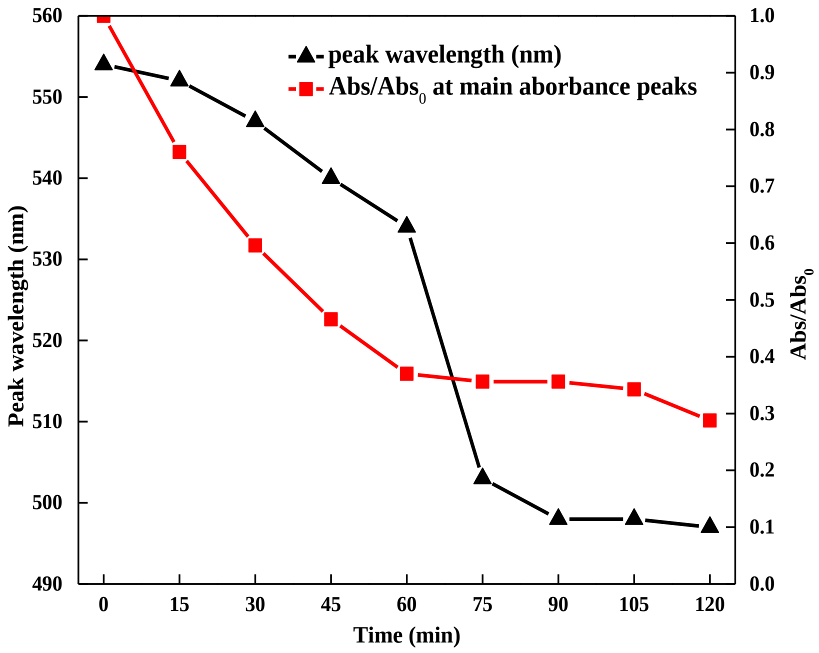

Figure 4-19. Wavelengths of the main absorbance peak and relative absorbances of RhB verse irradiation time

It is reported that there are two competitive pathways for RhB degradation[48, 60-65]. The first pathway is the N-deethylation process, which produces different kinds of deethylation intermediates including N, N, N'-triethyl Rhodamine (TER), N, N'-diethyl Rhodamine (DER), N-ethyl Rhodamine (ER) and Rhodamine, corresponding to peak wavelengths of 539 nm, 522 nm, 510 nm and 498 nm, respectively. These intermediates result in blue shifts in the wavelength. The color of RhB turns from pink to light green when this process is finished. The second pathway is called the "destruction of conjugated structure". The RhB structure is destroyed when •OH radicals attack the aromatic chromophore rings, leading to a decrease in absorption while no wavelength shift occurs. According to the Figure 4-19, it is clear that in the first 90 minutes, blue shifts of peak wavelength took place, indicating that successive deethylation dominated the degradation process, and the color of RhB solution turned to light green gradually. Subsequently, the wavelength of the main absorbance peak remained stable at ~498 nm while the absorption band continuously decreased, demonstrating after decolorization, only the destruction of aromatic rings occurred.

4.3.5.7 Improvement due to Heterojunctions

To further prove that the wet impregnation method is feasible in improving photocatalytic activity, a comparison of photodegradation of RhB between 20 wt% CeO_2/Bi_2MoO_6 composite and a mechanical mixture of CeO_2 (prepared by the homogeneous precipitation method) and Bi_2MoO_6 (prepared by the hydrothermal method) with the same weight ratio was carried out. Similarly, the catalyst dosage, temperature, pH and initial RhB concentration were maintained at 1 g/L, 20°C, 4.6 and 8 ppm, respectively. The results are summarized in Figure 4-20 and Table 4-7. The composite showed the highest adsorption ability of 15.00%, 2.36 times higher than that of the mechanical mixture with the same weight ratio. As for photocatalytic performance, after 90-minute-irradiation, the photodegradation activity of the composite was 30.28% higher than that of the mechanical mixture. The weighted average of the degradation ratios of the pure photocatalysts (20% CeO_2 and 80% Bi_2MoO_6) is 54.90%, which matches well with the degradation ratio of the mechanical mixture (59.79%), suggesting that few or no heterojunctions were formed by simply mechanical mixing the two photocatalysts. The significant improvement in photocatalytic activity of the composite was caused by the formation of heterojunctions. The formation of heterojunctions suppresses the recombination of photoinduced holes and electrons and enhances their separation efficiency, thus leading to an improved degradation performance.

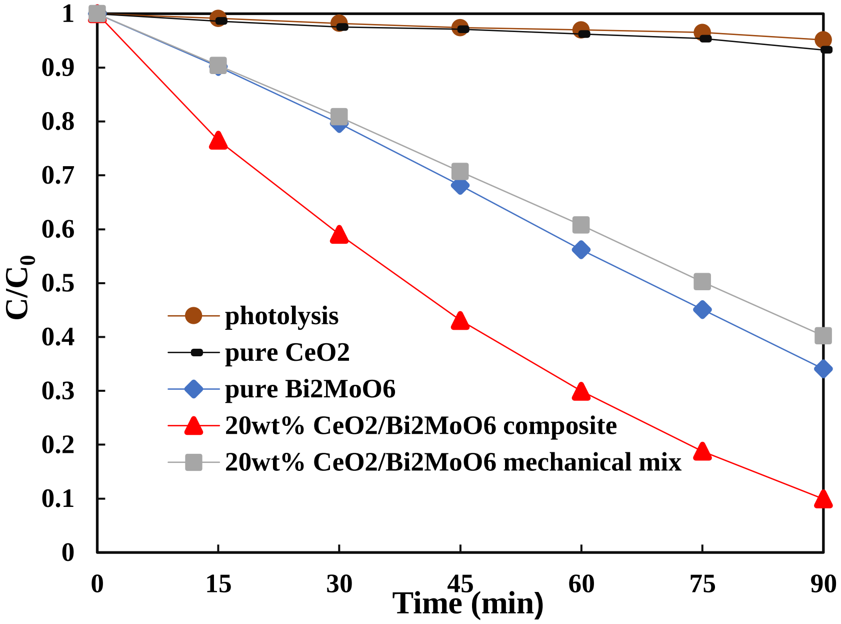

Figure 4-20. Comparison of catalysts synthesized by different method (catalysts dosage: 1 g/L; temperature: 20 °C; pH 4.6 and initial RhB concentration: 8 ppm)

Table 4-7. Adsorption ability and photodegradation ratio of 20wt% CeO_2/Bi_2MoO_6 synthesized by different methods

Samples	**Absorption ability**	**Degradation ratio**
CeO_2	5.40%	6.73%
Bi_2MoO_6	6.83%	66.94%
20 wt% CeO_2/Bi_2MoO_6 composite	15.00%	90.07%
20 wt% CeO_2/Bi_2MoO_6 mechanical mix	6.36%	59.79%

4.3.6 Reusability

It is well known that one of the most important properties of a catalyst is its stability. Hence, to assess the stability of the composite photocatalyst, a cycling test of 5 rounds was carried out. Between each degradation, the photocatalyst was separated from the suspension by centrifugation and mixed with fresh RhB solution. The results are shown in Figure 4-21 and 4-22. The adsorption and photodegradation of the first cycle reached 15.00% and 90.07%, respectively after a 90-minute-irradiation. Then, the absorption ability decreases to ~2% for the remaining cycles. This may be attributed to the intermediates produced during the process, which were not fully decomposed and remained adsorbed on the surface of the catalyst[51]. The degradation activity remained above 80% throughout the five cycles. These results demonstrated that the composite could remain stable after the 5-round-cycling test and be used repeatedly as a highly effective photocatalyst.

The crystal structures of the composite after the cycling test were also characterized by XRD. The results are shown in Figure 4-23. All characteristic peaks appear in both spectra, implying that no obvious structural destruction happened during the long-term repeated degradation experiments. Moreover, the characteristic peaks were almost as sharp in the “after” spectrum, indicating that the composite after the 5-round degradation cycling experiments maintained good crystallinity and remained stable. In conclusion, the composite prepared by the wet impregnation method exhibited excellent stability and could be employed repeatedly, establishing a firm foundation for its further use in industry.

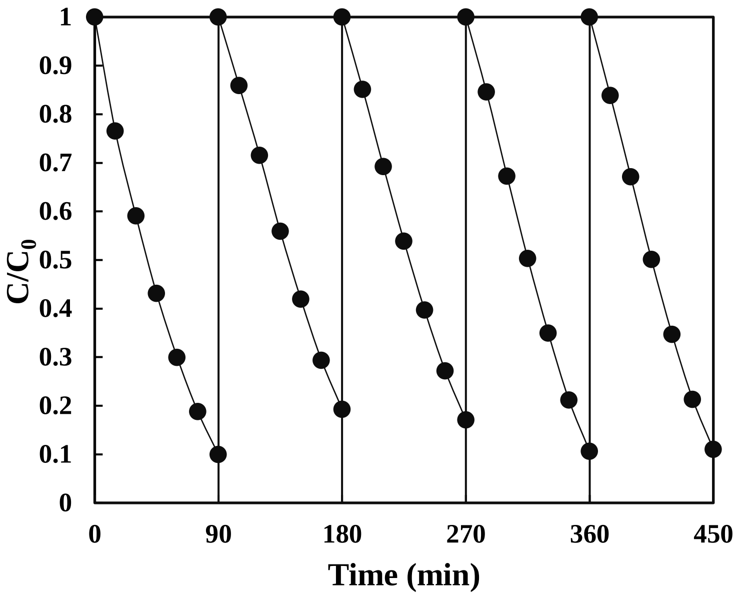

Figure 4-21. Photodegradation performance of 20 wt% CeO$_2$/Bi$_2$MoO$_6$ composite versus irradiation time under a 5-round cycling test (catalysts dosage: 1 g/L; temperature: 20 °C; pH 4.6 and initial RhB concentration: 8 ppm)

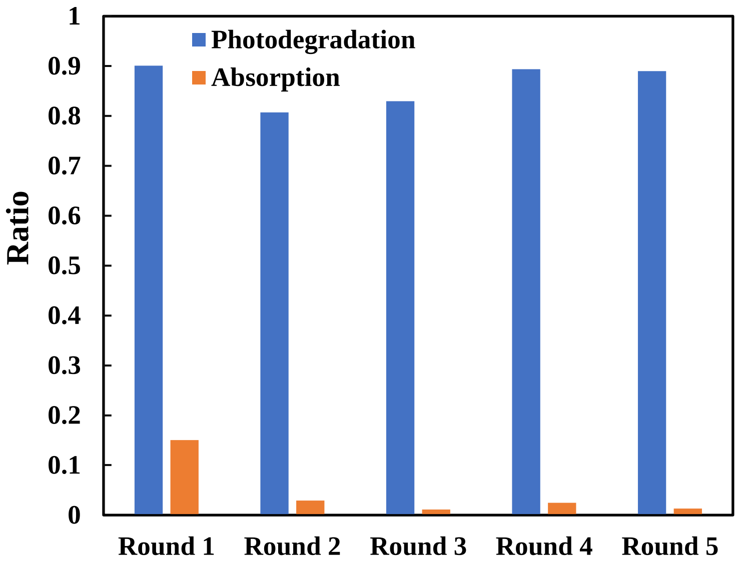

Figure 4-22. Adsorption ability and photodegradation ratio of 20 wt% CeO$_2$/Bi$_2$MoO$_6$ composite after 90-minute-irradiation under a 5-round cycling test (catalysts dosage: 1 g/L; temperature: 20 °C; pH 4.6 and initial RhB concentration: 8 ppm)

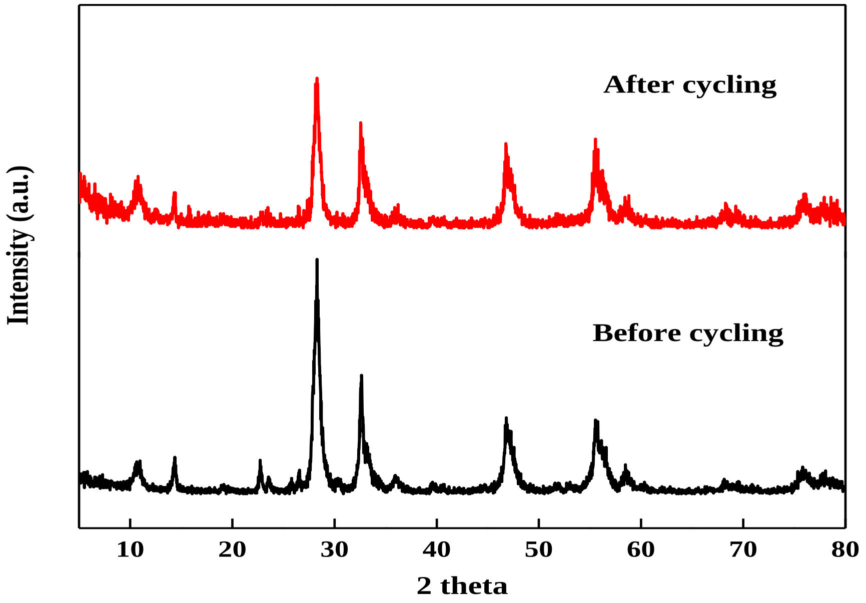

Figure 4-23. XRD spectra of 20 wt% CeO_2/Bi_2MoO_6 composite before and after cycling test

4.3.7 Roles of Active Species

One of the most important reasons that photocatalysis can be applied in wastewater treatment is due to the formation of strongly active oxidizing species, including hydroxyl radicals (•OH), superoxide radicals ($•O_2$) and holes (h^+), which are generated under light irradiation. These species can mineralize organic pollutants on the surface of photocatalysts into CO_2 and innocuous inorganic ions[8, 66, 67]. To investigate the roles of different kinds of active species, three types of scavengers aimed at eliminating oxidizing species were employed. In these experiments, N_2 bubbling into the suspension was introduced to reduce dissolved oxygen thus prevent the formation of superoxide radicals ($O_2^{•-}$)[16]. EDTA was used as a quencher of holes (h^+) and isopropanol was added to suppress the appearance of hydroxyl radicals (•OH)[68, 69]. The results are shown in Figure 4-24. Photodegradation activity declined after introducing scavengers, indicating a negative influence from scavengers. After adding EDTA, the photocatalytic activity decreased from 90.07% to 7.10%, implying that holes (h^+) were the most effective species during the degradation process. According to the literature[70-72], there are three reaction pathways for positive holes (h^+): (1) reacting with H_2O (Equation 2-7); (2) reacting with OH^- to form hydroxyl radicals (•OH) (Equation 2-5) on the catalyst surface for further oxidation; and (3) reacting directly with pollutants (Equation 2-6). However, when isopropanol was introduced, there was only a 2% decrease in removal ratio. Combined with reaction pathways of positive holes (h^+), it can be concluded that only a small proportion of holes (h^+) reacted with H_2O and OH^- to produce hydroxyl radicals (•OH) for further oxidation, most of which reacted directly with pollutants to finish degradation. As for adding N_2 bubbling, the photodegradation performance also showed a relatively significant decrease of 50% when compared to the value without scavengers, indicating that superoxide radicals ($O_2^{\bullet-}$) also played an important role in the degradation of RhB. Oxygen, acting as a scavenger, could be reduced by electrons (e^-) to superoxide radicals ($O_2^{\bullet-}$) (Equation 2-8) which either oxidize pollutants or react with hydroxyl radicals (•OH) to form HOO• radicals (Equation 2-9) for further degradation[72, 73]. For better comprehension, the kinetic analysis of different scavengers was plotted in Figure 4-25 and listed in Table 4-8. The degradation data fitted with pseudo first-order kinetics and the reaction rates were all in accordance with the degradation activity.

In summary, positive holes (h^+) and superoxide radicals ($O_2^{\bullet-}$) were the main active oxidizing species during the degradation process of RhB, while hydroxyl radicals (•OH) almost had no effect in the degradation.

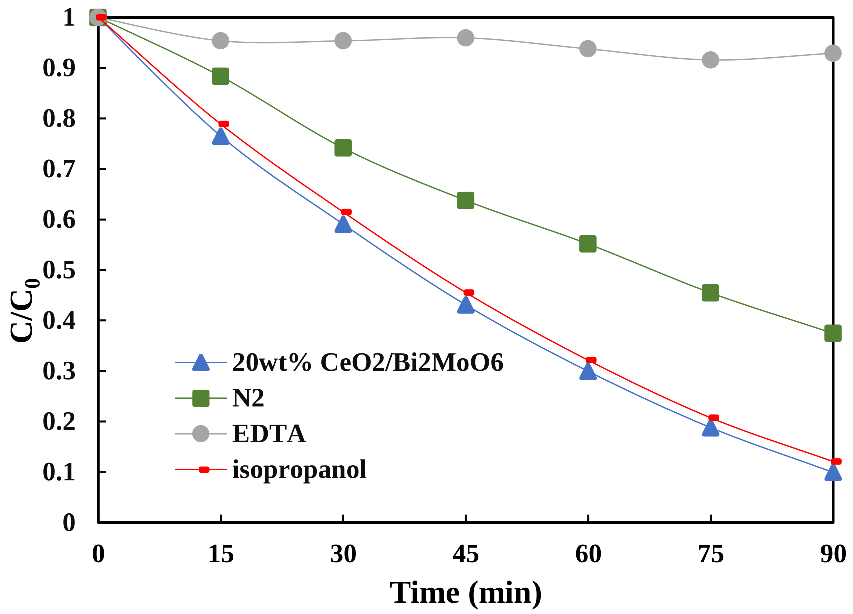

Figure 4-24. Influence of scavengers in the photodegradation of RhB (catalysts dosage: 1 g/L; temperature: 20 °C; pH 4.6 and initial RhB concentration: 8 ppm)

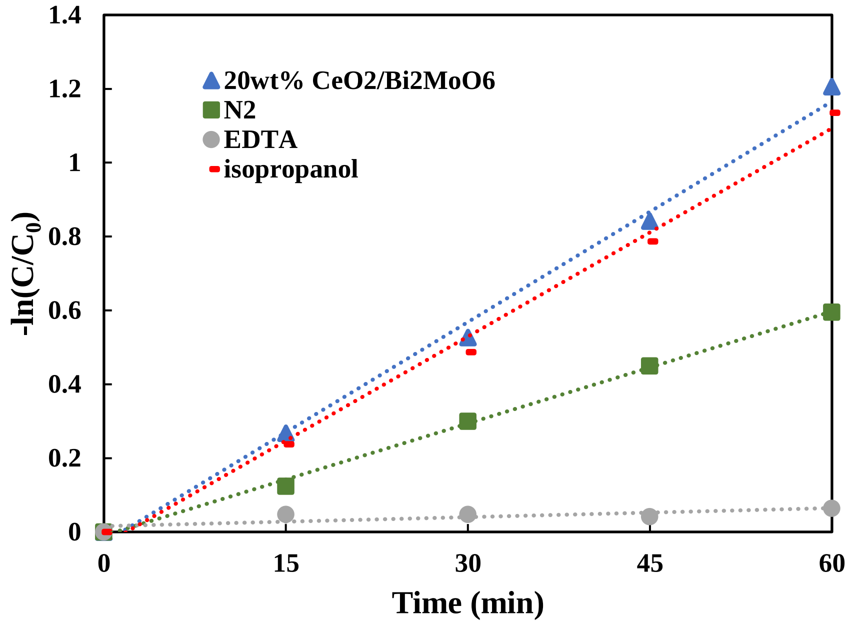

Figure 4-25. Photocatalytic kinetics for different scavengers (catalysts dosage: 1 g/L; temperature: 20 °C; pH 4.6 and initial RhB concentration: 8 ppm)

Table 4-8. Photodegradation ratio, reaction rate constant k and R^2 for different scavengers

Scavenger	Species removed	Degradation ratio	k (min^{-1})
-	-	90.07%	0.0199
isopropanol	Hydroxyl radicals (•OH)	87.93%	0.0188
N_2	Superoxide radicals ($O_2^{\bullet -}$)	40.47%	0.0101
EDTA	Holes (h^+)	7.10%	0.0008

4.3.8 Proposed Mechanism

When referring to a photocatalytic mechanism, a better understanding of the band positions of the semiconductor photocatalyst is necessary. Unlike metals with continuous electronic states, semiconductor molecules contain a vacant region, the band gap (E_g), between the VB that is fully occupied by electrons and an empty CB [73-75]. The valence and conduction band positions of CeO_2 and Bi_2MoO_6 can be calculated by Mulliken electronegativity theory given by Equations 2-2 and 2-3[20, 24, 76]. The calculated values of the photocatalysts are listed in Table 4-9. The positions of valence bands for CeO_2 and Bi_2MoO_6 were 2.52 eV and 2.91 eV respectively, indicating that photoinduced holes held a much higher redox potential than those of general oxidative species, such as $\bullet OH/OH^-$ (+1.99 eV)[48]. According to this experimental data, a possible photocatalytic mechanism diagram was generated (Figure 4-26). With sufficient light irradiation, electrons would be excited, jumping from the VB to the CB. As a result, there would be corresponding number of positive holes left in the VB due to charge balance. These photogenerated charges would either react with accepters and pollutants to finish oxidation or recombine with each other to produce heat[73]. The former one is the expected process. Because of different redox potentials of these two semiconductors, electrons prefer moving from CeO_2 to Bi_2MoO_6, while holes prefer flowing from Bi_2MoO_6 to CeO_2. Hence, electrons and holes will accumulate on the CB of Bi_2MoO_6 and VB of CeO_2, respectively. In other words, the formation of this Type II of heterojunction effectively separates electrons and holes to two semiconductors, thus decreasing their possibility of recombination and indirectly enhancing the photodegradation activity. Instead of reacting with H_2O and OH^- to form hydroxyl radicals (•OH), holes with much higher redox potential would directly attack RhB molecules. Electrons would react with oxygen dissolved in the suspension to generate superoxide radicals ($O_2^{\bullet -}$), finishing the oxidative reactions. In summary, the significant enhancement of photocatalytic activity of the composite is attributed to the formation of Type II heterojunction, which could effectively reduce the recombination of electrons and holes, thus increasing their separation efficiency. As a result, the photocatalytic performance would be enhanced.

Table 4-9. Band structures of semiconductor photocatalysts

Semiconductor	χ_p **(eV)**	E^e **(eV)**	E_g **(eV)**	E_{CB} **(eV)**	E_{VB} **(eV)**
CeO_2	5.56	4.50	2.92	-0.40	2.52
Bi_2MoO_6	6.13	4.50	2.55	0.36	2.91

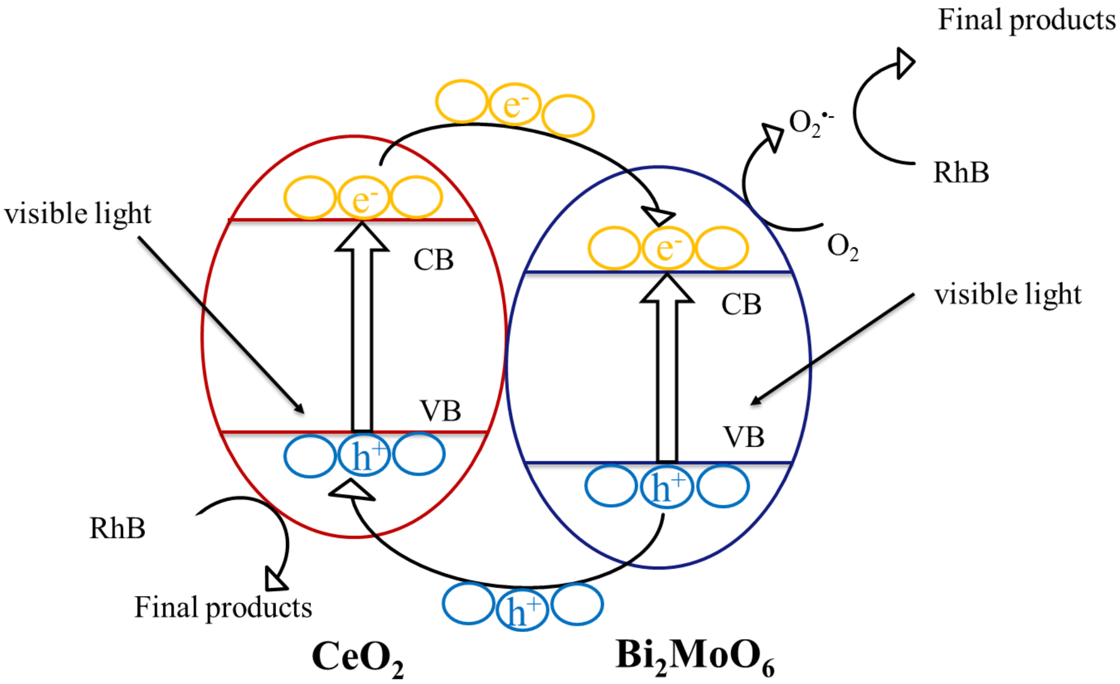

Figure 4-26. Diagram of possible photodegradation mechanism

4.4 Conclusions

In this project, CeO_2/Bi_2MoO_6 composites with different CeO_2 loading content were successfully prepared by the wet impregnation method. The heterojunctions formed between these two semiconductors effectively suppressed the recombination of photogenerated electrons and holes, thereby improving the photocatalytic activity of RhB degradation under visible light irradiation. The DRS results illustrated that after composition, the absorbance of visible light was increased. The composite with the best photocatalytic performance in a 90-minute degradation experiment was 20wt% CeO_2/Bi_2MoO_6, whose reaction rate was twice and 33 times higher than those of pure CeO_2 and pure Bi_2MoO_6, respectively. Both superoxide radicals ($O_2^{\bullet-}$) and holes (h^+) played important roles in the oxidation process, while the latter one took on greater significance. The cycling test indicated that the composite possessed good chemical and light stability. This study supplied more evidence that the formation of heterojunctions can be a successful way to overcome some of the challenges associated with photocatalysts, such as low separation efficiency of photoinduced charge carriers and low visible-light response. Moreover, this project also revealed the huge potential of CeO_2 using as a co-photocatalyst in wastewater treatment.

4.5 References

1. DeJohn, P.B. and R.A. Hutchins, Treatment of Dye Wastes with Granular Activated Carbon. Textile Chemist & Colorist, 1976. **8**(4).
2. Slokar, Y.M. and A.M. Le Marechal, Methods of decoloration of textile wastewaters. Dyes and Pigments, 1998. **37**(4): p. 335-356.
3. Patil, S.S. and V.M. Shinde, Biodegradation studies of aniline and nitrobenzene in aniline plant waste water by gas chromatography. Environmental Science & Technology, 1988. **22**(10): p. 1160-1165.
4. Padmanabhan, P., et al., Nano-crystalline titanium dioxide formed by reactive plasma synthesis. Vacuum, 2006. **80**(11): p. 1252-1255.
5. Malik, P.K., Dye removal from wastewater using activated carbon developed from sawdust: adsorption equilibrium and kinetics. Journal of Hazardous Materials, 2004. **113**(1): p. 81-88.
6. Khouni, I., et al., Decolourization of the reconstituted textile effluent by different process treatments: Enzymatic catalysis, coagulation/flocculation and nanofiltration processes. Desalination, 2011. **268**(1): p. 27-37.
7. Pagga, U. and D. Brown, The degradation of dyestuffs: Part II Behaviour of dyestuffs in aerobic biodegradation tests. Chemosphere, 1986. **15**(4): p. 479-491.
8. Gaya, U.I. and A.H. Abdullah, Heterogeneous photocatalytic degradation of organic contaminants over titanium dioxide: a review of fundamentals, progress and problems. Journal of Photochemistry and Photobiology C: Photochemistry Reviews, 2008. **9**(1): p. 1-12.

9. Andreozzi, R., et al., Advanced oxidation processes (AOP) for water purification and recovery. Catalysis Today, 1999. **53**(1): p. 51-59.

10. Bora, L.V. and R.K. Mewada, Visible/solar light active photocatalysts for organic effluent treatment: Fundamentals, mechanisms and parametric review. Renewable and Sustainable Energy Reviews, 2017. **76**: p. 1393-1421.

11. Bai, X., et al., Photocatalytic degradation of deoxynivalenol using graphene/ZnO hybrids in aqueous suspension. Applied Catalysis B: Environmental, 2017. **204**: p. 11-20.

12. Meng, X., Z. Zhang, and X. Li, Synergetic photoelectrocatalytic reactors for environmental remediation: a review. Journal of Photochemistry and Photobiology C: Photochemistry Reviews, 2015. **24**: p. 83-101.

13. Chong, M.N., et al., Recent developments in photocatalytic water treatment technology: a review. Water Research, 2010. **44**(10): p. 2997-3027.

14. Liu, Y., et al., A novel $CeO_2/Bi_4Ti_3O_{12}$ composite heterojunction structure with an enhanced photocatalytic activity for bisphenol A. Journal of Alloys and Compounds, 2016. **688**: p. 487-496.

15. Miao, H., et al., Origin of enhanced photocatalytic activity of F-doped CeO_2 nanocubes. Applied Surface Science, 2016. **370**: p. 427-432.

16. Wen, X.-J., et al., AgI nanoparticles-decorated CeO_2 microsheets photocatalyst for the degradation of organic dye and tetracycline under visible-light irradiation. Journal of Colloid and Interface Science, 2017. **497**: p. 368-377.

17. Wandre, T., et al., Sol–gel synthesized TiO_2–CeO_2 nanocomposite: an efficient photocatalyst for degradation of methyl orange under sunlight. Journal of Materials Science: Materials in Electronics, 2016. **27**(1): p. 825-833.

18. Choi, J., et al., Self-assembly of CeO_2 nanostructures/reduced graphene oxide composite aerogels for efficient photocatalytic degradation of organic pollutants in water. Journal of Alloys and Compounds, 2016. **688**: p. 527-536.

19. Contreras-García, M., et al., Synergic effect of the TiO_2-CeO_2 nanoconjugate system on the band-gap for visible light photocatalysis. Materials Science and Engineering: B, 2014. **183**: p. 78-85.

20. Wetchakun, N., et al., $BiVO_4/CeO_2$ nanocomposites with high visible-light-induced photocatalytic activity. ACS Applied Materials & Interfaces, 2012. **4**(7): p. 3718-3723.

21. Tian, J., et al., Enhanced photocatalytic performances of CeO_2/TiO_2 nanobelt heterostructures. Small, 2013. **9**(22): p. 3864-3872.

22. Song, H., et al., Fabrication of CeO_2 nanoparticles decorated three-dimensional flower-like BiOI composites to build pn heterojunction with highly enhanced visible-light photocatalytic performance. Journal of Colloid and Interface Science, 2018. **512**: p. 325-334.

23. Hsieh, S.-H., et al., Synthesis of mesoporous Bi_2O_3/CeO_2 microsphere for photocatalytic degradation of Orange II dye. Materials Research Bulletin, 2013. **48**(10): p. 4174-4180.

24. Meng, X. and Z. Zhang, Bismuth-based photocatalytic semiconductors: introduction, challenges and possible approaches. Journal of Molecular Catalysis A: Chemical, 2016. **423**: p. 533-549.

25. Li, H., et al., Synthesis and characterization of g-C_3N_4/Bi_2MoO_6 heterojunctions with enhanced visible light photocatalytic activity. Applied Catalysis B: Environmental, 2014. **160**: p. 89-97.

26. Meng, X. and Z. Zhang, Pd-doped Bi_2MoO_6 plasmonic photocatalysts with enhanced visible light photocatalytic performance. Applied Surface Science, 2017. **392**: p. 169-180.

27. Li, Z., X. Meng, and Z. Zhang, Few-layer MoS_2 nanosheets-deposited on Bi_2MoO_6 microspheres: A Z-scheme visible-light photocatalyst with enhanced activity. Catalysis Today, 2018.

28. Xu, Y.-S. and W.-D. Zhang, Anion exchange strategy for construction of sesame-biscuit-like $Bi_2O_2CO_3/Bi_2MoO_6$ nanocomposites with enhanced photocatalytic activity. Applied Catalysis B: Environmental, 2013. **140**: p. 306-316.

29. Wang, P., et al., A one-pot method for the preparation of graphene–Bi_2MoO_6 hybrid photocatalysts that are responsive to visible-light and have excellent photocatalytic activity in the degradation of organic pollutants. Carbon, 2012. **50**(14): p. 5256-5264.

30. Feng, Y., et al., Hydrothermal synthesis of CdS/Bi_2MoO_6 heterojunction photocatalysts with excellent visible-light-driven photocatalytic performance. Applied Surface Science, 2015. **353**: p. 87-94.

31. Meng, X. and Z. Zhang, Acetic Acid Assisted to Prepare Bi_2MoO_6 with Visible-Light-Induced Activity. General Chemistry, 2017. **3**(3).

32. Xie, H., et al., Microwave hydrothermal synthesis and visible-light photocatalytic activity of γ-Bi_2MoO_6 nanoplates. Materials Chemistry and Physics, 2008. **110**(2-3): p. 332-336.

33. Dai, W., et al., Hierarchical CeO_2/Bi_2MoO_6 heterostructured nanocomposites for photoreduction of CO_2 into hydrocarbons under visible light irradiation. Applied Surface Science, 2018. **434**: p. 481-491.

34. Meng, X. and Z. Zhang, Plasmonic ternary Ag–rGO–Bi_2MoO_6 composites with enhanced visible light-driven photocatalytic activity. Journal of Catalysis, 2016. **344**: p. 616-630.

35. Pfau, A. and K. Schierbaum, The electronic structure of stoichiometric and reduced CeO_2 surfaces: an XPS, UPS and HREELS study. Surface Science, 1994. **321**(1-2): p. 71-80.

36. Chen, L., et al., In situ synthesis of V^{4+} and Ce^{3+} self-doped $BiVO_4/CeO_2$ heterostructured nanocomposites with high surface areas and enhanced visible-light photocatalytic activity. The Journal of Physical Chemistry C, 2016. **120**(33): p. 18548-18559.

37. Wang, Y., et al., CO_2 photoreduction with H_2O vapor on highly dispersed CeO_2/TiO_2 catalysts: Surface species and their reactivity. Journal of Catalysis, 2016. **337**: p. 293-302.

38. Jiao, J., et al., Photocatalysts of 3D ordered macroporous TiO_2-supported CeO_2 nanolayers: design, preparation, and their catalytic performances for the reduction of CO_2 with H_2O under simulated solar irradiation. Industrial & Engineering Chemistry Research, 2014. **53**(44): p. 17345-17354.

39. Romeo, M., et al., XPS study of the reduction of cerium dioxide. Surface and Interface Analysis, 1993. **20**(6): p. 508-512.

40. Campbell, C.T. and C.H. Peden, Oxygen vacancies and catalysis on ceria surfaces. Science, 2005. **309**(5735): p. 713-714.

41. Guo, X., J. Li, and R. Zhou, Catalytic performance of manganese doped $CuO–CeO_2$ catalysts for selective oxidation of CO in hydrogen-rich gas. Fuel, 2016. **163**: p. 56-64.

42. Fan, J., et al., Thermal ageing of Pt on low-surface-area $CeO_2–ZrO_2–La_2O_3$ mixed oxides: effect on the OSC performance. Applied Catalysis B: Environmental, 2008. **81**(1-2): p. 38-48.

43. Choudhury, B., P. Chetri, and A. Choudhury, Oxygen defects and formation of Ce^{3+} affecting the photocatalytic performance of CeO_2 nanoparticles. RSC Advances, 2014. **4**(9): p. 4663-4671.

44. Torres, J., et al., Low-temperature oxidation of nitrided iron surfaces. The Journal of Physical Chemistry B, 2003. **107**(23): p. 5558-5567.

45. Szczepankiewicz, S.H., J.A. Moss, and M.R. Hoffmann, Slow surface charge trapping kinetics on irradiated TiO_2. The Journal of Physical Chemistry B, 2002. **106**(11): p. 2922-2927.

46. Li, K., et al., In-situ-reduced synthesis of Ti^{3+} self-doped TiO_2/g-C_3N_4 heterojunctions with high photocatalytic performance under LED light irradiation. ACS applied materials & interfaces, 2015. **7**(17): p. 9023-9030.

47. Zhang, L., et al., Fabrication of flower-like Bi_2WO_6 superstructures as high performance visible-light driven photocatalysts. Journal of Materials Chemistry, 2007. **17**(24): p. 2526-2532.

48. Meng, X. and Z. Zhang, Facile synthesis of BiOBr/Bi_2WO_6 heterojunction semiconductors with high visible-light-driven photocatalytic activity. Journal of Photochemistry and Photobiology A: Chemistry, 2015. **310**: p. 33-44.

49. Meng, X., et al., MoS_2 quantum dots-interspersed Bi_2WO_6 heterostructures for visible light-induced detoxification and disinfection. Applied Catalysis B: Environmental, 2017. **210**: p. 160-172.

50. Herrmann, J.-M., Heterogeneous photocatalysis: fundamentals and applications to the removal of various types of aqueous pollutants. Catalysis Today, 1999. **53**(1): p. 115-129.

51. Meng, X. and Z. Zhang, Synthesis, analysis, and testing of BiOBr-Bi_2WO_6 photocatalytic heterojunction semiconductors. International Journal of Photoenergy, 2015. **2015**.

52. Magdalane, C.M., et al., Photocatalytic degradation effect of malachite green and catalytic hydrogenation by UV–illuminated CeO_2/CdO multilayered nanoplatelet arrays:

investigation of antifungal and antimicrobial activities. Journal of Photochemistry and Photobiology B: Biology, 2017. **169**: p. 110-123.

53. Magdalane, C.M., et al., Evaluation on the heterostructured CeO_2/Y_2O_3 binary metal oxide nanocomposites for UV/Vis light induced photocatalytic degradation of Rhodamine-B dye for textile engineering application. Journal of Alloys and Compounds, 2017. **727**: p. 1324-1337.

54. Saravanakumar, K., et al., Fabrication of highly efficient visible light driven Ag/CeO_2 photocatalyst for degradation of organic pollutants. Journal of Alloys and Compounds, 2016. **664**: p. 149-160.

55. Daneshvar, N., D. Salari, and A. Khataee, Photocatalytic degradation of azo dye acid red 14 in water on ZnO as an alternative catalyst to TiO_2. Journal of Photochemistry and Photobiology A: Chemistry, 2004. **162**(2-3): p. 317-322.

56. Wong, C. and W. Chu, The direct photolysis and photocatalytic degradation of alachlor at different TiO_2 and UV sources. Chemosphere, 2003. **50**(8): p. 981-987.

57. Chiou, C.-H., C.-Y. Wu, and R.-S. Juang, Influence of operating parameters on photocatalytic degradation of phenol in UV/TiO_2 process. Chemical Engineering Journal, 2008. **139**(2): p. 322-329.

58. Wang, H., et al., Surface decoration of Bi_2WO_6 superstructures with Bi_2O_3 nanoparticles: an efficient method to improve visible-light-driven photocatalytic activity. CrystEngComm, 2013. **15**(44): p. 9011-9019.

59. Li, Y., et al., Kinetic study and model of the photocatalytic degradation of rhodamine B (RhB) by a TiO_2-coated activated carbon catalyst: Effects of initial RhB content, light

intensity and TiO_2 content in the catalyst. Chemical Engineering Journal, 2008. **142**(2): p. 147-155.

60. Martinez-de La Cruz, A. and U.G. Perez, Photocatalytic properties of $BiVO_4$ prepared by the co-precipitation method: Degradation of rhodamine B and possible reaction mechanisms under visible irradiation. Materials Research Bulletin, 2010. **45**(2): p. 135-141.

61. Chang, X., et al., Photodegradation of Rhodamine B over unexcited semiconductor compounds of BiOCl and BiOBr. Journal of Colloid and Interface Science, 2012. **377**(1): p. 291-298.

62. Shang, M., et al., Bi_2WO_6 with significantly enhanced photocatalytic activities by nitrogen doping. Materials Chemistry and Physics, 2010. **120**(1): p. 155-159.

63. Watanabe, T., T. Takizawa, and K. Honda, Photocatalysis through excitation of adsorbates. 1. Highly efficient N-deethylation of rhodamine B adsorbed to cadmium sulfide. The Journal of Physical Chemistry, 1977. **81**(19): p. 1845-1851.

64. Wu, T., et al., Photoassisted degradation of dye pollutants. V. Self-photosensitized oxidative transformation of rhodamine B under visible light irradiation in aqueous TiO_2 dispersions. The Journal of Physical Chemistry B, 1998. **102**(30): p. 5845-5851.

65. Dong, H., et al., A novel high-efficiency visible-light sensitive Ag_2CO_3 photocatalyst with universal photodegradation performances: simple synthesis, reaction mechanism and first-principles study. Applied Catalysis B: Environmental, 2013. **134**: p. 46-54.

66. Lu, M. and P. Pichat, Photocatalysis and water purification: from fundamentals to recent applications. 2013: John Wiley & Sons.

67. Kwon, S., et al., Photocatalytic applications of micro-and nano-TiO_2 in environmental engineering. Critical Reviews in Environmental Science and Technology, 2008. **38**(3): p. 197-226.

68. Ai, L., C. Zhang, and J. Jiang, Hierarchical porous AgCl@ Ag hollow architectures: self-templating synthesis and highly enhanced visible light photocatalytic activity. Applied Catalysis B: Environmental, 2013. **142**: p. 744-751.

69. Wen, X.-J., et al., Facile synthesis of a visible light α-Fe_2O_3/BiOBr composite with high photocatalytic performance. RSC Advances, 2016. **6**(5): p. 4035-4042.

70. Houas, A., et al., Photocatalytic degradation pathway of methylene blue in water. Applied Catalysis B: Environmental, 2001. **31**(2): p. 145-157.

71. Turchi, C.S. and D.F. Ollis, Photocatalytic degradation of organic water contaminants: mechanisms involving hydroxyl radical attack. Journal of Catalysis, 1990. **122**(1): p. 178-192.

72. Dong, S., et al., Recent developments in heterogeneous photocatalytic water treatment using visible light-responsive photocatalysts: a review. RSC Advances, 2015. **5**(19): p. 14610-14630.

73. Kabra, K., R. Chaudhary, and R.L. Sawhney, Treatment of hazardous organic and inorganic compounds through aqueous-phase photocatalysis: a review. Industrial & Engineering Chemistry Research, 2004. **43**(24): p. 7683-7696.

74. Lee, S.-Y. and S.-J. Park, TiO_2 photocatalyst for water treatment applications. Journal of Industrial and Engineering Chemistry, 2013. **19**(6): p. 1761-1769.

75. Linsebigler, A.L., G. Lu, and J.T. Yates Jr, Photocatalysis on TiO_2 surfaces: principles, mechanisms, and selected results. Chemical reviews, 1995. **95**(3): p. 735-758.

76. Xu, Y. and M.A. Schoonen, The absolute energy positions of conduction and valence bands of selected semiconducting minerals. American Mineralogist, 2000. **85**(3-4): p. 543-556.

Chapter 5 – Conclusions and Future work

5.1 Conclusions of Projects

Firstly, Bi_2MoO_6 was synthesized by the solvothermal method with the assistance of ethylene glycol and ethanol. The preparation conditions, including reaction temperature, reaction time, and precursor stirring time were optimized according to the photocatalytic performance of Rhodamine B (RhB) degradation under visible light irradiation. The samples were also characterized by XRD and SEM. The results indicated that Bi_2MoO_6 fabricated at 180°C for 20 h with a stirring time 10 min exhibited the higher photodegradation activity, which may be attributed to the higher crystallinity and more stereoscopic plate-like morphology of the photocatalyst particles. Moreover, a comparison between Bi_2MoO_6 prepared by the solvothermal and hydrothermal synthesis methods was performed by comparing the performances of the photocatalysts during the decomposition of RhB under visible light illumination.

Secondly, the CeO_2/Bi_2MoO_6 semiconductor heterojunctions with different CeO_2 loading contents were successfully fabricated by the wet impregnation method. The photocatalytic activities of as-prepared samples were investigated by degrading RhB under visible light irradiation. The 20 wt% CeO_2/Bi_2MoO_6 composite showed the highest photocatalytic activity, which was 24% and 83% higher than those of pure Bi_2MoO_6 and pure CeO_2, respectively. The kinetic study indicated that the photodegradation process fitted well with a pseudo-first-order model. Moreover, the effect of some operating parameters including temperature, pH, catalyst dosage and initial RhB concentration was investigated. A cycling test was performed to test the reusability of the composite. The results revealed that even after a 5-cycle degradation, the photocatalytic performance and crystallinity were maintained at high levels. All these results revealed that the CeO_2/Bi_2MoO_6 composite could be applied in long-term experiments.

The possible mechanism of the improvement in photodegradation activity when compared to the pure photocatalysts and the weighted mechanical mixture of the photocatalysts was proposed according to quenching experimental results. Photo-induced holes (h^+) were the main active species and superoxide radicals ($O_2^{\bullet -}$) also played a role in the degradation process. The formation of heterojunctions on the interface of two semiconductors forced holes to move to the VB of CeO_2 while electrons preferred to stay on the CB of Bi_2MoO_6. This kind of migration effectively improved the separation efficiency of photo-induced charge carriers and reduced their recombination. As a result, the photocatalytic activity was enhanced.

In summary, Bi_2MoO_6 synthesized by the solvothermal method showed the highest photodegradation performance under visible light irradiation when the reaction temperature, time and precursor stirring time were maintained at 180°C, 20 h and 10 min respectively. The as-prepared CeO_2/Bi_2MoO_6 composites showed a significant improvement in RhB photodegradation and good reusability, which makes it possible for them to be applied in industry in the future.

5.2 Future Work Recommendations

The optimization of Bi_2MoO_6 synthesis in the composites need to be performed to reduce the generation of intermediates and obtain a better crystal structure.

The degradation of other pollutants, including some colorless contaminants, needs to be investigated because in large-scale and industrial applications, the wastewater contains various kinds of pollutants.

Appendix

A-1. Calculation of Photodegradation Ratio from Absorbance

Figure A-1 shows the relationship between RhB concentration (ppm) and its absorbance (A) at 554 nm, which fits well with a first-order polynomial ($R^2 = 0.9998$). As a result, the photocatalytic ratio can be represented by Equation A-1:

$$RhB\ remaining\ (\%) = \frac{C}{C_0} \times 100\% = \frac{(\frac{A}{0.2116})}{(\frac{A_0}{0.2116})} \times 100\% = \frac{A}{A_0} \times 100\% \qquad \text{(Eq. A-1)}$$

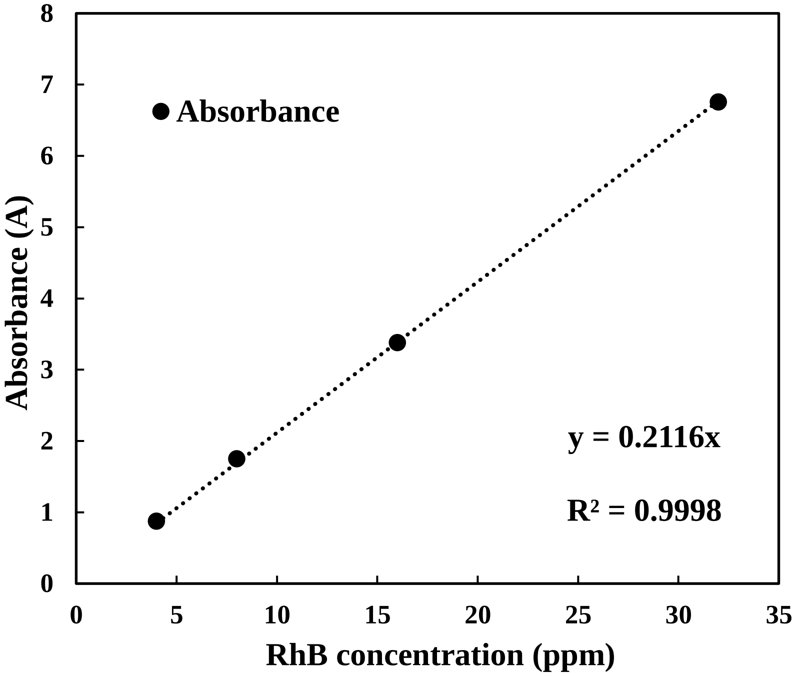

Figure A-1. The relation between RhB concentration and its absorbance at 554 nm